Assessment of Arctic sea ice properties during advanced melt using C- and L-band polarimetric synthetic aperture radar

by

Aikaterini Tavri

B.Sc., University of the Aegean 2014

M.Sc., Technical University of Munich, 2016

A Dissertation Submitted in Partial Fulfillment of the
Requirements for the Degree of

DOCTOR OF PHILOSOPHY

in the Department of Geography

University of Victoria

We acknowledge and respect the lək̓ʷəŋən peoples on whose traditional territory the university stands and the Songhees, Esquimalt and W̱SÁNEĆ peoples whose historical relationships with the land continue to this day.

Supervisory Committee

Assessment of Arctic sea ice properties during advanced melt using C- and L-band polarimetric synthetic aperture radar

by

Aikaterini Tavri

B.Sc., University of the Aegean 2014

M.Sc., Technical University of Munich, 2016

Supervisory Committee

Dr. Randall Scharien, Supervisor
Department of Geography

Dr. Maycira Costa, Departmental Member
Department of Geography

Dr. Torsten Geldsetzer, Outside Member
Department of Geography, University of Calgary

Abstract

Over recent decades, there have been significant changes in Arctic sea ice, marked by a shift from thicker to thinner ice, and reductions in extent and volume. These changes, along with extended melt seasons, have accelerated sea ice melt and the ice-albedo feedback. This dissertation leverages Synthetic Aperture Radar (SAR) to analyze sea ice dynamics and thermodynamics at various scales.

Focusing on the advanced melt season, this dissertation examines the relationships between sea ice geophysical properties and SAR backscatter signatures at C- and L-bands. Our analysis uses RADARSAT-2 (C-band) and ALOS-2/PALSAR-2 (L-band) imagery in different polarimetric modes to assess sea ice type separability and the effects of incidence angle and melt ponds on backscatter. We discover that C-band SAR is more effective early in the melt season, while L-band SAR provides clearer delineation of ice features later in the season. Additionally, the co-pol ratio (VV/HH) was found to be a consistent indicator of the melt ponds for FYI, despite environmental changes, such as wind-roughened melt ponds, for both frequencies and incidence angles in the near and far range.

Utilizing our findings, we developed a dual frequency, dual-incidence angle sea ice classification approach using a random forest classifier. We achieved over 70% accuracy in sea ice type classification, validated by airborne measurements. This research underscores the value of a dual-frequency approach in improving sea ice classification, particularly for first-year and multi-year ice during advanced melt stages, while considering the evolution of deformed ice types in the advanced melt season. The findings contribute significantly to climate studies and operational services and are pertinent to future dual-frequency SAR missions.

Keywords: sea ice, SAR, C-band, L-band, advanced melt, compact polarimetry, full polarimetry, RADARSAT Constellation Mission, separability, melt season, classification, deformed ice, landfast ice

“Εοικα γούν τούτου γε σμικρώ τινι αυτώ τούτω σοφώτερος είναι, ότι α μη οίδα ουδέ οίομαι ειδέναι.”

Σωκράτης - Socrates (469-399 BC)

Dedication

This dissertation is dedicated to *Rad*, whose encouragement and advice have been constant throughout this challenging journey. Your willingness to stand by my side, offering insight and care, has been instrumental in the fruition of this work. Your presence and cheering have been my rock, and I am deeply grateful for your resolute belief in me.

Acknowledgements

What an incredible journey this Ph.D. has been! Completing this academic endeavour would not have been possible without the support of my invaluable network of mentors, colleagues, and loved ones.

I extend my sincerest gratitude to my supervisor, Randall Scharien, whose steadfast guidance, support, and invaluable insights have been the cornerstones of this research journey. Our extensive discussions, creative collaborations, and even weekend work sessions have been the driving force behind my scientific growth. I sincerely appreciate the trust and confidence he placed in me, providing numerous opportunities to excel in academia and research. His expertise and mentorship have been instrumental in shaping the direction and quality of this thesis. In addition, I would like to express my sincere gratitude for providing me with the extraordinary opportunity to participate in the Multidisciplinary Drifting Observatory for the Study of Arctic Climate (MOSAiC) expedition. This experience was not only invaluable to my growth as a researcher but also a unique learning journey, allowing me to witness the processes and dynamic nature of summer sea ice.

I also want to express my appreciation to my thesis committee members, Dr. Torsten Geldsetzer and Dr. Maycira Costa, for their constructive feedback and expert guidance. Their commitment to upholding the rigour of my research has been invaluable. Additionally, I am grateful to Dr. David Goodenough for his guidance during the initial years of my Ph.D.

I extend my special thanks to the remarkable individuals I had the privilege of meeting and working alongside during the MOSAiC expedition. My roommate, Maddie Smith, deserves a heartfelt acknowledgment for her camaraderie and support throughout our time on board. I would also like to express my appreciation to our dedicated group leader, Melinda Webster, whose guidance and expertise were instrumental during the expedition. Furthermore, I am grateful for the friendships I forged with fellow researchers Evgenii Salganik and Felix Linhardt, whose camaraderie and shared experiences made this once-in-a-lifetime journey all the more memorable. The collective efforts and collaborative spirit

of everyone involved in the MOSAiC expedition made it an unforgettable chapter in my academic and personal journey. Thank you all for your support and contributions.

The Department of Geography has been an incredible source of support over the years, thanks to the dedicated staff, faculty, and fellow students. Special acknowledgments go to Terri Evans, David Atkinson, and Janette Delong. I would also like to extend my gratitude to both current and former members of the ICE lab for fostering a conducive learning environment.

My heartfelt thanks go to my parents, Anna and Spiros, for their immense support, patience, and encouragement. Their unwavering belief in my abilities has been a constant wellspring of motivation. I am particularly grateful to my sister, Panagiota, for her unwavering support and empathetic ear along this journey.

To my friends and peers, I extend my deepest appreciation for providing a strong network and offering valuable insights and discussions that enriched my research and supported my mental well-being. I want to give special thanks to Tara and Monica for their encouraging discussions during our lunch breaks. I also thank Alex, Arash, Lily, and Eva for being a steady source of laughter and warmth, as well as my dear friends Vanessa, Maria, Carla, Kata and Ino.

I must also acknowledge the vital financial support provided by MEOPAR, SNAME, and the University of Victoria, which made this dissertation possible.

To all these individuals and entities, your collective support and encouragement have been indispensable in completing this dissertation. From the depths of my heart, thank you.

Table of Contents

Abstract iii
Dedication v
Acknowledgements vi
Table of Contents viii
List of Tables x
List of Figures xi
List of Acronyms xiv
List of Symbols xvi
Preface xvii

Chapter 1: Introduction 1
1.1. Motivation and Rationale 1
1.2. Objectives 3
1.3. Sea ice properties 4
1.3.1. Sea ice types 5
1.3.2. Sea ice formation and growth 6
1.3.3. Sea ice in the melt season 7
1.3.4. Deformed sea ice 10
1.4. Sea ice importance for global climate processes 12
1.5. Current state of sea ice 13
1.5.1. Sea ice in the Canadian Arctic Archipelago 14
1.6. Sea ice monitoring using Synthetic Aperture Radar 15
1.6.1. Sea ice dielectric properties and penetration depth 17
1.7. Dissertation outline 19

Chapter 2. Melt Season Arctic Sea Ice Type Separability Using Fully and Compact Polarimetric C- and L-band Synthetic Aperture Radar 21
Abstract 21
2.1. Introduction 22
2.2. Seasonal stages, Study site and Data 25
2.2.1. Seasonal stages 25
2.2.2. Study site 26
2.2.3. SAR and Optical datasets 28
2.2.4. Ancillary datasets 30
2.3. Methods 31
2.3.1. C- and L-band SAR image processing 31
2.3.2. SAR polarimetric parameter analysis 32
2.3.3. Melt Pond Fraction and SAR parameter comparison 33
2.3.4. Software usage 34
2.4. Results 34
2.4.1. Melt Season stage definition 34
2.4.2. FYI and MYI scattering properties across the melt season 37

2.4.3. Melt Pond Fraction retrievals 42
2.4.4. C- and L-band ice type separability for FP and CP parameters 46
2.4.5. FP and CP Parameter redundancy 50
2.5. Summary and Conclusions 52
2.6. Acknowledgments 55
2.7. Funding 55

Chapter 3. C- and L-band Synthetic Aperture Radar synergy for Arctic sea ice classification in the advanced melt season 56
Abstract 56
3.1. Introduction 57
3.2. Study area and data 60
3.2.1. Full polarimetric C- and L-band SAR 62
3.2.2. Auxiliary datasets 62
3.3. Methodology 65
3.3.1. SAR image processing and class selection 66
3.3.2. Image classification and validation 68
3.4. Results and Discussion 69
3.4.1. Airborne ice-type roughness and thickness in LW at M'Clintock Channel 70
3.4.2. C- and L- band SAR backscatter variability from LW to advance melt 72
3.4.3. *Ice type classification using C- and L- band SAR* 74
3.4.4. DFI validation with the airborne track 82
3.5. Conclusions 86
3.6. Acknowledgments 88
3.7. Funding 88

Chapter 4. Conclusions 90
4.1. Summary of key findings 91
4.2 Significance implications and recommendations 92
4.3 Research limitations 94

References 96

Appendix A 108

List of Tables

Table 2.1: SAR and optical image characteristics. 29

Table 2.2: Grouping of FP and CP polarimetric parameters, using Spearman's correlation coefficient ≥ 0.80 for FYI and MYI types (n = 6000). With * we denote the negative correlations 51

Table 3.1: Data description and characteristics. 64

Table 3.2: An overview of the investigated SAR polarimetric parameters in this study. 65

Table 3.3: Confusion matrices for C- and L-band SAR RF classification scenarios in LW, PO and PD 75

Table 3.4: Mean Square Error (MSE) between the estimated value from the trained model and the actual value from each class ROI. 81

Table S.1: An overview of the SAR polarimetric parameters examined in this study. 108

List of Figures

Figure 1.1: Arctic sea ice extent percentage difference during the winter maximum (March) and summer minimum (September) relative to the mean values for the 1979-2022 period. Based on a least-squares regression, the rate of loss for September is 12.3% per decade (Adapted from: 2022 Arctic report Card 2022, NOAA). 1

Figure 1.2: Schematic depicting the complex processes governing the Arctic snow and sea ice across the seasons. The close-ups focus on the snow–ice (left) and ice–ocean (right) interfaces. (Adapted from Nicolaus et al., 2020). 5

Figure 1.3: Optical high-resolution images (VIS-RGB) depicting smooth FYI and MYI regions in the Canadian Arctic Archipelago. Each advanced melt stage is shown portraying changes in ice type surface properties. 9

Figure 1.4: Optical high-resolution images (VIS-RGB) depicting a region of deformed ice in the Canadian Arctic Archipelago. Each advanced melt stage is shown, portraying changes in ice type surface properties.....11

Figure 1.5: Time series and trends of average July seasonal FYI, average September MYI and melt season duration anomalies in the Canadian Arctic Archipelago from 1979 to 2018. (Adapted from Howell and Brady 2019). 15

Figure 1.6: Comparison of passive optical satellite sensors with active SAR sensors of different frequencies for sea ice monitoring in the wintertime. Lower frequency SAR (L-band) is characterized by higher penetration depth compared to C-band SAR in dry snow conditions 18

Figure 1.7: Comparison of SAR sensor frequencies for sea ice monitoring in the summertime. Lower frequency SAR is characterized by higher penetration depth compared to C-band SAR however, the presence of melt ponds impedes signal penetration at both frequencies. 19

Figure 2.1: a) Study area map showing the southwestern Canadian Arctic Archipelago. Areal extents of C- and L-band SAR images and optical scenes are shown along with an airborne electromagnetic (AEM) sea ice thickness track. b) A late winter (LW) SAR image showing the ice thickness data and ROIs used for aggregating scattering data across all seasons. c) Histograms of ice thickness derived from the complete survey track (orange) and the segment that coincides with SAR acquisitions (blue).....27

Figure 2.2: Workflow for SAR polarimetric parameter retrieval and optical scene processing to melt pond fraction. The two processing chains were executed concurrently to facilitate comparison between backscatter parameters and melt pond fraction. .31

Figure 2.3: a) ASCAT data and ROIs used for FYI and MYI time series backscatter coefficient σ^0 extraction. b) Backscatter time series and seasonal regimes denoted by green dashed lines (MO, PO, PD). c) Time series ERA5 bias-corrected atmospheric reanalysis data of mean surface wind speed (at 10m) and mean surface air temperature (at 2m). Vertical, light blue lines represent the days of the RS2 and PS2 acquisitions. 35

Figure 2.4: Image subsets of optical RGB composites and C- and L-band HH backscatter variability during advanced melt season substages. The top panel shows the PO stage with: a) WV2-1; a_i) RS2-6; a_{ii}) RS2-5; and a_{iii}) PS2-2. The middle panel shows the PE stage with: b) WV3-1; b_i) RS2-7; b_{ii}) RS2-8 (there is no L-band

scene). The bottom panel shows the PD stage with: c) WV3-2; c_i) RS2-9; c_{ii}) RS2-10; and c_{iii}) PS2-3. 36

Figure 2.5: Mean total power (span) for C- and L-band ROIs in late winter (LW), melt onset (MO), pond onset (PO), pond evolution (PE), and pond drainage (PD). The analysis encompasses NR and FR for C-band during all stages, and L-band FR during PO and PD. Additional melt pond water and bare ice samples in the advanced melt (see text for description). L-band scenes are indicated by an "L" suffix. 38

Figure 2.6: Bar plots of relative scattering mechanisms from the m_χ decomposition, from C-band acquisitions in NR (left panel) and FR (right panel). Groups a) to e) correspond to late winter (LW), melt onset (MO), pond onset (PO), pond evolution (PE), and pond drainage (PD). Bare ice and melt ponds samples are shown in addition to FYI during stages PO to PD. 40

Figure 2.7: Bar plots of relative scattering mechanisms from the m_χ decomposition, from L-band acquisitions in FR during a) pond onset (PO) and b) pond drainage (PD). Bare ice and melt ponds samples are shown in addition to FYI during stages PO to PD. 42

Figure 2.8: a) MPF barplot time series of FYI and MYI, retrieved from optical imagery. The vertical lines indicate standard deviation. b) RGB colour composite image subsets demonstrating surface conditions in the corresponding dates during PO, c) and d) in PE, and e) in PD substages of the advanced melt. 43

Figure 2.9: a) Scatter plots of the co-polarized ratio (VV/HH) and b) the cross-polarized (HV/HH) ratio against MPF from PO and PD substages. Pearson's product moment correlation coefficient (r) is given as a measure of linear association between the polarimetric ratio and MPF along with the significance level. The shaded area represents the size of the confidence interval for the regression estimate and here is set to 95%. 44

Figure 2.10: FYI and MYI type separability heatmaps using Kolmogorov-Smirnov (KS) distance for samples based on RS2 scene a) C-band FP parameters. b) C-band CP parameters. Seasonal stages and NR and FR incidence angles are shown at the bottom. 47

Figure 2.11: Kolmogorov-Smirnov (KS) separability heatmaps for FYI and MYI at L-band. a) L-band FP parameters. b) CP parameters. Seasonal stages and FR incidence angles are shown at the bottom. 49

Figure 3.1: The study area in the McClintock channel, in the western Canadian Arctic Archipelago. a) Canadian Ice Service (CIS) chart presenting the sea ice types in the extended area with dashed-line and line rectangles denoting the areal extents of the ALOS-2 PALSAR-2 and RASARSAT-2 61

Figure 3.2: Methodological workflow for the SAR image classification using a Random Forest machine learning algorithm. ROIs representing zones of homogeneous sea ice types are used for training the classification model that classifies each SAR image. 67

Figure 3.3: a) Late Winter (LW) sea ice surface roughness and thickness histograms for the overlapping SAR image portion of the survey line, indicating mode and mean statistics. Ice types are separated into deformed ice (DFI) and non-DFI based on a roughness threshold. b) Scatterplots between sea ice roughness and thickness for each type, showing the relationship between the two parameters using Spearman's correlation coefficient (ρ). 71

Figure 3.4: Boxplots presenting the distributions of each ice type at both C- and L-band during LW and over the advanced melt season. Each box consists of 400 pixels for FYI and MYI, while the DFI samples are based on ice roughness track points (120pixels).....72

Figure 3.5: LW SAR HH subsets and classified images for C-band in NR and FR. Each classification output has image segmentation objects based on the LW SAR image overlaid for visual reference. 76

Figure 3.6: High-resolution optical scenes and classified images for C-band combining NR and FR scenes and C- and L-band for PO and PD stages for FYI, DFI and MYI. Each classification output has image segmentation objects based on the LW SAR image overlaid for visual reference. 78

Figure 3.7: Classification results for C- and L-band SAR in PD for NR and FR incidence angles. Each classification output has image segmentation objects based on the LW SAR image overlaid for visual reference 80

Figure 3.8: Transect plot for DFI class validation using in situ ice roughness data from the airborne survey track in LW. We compare only the results from the same incidence angle in FR for consistency between C- and L-band data.....82

Figure 3.9: Line plots of C- and L-band HH backscatter along the AEM track, a) in PO and b) in PD. The lines are smoother with a 8-measurement averaging window size to support data comparison. Stars symbols indicate the survey points identified as DFI. 84

Figure 3.10: Stacked bar plots of relative scattering mechanisms for each ice type using the Freeman-Durden decomposition from C- and L-band band acquisitions in NR (left panels) and FR (right panels), with the L-band scenes indicated. Groups correspond to a) LW, b) PO, and c) PD.....85

Figure S.1: Moderate Resolution Imaging Spectroradiometer (MODIS) corrected reflectance, true color timeseries of the advanced melt sub-stage evolution, for 2018 over M'Clintock Channel. The seasonal stages shown are Pond Onset (PO), Pond Evolution (PE) and Pond Drainage (PD).....109

Figure S.2: Spearman's correlation matrices for the MYI FP mode. The heatmaps represent the correlation matrices from pond onset (PO) and pond drainage (PD) substages for each polarimetric parameter at C- and L-band. The effect of incidence angle is examined for the near and far range (NR, FR). 110

Figure S.3: Spearman's correlation matrices for the MYI CP mode. The heatmaps represent the correlation matrices from pond onset (PO) and pond drainage (PD) substages for each polarimetric parameter at C- and L-band. The effect of incidence angle is examined for the near and far range (NR, FR). 111

List of Acronyms

AO	Arctic Oscillation
ALOS-2 / PALSAR-2	Advanced Land Observing Satellite-2 / Phased Array type L-band Synthetic Aperture Radar-2
ALS	Air-borne Laser Scanner
ASCAT	Advanced Scatterometer
CAA	Canadian Arctic Archipelago
CIS	Canadian Ice Service
CISDA	Canadian Ice Service Digital Archive
CP	Compact polarimetric
dB	Decibel
DFI	Deformed year ice
DL	Drained ice layer
DOY	Day of the Year
EM	Electromagnetic
ERA5	European Center for Medium-Range Weather Forecasts (ECMWF) atmospheric reanalysis
ESA	European Space Agency
FP	Fully polarimetric
FR	Far range
FYI	First year ice
GE1	GeoEye-1
GRD	Ground Range Detected
JAXA	Japan Aerospace Exploration Agency
KS	Kolmogorov-Smirnov
LW	Late Winter
MEOPAR	Marine Observation and Prediction Network
MIZ	Marginal ice zone
MO	Melt Onset

MODIS	Medium Resolution Imaging Spectrometer
MOSAiC	The Multidisciplinary drifting Observatory for the Study of Arctic Climate
MPF	Melt pond fraction
MPF	Melt pond Fraction
MSE	Mean square error
MYI	Multiyear ice
NAO	North Atlantic Oscillation
NISAR	NASA-ISRO SAR
NR	Near range
ON	Off-Nadir
PD	Pond Drainage
PE	Pond Evolution
PO	Pond Onset
PS2	ALOS-2/PALSAR-2
RCM	RADARSAT Constellation Mission
RADARSAT-2	C-band Radar Satellite-2
RF	Random Forest
ROI	Regions of interest
ROSE-L	Radar Observing System for Europe - L-Band
RS2	RADARSAT-2
S1	Sentinel-1
SAR	Synthetic Aperture Radar
SIR	Scatterometer Image Reconstruction
SL	Surface granular layer
SLC	Single Look Complex
VIS-NIR	Visible Near-Infrared
WV2	Worldview-2
WV3	Worldview-3

List of Symbols

σ^0	Microwave backscatter coefficient
$^{\circ}C$	Degrees Celsius
CO_2	Carbon Dioxide
SPAN	Total backscattered power
T_{air}	Air temperature
HV/HH	Cross-polarization ratio
VV/HH	Co-polarization ratio
s_{rms}	Root-mean-square height
τ_{rms}	Threshold for root-mean-square height
α	Significance level (for statistical tests)
α_s	Alpha scattering angle
μ	Conformity
HH, HV, VV, RR, RL, RV,RH	Linear and circular sigma naught backscatter intensities
S	Scattering Matrix
S_0, S_1, S_2, S_3	Stokes vectors
RR/RL	Circular polarization ratio
RV/RH	Right co-polarized ratio
m	Degree of polarization
$m\chi_{d,s,v}$	Mchi decomposition
r	Pearson's correlation coefficient
$^{\circ}$	Degrees

Preface

This dissertation is an original work by the author.

Chapter 2 has been published in the Canadian Journal of Remote Sensing:

Tavri, A., Scharien, R.K, and Geldsetzer, T., (2023). Melt Season Arctic Sea Ice Type Separability Using Fully and Compact Polarimetric C- and L-band Synthetic Aperture Radar. Canadian Journal of Remote Sensing, VOL. 49, NO. 1, 2271578. https://doi.org/10.1080/07038992.2023.2271578

Chapter 3 has been submitted for publication as of October 31st 2023 to the Journal Remote Sensing of Environment:

Tavri, A., Scharien, R.K., (2023). C- and L-band Synthetic Aperture Radar synergy for Arctic sea ice classification in the advanced melt season. *Remote Sensing of Environment*

Chapter 1: Introduction

1.1. Motivation and Rationale

The Earth's cryosphere, comprising elements like snow, sea ice, permafrost, and glaciers, is integral to climate regulation, influencing the absorption of electromagnetic radiation and poleward heat flux (Carsey et al., 1992; Meier et al., 2014). Unprecedented changes, especially in sea ice, influence the Arctic climate and mid-latitude climatic processes, thereby impacting the global climate system (Dorn et al., 2007; Döscher et al., 2014). Over the past two decades, the Arctic has witnessed a decline in sea ice extent and thickness, with climate models indicating a shift towards younger, thinner ice types (Stroeve et al., 2007; Meier et al., 2014; Boisvert et al., 2015; Sumata et al., 2023). Sea ice decline is particularly pronounced in the summer, with a shrinking rate of 12.3% per decade from 1979 to 2022 (Figure 1.1) (Meier et al., 2022).

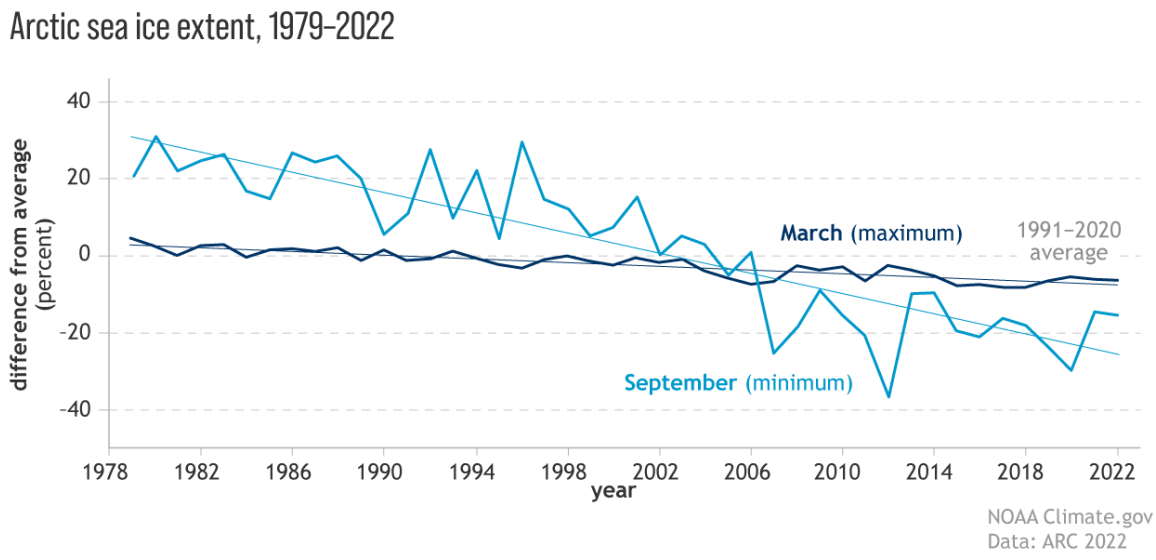

Figure 1.1: Arctic sea ice extent percentage difference during the winter maximum (March) and summer minimum (September) relative to the mean values for the 1979-2022 period. Based on a least-squares regression, the rate of loss for September is 12.3% per decade (Adapted from: 2022 Arctic report Card 2022, NOAA).

Earlier and longer summer melt seasons have multifaceted impacts on the Arctic environment. The accelerated melting of thinner first-year ice (FYI) intensifies the sea ice albedo feedback (Perovich, 2002). Melt ponds formed by the melting snow and ice reduce surface albedo by increasing solar energy absorption, further diminishing sea ice extent (Grenfell and Perovich, 2004). As Arctic sea ice transitions towards a regime dominated by FYI, which typically exhibits higher MPF than MYI, accurate identification and mapping of ice types during the melt season becomes essential. This is crucial for studying the energy interchange between the atmosphere and the ocean and predicting the annual sea ice cycle. Current climate models need significant improvement to accurately represent the geophysical parameters of sea ice during the advanced stages of the melt season (Tsamados et al., 2015). Additionally, reductions in sea ice have far-reaching consequences, influencing biochemical processes that affect the timing of ice algal and phytoplankton production and nutrient availability. These changes, in turn, have implications for marine food web dynamics and ecosystem structure (Meier et al., 2014). Beyond ecological impact, these intricate connections between changing sea ice conditions socioeconomical activities such as navigation, hunting, fishing, and ice travel, diminishing traditional knowledge (Pearce et al., 2015). In light of these changes, there is an urgent need for a deeper understanding of Arctic sea ice properties during the summer melt season and for continuous monitoring of the implications of a changing Arctic on climate dynamics, biogeochemical cycles, and ecological processes at both regional and global scales.

In the vast and remote Arctic, continuous sea ice monitoring relies heavily on satellite observations. Over the past 45 years, satellite passive microwave sensors have played a crucial role in supporting large-scale sea ice monitoring (Meier et al., 2014). However, passive microwave systems have limitations, particularly in providing essential regional-scale retrievals and summer sea ice observations. In contrast, Synthetic Aperture Radars (SAR) are active microwave sensors capable of operating under various weather and light conditions, allowing the detection of small-scale ice features such as ridges, small leads, and coastal polynyas (Dierking, 2013; Moreira et al., 2013). SAR datasets are particularly suited for advanced melt studies due to their operational characteristics, allowing both large-scale and local-scale monitoring. The availability of multi-frequency and

polarimetric data from SAR supports the development of innovative algorithms for monitoring sea ice properties (Drinkwater et al., 1991; Scheuchl et al., 2002; Shokr and Dabboor, 2023).

An increasing body of research has explored the relationship between SAR backscatter and the geophysical properties of sea ice in the melt season for ice type detection and classification (Scheuchl 2005; Dierking and Busche, 2006; Casey et al. 2016; Mahmud et al., 2020). The application of polarimetry to decipher ice type properties holds immense potential for enhancing sea ice classification and mapping during the melt season, leveraging various polarimetric features and decompositions (Dabboor and Geldsetzer 2014; Geldsetzer et al., 2015; Nasonova et al., 2018; Singha et al., 2020; He et al., 2022). Additionally, combining observations from the well-established C-band SAR with ones with lower frequency such as L-band, and polarimetric datasets, may help address ice type discrimination and classification challenges during the summer melt season (Dierking and Busche, 2007; Casey et al., 2016).

While literature supports the advantageous synergy of C- and L-band SAR frequencies for identifying ice types during the melt season, a comprehensive analysis akin to that presented by Casey et al. (2016) is scarce. The lack of a detailed analysis of the relationships of SAR backscatter and sea ice geophysical properties in the advanced melt season using multi-polarimetric and multi-frequency SAR represents a significant gap in our understanding, one that has the potential to greatly benefit operational and scientific aspects of sea ice research and advance our understanding of the future of Arctic sea ice.

1.2. Objectives

The primary objective of this research is to advance our understanding of the intricate relationships between the sea ice geophysical properties and the C- and L-band SAR microwave scattering during the advanced melt season. To achieve this objective, the following research subobjectives are addressed:

i) Examine the C- and L-band sea ice type backscatter and dominant scattering mechanism in the early and advanced melt season.

ii) Evaluate the utility of polarimetric parameters (fully and-or compact) for ice type separability in the early and advanced melt season.

iii) Assess the influence of melt ponds on SAR sea ice type separability in the advanced melt season.

iv) Investigate the influence of environmental conditions and variable incidence angle at each frequency and stage of the advanced melt.

v) Harness the extracted knowledge for sea ice type classification in the advanced melt, including the evaluation and classification of deformed ice.

Nevertheless, to effectively make use of multifrequency and multi-polarimetric data it is essential to have a thorough understanding of how the physical and electrical properties of summer sea ice relate to scattering mechanisms. To gain a complete understanding of the geophysical and microwave scattering properties of sea ice, it is imperative to consider its entire seasonal lifecycle and its connections to regional and global climate processes. The following sections introduce a brief description of sea ice properties and SAR remote sensing nomenclature.

1.3. Sea ice properties

Sea ice is a complex composite consisting of pure ice, brine, air, and salt crystals and plays a critical role in moderating energy transfer between the ocean and atmosphere (Figure 1.2) (Barry, 1989).

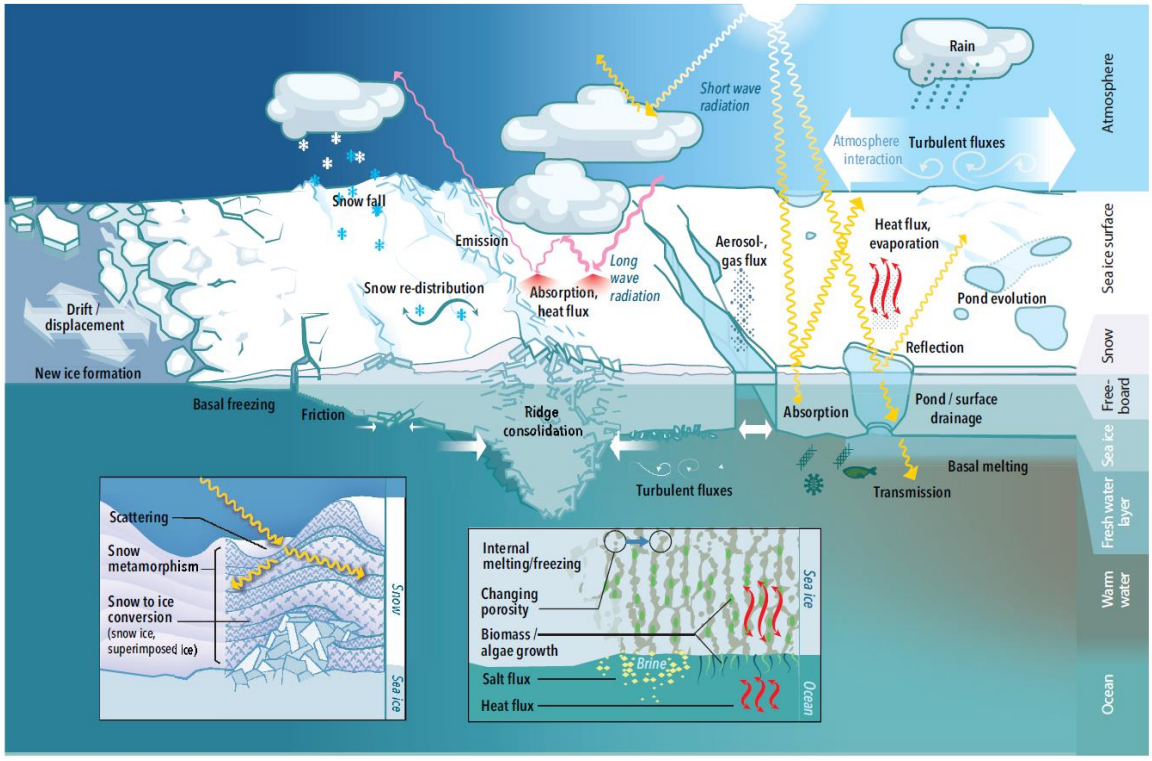

Figure 1.2: Schematic depicting the complex processes governing the Arctic snow and sea ice across the seasons. The close-ups focus on the snow–ice (left) and ice–ocean (right) interfaces. (Adapted from Nicolaus et al., 2020).

1.3.1. Sea ice types

According to the World Meteorological Organization (WMO, 2014), ice less than 10cm thick is categorized as 'New ice,' which includes various subtypes like frazil, grease, and nilas, with nilas being consolidated and elastic. As new ice thickens, it transitions through stages, starting with 'Young ice' (10-30cm) and progressing to 'First-year ice (FYI)' categorized into 'Thin' (30-70cm), 'Medium' (70-120cm), and 'Thick' (>120cm) stages. If it survives the summer melt, FYI eventually becomes 'Old ice' (≥3m), which includes both 'Second-year ice' and 'Multiyear ice (MYI),' depending on the number of melt seasons it has endured (Scharien, 2010). Distinguishing second-year ice from MYI, whether visually or in remote sensing datasets, is challenging due to their similar geophysical properties (Wadhams, 2000). Consequently, second-year ice is rarely mentioned in the literature, and the term 'MYI' is often used as a synonym for old ice. Deformed ice (DFI) is ice that has

in places been pressed upwards or downwards due to dynamic forces (WMO, 2014). This dissertation consistently employs this nomenclature.

1.3.2. Sea ice formation and growth

Sea ice formation is primarily driven by thermodynamics. It begins when the sea surface reaches its freezing point, giving rise to various ice structures, including frazil, grease ice, and nilas. These structures can further develop into pancake ice under the influence of ocean swell. In the Arctic Ocean, for a typical surface salinity of 32 ppt (parts per thousand by weight), the freezing point is approximately –1.8°C (Maykut, 1985). As new ice forms and consolidates, it creates an insulating barrier between the ocean and the atmosphere. Ice accretion then occurs through the congelation growth mechanism, where water molecules freeze onto the basal planes of existing ice crystals at the ice-water interface (Weeks and Ackley, 1986). Over time, platelet orientations shift from a disordered state to a predominantly vertical alignment, forming what is known as columnar ice. This type of ice dominates as it thickens seasonally, responding to thermal gradients and regulated by heat fluxes (Weeks and Gow, 1978; Petrich and Eicken, 2009).

The basal growth rate of sea ice depends on the temperature gradient across the ice sheet and its effective thermal conductivity. Greater temperature differences between the surface air and the ice base, which is at the salinity-adjusted freezing point, lead to increased heat conduction through the ice. This process is balanced by oceanic heat flow into the ice and latent heat release during ice growth (Wadhams, 2000). Consequently, as the temperature difference between the air-ice (or air-snow) interface and the ice-ocean interface remains constant, thicker ice sheets exhibit decreased ice growth rates due to reduced temperature gradients within the thickening ice.

Importantly, rapid desalination occurs during ice formation, trapping brine and gas within pure ice platelets at the crystalline boundary (Kovacs, 1996). As ice thickens, the growth rate decelerates, reducing the concentration of brine layers with depth. Seasonal brine drainage is driven by three distinctive mechanisms: i) brine cell migration, where brine pockets move along the thermal gradient within the ice sheet, directed toward the warmer

ocean water below, ii) brine expulsion, occurring when thermal contraction in the ice ruptures a brine pocket wall, causing the brine to move upward or downward through the ice sheet, and iii) gravity drainage, which occurs as an ice sheet grows and elevates above sea level, creating a pressure gradient that compels brine to migrate through fine pores toward the base of the ice sheet (Cox and Weeks, 1975; Wadhams, 2000). This seasonal brine drainage results in a salinity depth profile that resembles a reverse C-shape and diminishes with time (Maykut, 1985). Various factors, such as the insulating properties of snow cover and ice dynamics, further complicate the system, introducing micro to macro-scale variations in ice and brine structures (Scharien, 2010).

During freeze-up and winter, atmospheric forcing drives processes of snow and sea ice growth, structure development, and brine drainage, creating a strong temperature gradient. Early melt, initiated by sunlight and diurnal temperature variations, primarily affects the snowpack rather than ice volume. Freeze-thaw cycles induce stratification within the snowpack, accompanied by kinetic changes driven by wind (Colbeck, 1982; Shokr and Barber, 1994). In the summer, sea ice desalination intensifies, expanding brine cells and enhancing their interconnectivity and gravity drainage. Surface conditions become highly variable due to interactions with the ocean-sea ice and atmospheric interfaces. The detailed stages of ice phenology in the melt season are described in the following section.

1.3.3. Sea ice in the melt season

With the rise of air or sea surface temperatures, the surface energy balance becomes positive thus snow and sea ice undergo warming and melting. The melting point of saline (brine-wetted) snow is below 0°C, allowing for melting even at surface air temperatures as low as approximately -5°C (Golden, 2001). The summer melt season is typically characterized by three stages: *early melt*, *melt onset*, and *advanced melt* (Livingstone et al., 1987; Barber et al., 2001).

Early melt signifies the onset of increasing solar radiation and atmospheric forcing, leading to snowpack warming and the rapid growth of snow grains. During this time, high shortwave flux downwelling impacts the snow volume and liquid water may appear in the

snowpack during the day (Shokr and Barber, 1994; Barber et al., 2001). The most notable aspect of snow thermodynamics is the change in the physical properties of the snow volume. The Earth-Sun geometry induces a diurnal shortwave flux pattern, leading to a diurnal temperature variability within the snow (Barber et al., 2001).

Melt onset (MO), follows when a sustained positive surface energy balance is achieved, and liquid water persists throughout the diurnal cycle, initially held within the snowpack pore volume until reaching about 7% volumetric water content, causing drainage to the base (transition from the pendular to funicular snowmelt regime). Most of the snow cover becomes saturated at the end of this season (Tiuri et al. 1984; Barber et al., 2001).

Advanced melt encompasses daily average air temperatures exceeding 0°C, leading to isothermal snow and ice conditions and the development of melt ponds on the ice surface. As melt ponds form, the ice surface topography becomes undulating. Once the ice reaches an isothermal state with well-established brine drainage networks, melt ponds start draining, resulting in a deteriorated, low-density, and low-salinity ice cover, significantly reducing its strength (Figure 1.3) (Wadhams, 2000; Barber et al., 2001; De Abreu et al., 2001). The advanced melt can be subdivided into 3 distinct substages in the context of melt pond evolution: Pond Onset (PO), Pond Evolution (PE) and Pond Drainage (PD).

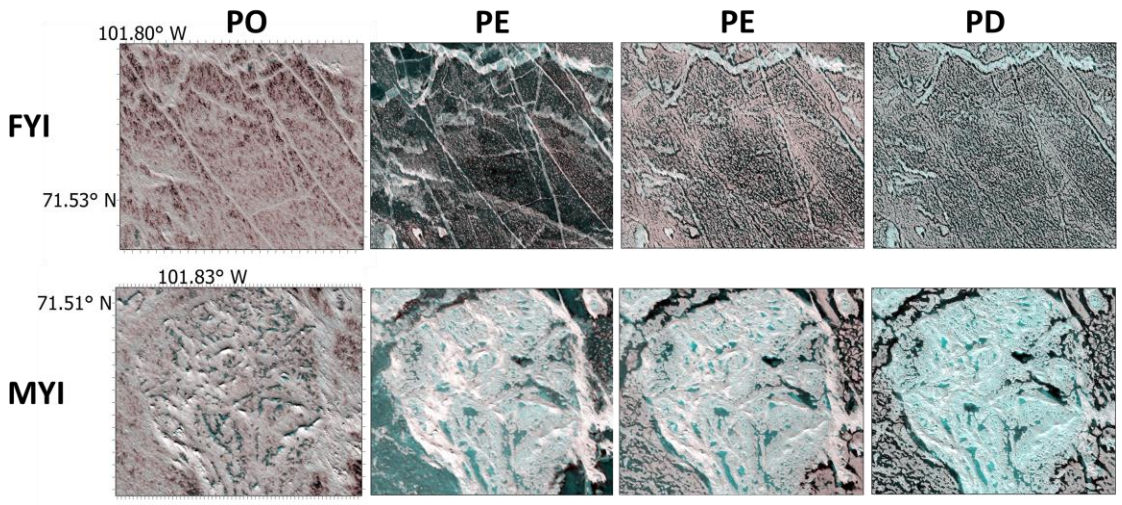

Figure 1.3: Optical high-resolution images (VIS-RGB) depicting smooth FYI and MYI regions in the Canadian Arctic Archipelago. Each advanced melt stage is shown portraying changes in ice type surface properties.

In PO, ponds are form in shallow depressions near snow drifts due to the accumulation of liquid water from snowmelt surpassing the gravitational drainage rate within the underlying ice (Barber and Nghiem, 1999). Smooth FYI presents higher melt pond fraction (MPF) (from 20 to 60%) than MYI (≤ 30%) (Figure 1.3) (Eicken et al., 2004). Meltwater flushes the liquid brine, causing a rapid desalination of the upper ice layers. As water percolates downwards in the snow, it disperses and freezes when it reaches the cold ice surface, forming a rough, superimposed ice layer. This layer is much rougher compared to the winter surface of FYI (Onstott, 1992). Depending on snow cover distribution and ablation, melt ponds in proximity expand in size.

During PE, snow cover has melted, leading to maximum MPF and exposing the superimposed ice layer. During this phase, the desalinated upper portion of the ice sheet, ranging from 5-20 cm in thickness, comprises two desalinated layers: the drained ice layer (DL), characterized by porous, white ice that remains relatively constant throughout the melt season, and the surface granular layer (SL), a 1-3 cm thick layer of loose, decomposing grains formed from the friable top portion of the DL when exposed to sufficient penetrative

solar radiation (Perovich et al., 2001; Grenfell and Perovich, 2004). The fractional coverage of melt ponds during the peak phase is influenced by an imbalance between diurnal ice ablation rates and lateral meltwater drainage processes, which can occur via cracks, leads, or within the ice volume (Eicken et al., 2004). Additionally, ice permeability plays a significant role, as impermeable fresh ice layers in the upper ice sheet can impede vertical drainage of meltwater, leading to variable melt pond coverage on a diurnal scale, gradually decreasing as the ice becomes more porous (Freitag and Eicken, 2003).

PD begins when the ice becomes permeable to fluid transport characterized by a decrease in MPF due to enhanced gravity drainage of meltwater. Once the ice reaches an isothermal state and the brine drainage networks become fully interconnected, rapid drainage takes place, often within a matter of hours. While freshwater melt pond drainage occurs, seawater replenishment may occur in regions where the ice descends below the freeboard level (Eicken et al., 2004). This phase results in the near structural indistinctiveness of FYI compared to the above-freeboard layer of MYI (Eicken et al., 1995). Dynamic processes play a significant role in ice breakup, capable of either accelerating or delaying the timing of ice breakup primarily driven by thermodynamics. In the absence of a dynamic mechanism, a deteriorating grid of decaying FYI and saltwater melt ponds persists until complete ice melt or a subsequent seasonal freeze-up, with breakup potentially induced by dynamic factors such as high winds.

1.3.4. Deformed sea ice

In addition to thermodynamic processes, dynamic forces play a significant role in shaping the structure and thickness distribution of sea ice (Hibler, 1986; Perovich et al., 2001). These dynamic forces are responsible for various phenomena, including cracks, leads, and polynyas, which create open water areas in the ice cover. When the surface energy budget is negative, these open water regions begin to freeze, forming new ice. Conversely, convergent ice motion causes stress within the ice cover, leading to deformation. Deformed ice experiences both upward and downward displacement due to pressure, in contrast to level ice, which remains unaltered (WMO, 2014). This deformation not only affects the surface roughness but also increases the thickness of the sea ice cover.

The porosity of sea ice, which refers to the volume of brine and gas bubbles trapped within the ice, is closely related to its mechanical strength. Warmer ice contains more brine, resulting in higher porosity and reduced mechanical strength compared to colder ice with the same salinity (Petrich and Eicken, 2009). As Arctic sea ice continues to diminish, and the summer marginal ice zone (MIZ) extends northward (Strong and Rigor, 2013), the dynamics of sea ice are changing. Some dynamic behaviors that were once exclusive to summer are now occurring in autumn or spring due to an extended ice melt season. This suggests that the evolving Arctic sea ice is becoming more similar to the dynamics observed in Antarctica (Lei et al., 2020).

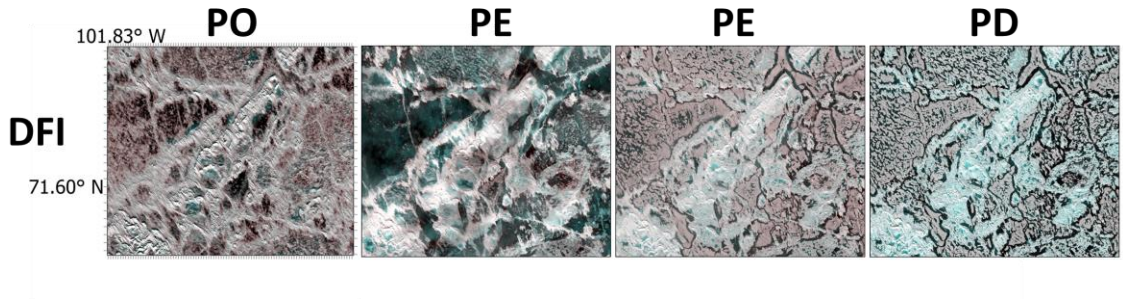

Figure 1.4: Optical high-resolution images (VIS-RGB) depicting a region of deformed ice in the Canadian Arctic Archipelago. Each advanced melt stage is shown, portraying changes in ice type surface properties.

In the early melt season, deformation features exhibit similar patterns for FYI and MYI types. At the end of the advanced melt, both types become porous and thinner, becoming susceptible to deformation (Kwok and Cunningham 2012). Deformation features are characterized by higher surface roughness that persists across the advanced melt season, as illustrated in Figure 1.4. This enhanced surface roughness could potentially facilitate improved detection of these ice types in the advanced melt season.

1.4. Sea ice importance for global climate processes

The interaction of the atmosphere, sea ice, and ocean processes under the influence of global climate forcing exhibits complex and non-linear behaviors (Goosse et al., 2018; Sumata et al., 2023). Sea ice, a crucial indicator of the Arctic climate state, undergoes inter-annual and seasonal variations driven by energy, humidity, heat, and gas fluxes (Perovich et al., 2007; Meier et al., 2014). These variations in sea ice extent, type, and thickness have far-reaching impacts on regional and global atmospheric and oceanic systems. Understanding and monitoring these mechanisms are essential for isolating their roles and assessing their overall impact.

The atmosphere, sea ice, and ocean system are characterized by positive feedback loops that predominantly amplify trends in sea ice components (Perovich et al., 2007; Meier et al., 2014; Döscher et al., 2014). Pressure patterns and winds, influenced by broader climatic changes, significantly affect the state of sea ice and its inter-annual variability. Oceanic factors, such as increased open water areas, are linked to modifications in large-scale atmospheric circulation patterns. One of the most notable feedback mechanisms is the surface albedo feedback, driven by thermodynamic interactions. It occurs as melting sea ice reduces surface reflectivity, leading to increased solar radiation absorption and extended ice melt. The sea ice-albedo feedback can reinforce Arctic amplification (Döscher et al., 2014), which, in turn, has been linked to global atmospheric temperature rise and increased greenhouse gas concentrations (Gillet et al., 2008; Notz and Marotzke, 2012).

Two prominent climatic patterns, the Arctic Oscillation (AO) and the North Atlantic Oscillation (NAO), exert significant influence on both Arctic and global climate dynamics. The AO is characterized by a counterclockwise wind pattern, which has notable effects on colder air masses and storms in the Arctic (Thompson and Wallace, 1998). Conversely, the NAO governs atmospheric pressure patterns in the North Atlantic. While both patterns influence Arctic sea ice, the AO exhibits a slightly stronger correlation, explaining over 53% of its variability (Wang and Ikeda, 2000). The influence of AO on Arctic sea ice is multifaceted. It affects sea level pressure and sea ice motion in the Arctic, thereby influencing critical features like the Beaufort Gyre and the Transpolar Drift Stream. These

features, in turn, control ice circulation, transport, and formation in various AO phases. During a positive AO phase, thinner ice formation prevails, often resulting in negative anomalies in summer sea ice extent. Conversely, a negative AO phase promotes sea ice survival and thickening, especially in regions such as the Canadian Arctic (Kwok, 2006; Spreen et al., 2011). High AO phases are associated with increased sea ice divergence, facilitating enhanced heat transport from the ocean in winter. This process leads to the formation of leads in areas like the East Siberian and contributes to reduced sea ice extent and thickness over the Arctic Ocean (Rothrock et al., 1999). Moreover, the exchange of sea ice within the Canadian Arctic Archipelago (CAA) is positively correlated with AO indices. During high AO phases, more sea ice flows from the Arctic Ocean to the CAA, resulting in a notably higher net sea ice flux in the Queen Elizabeth Islands region from 2005-2012 compared to 1997-2004 (Howell et al., 2013). Understanding the intricate relationship between climate feedbacks and Arctic sea ice dynamics is essential for comprehending the broader implications of these climatic patterns on the Arctic environment and its global repercussions.

1.5. Current state of sea ice

In recent years, researchers have investigated the potential for the Arctic sea ice system to reach a tipping point under extreme warming conditions, as suggested by modeling simulations based on historical sea ice minima. The vulnerability of such scenarios hinges on complex interactions among feedback mechanisms. A recent publication from Johannessen and Shalina, (2023) emphasized that there is a strong relationship between CO_2 levels and Arctic sea ice extent, and that a tipping point scenario is less likely to occur if the CO_2 emission targets of the Paris agreement are reached. Nonetheless, it's essential to consider that natural variability will continue to impact the thinner Arctic sea ice, complicating efforts to fully understand and predict seasonal and inter-annual variability (Goosse et al., 2009; Johannessen and Shalina, 2023).

1.5.1. Sea ice in the Canadian Arctic Archipelago

The CAA encompasses islands on the North American continental shelf. Sea ice in this region includes ice trapped around the islands and pack ice in the adjacent Canadian Basin. Throughout winter, CAA is predominantly covered by landfast ice, which breaks apart during the summer months. FYI accounts for up to 87% of the total ice cover, while the western part of the archipelago contains as much as 50% MYI due to persistently low temperatures in winter and spring (Howell et al., 2010). Studies have highlighted a thinning of the snowpack in the Western Arctic over the past decade (Giles et al., 2008; Webster et al., 2014). This thinning is linked to increased atmospheric moisture content, impacting precipitation rates, and resulting in delayed and thinner sea ice cover. Howell et al. (2015) found that MYI replacement within the CAA is influenced by various factors, including approximately 10% FYI aging in the Arctic Ocean, around 50% MYI exchange from Nares Strait outflow to Baffin Bay, and roughly 12% from Fram Strait outflow to the Greenland Sea.

In the summer season, sea ice in the CAA has decreased by 4.8% per decade from 1968 to 2016 (Derksen et al., 2018). Additionally, the duration of the melt season in CAA shown an increase of 5.1 days per decade from 1979 to 2018 (Figure 1.5). This leads to earlier ice breakup and delayed formation of ice with more open water, allowing for the accommodation of ice entering the CAA from the Arctic Ocean during the melt season (Howell and Brady 2019). Understanding ice dynamics and thermodynamics in the CAA and the potential implication for the broader Arctic region is essential for assessing the ongoing changes in the Arctic sea ice system.

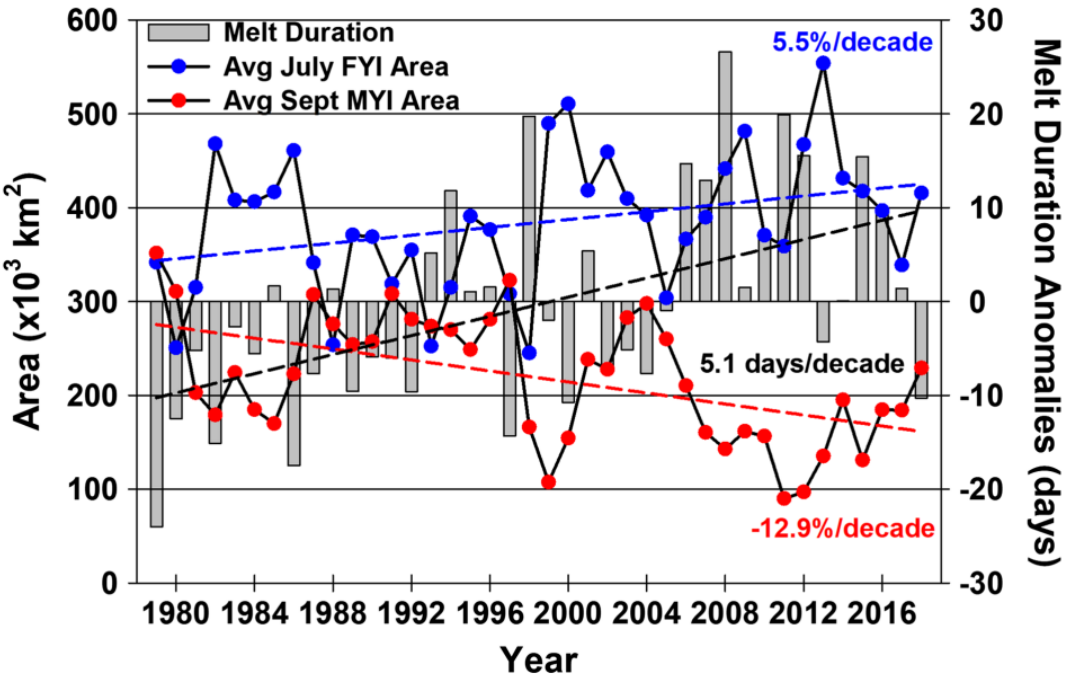

Figure 1.5: Time series and trends of average July seasonal FYI, average September MYI and melt season duration anomalies in the Canadian Arctic Archipelago from 1979 to 2018. (Adapted from Howell and Brady 2019).

1.6. Sea ice monitoring using Synthetic Aperture Radar

Satellite remote sensing systems, including microwave radiometers, scatterometers, and altimeters, offer valuable observations of Arctic sea ice parameters, albeit at coarser spatial resolutions (Dierking, 2013; Meier et al., 2014). SAR systems operate under various conditions, with swath widths ranging from 30 to 500 km and spatial resolutions from 1 to 100m, making them suitable for regional sea ice analysis and validation of lower-resolution data and numerical models (Dierking, 2013). SAR sensors measure variations in backscatter signals over the sea ice and can effectively map its dynamic and thermodynamic properties. Numerous studies (Nghiem and Bertola, 2001; Geldsetzer and Yackel, 2009; Singha et al.,2020; He et al., 2022) have been conducted in recent decades to monitor sea ice properties using SAR. However, their performance is heavily influenced by regional characteristics and environmental conditions, such as wind fields and local

climatology. Additionally, research has explored the potential of sensor parameters, including incidence angle, frequency, and polarization, for sea ice classification purposes (Drinkwater, 1992; Scheuchl et al., 2005; Gill and Yackel, 2012). A key insight from this body of work is that the backscatter response from different ice types is dependent on radar parameters, the dielectric properties of sea ice, and sea ice geophysical properties (Ulaby et al., 1986).

Polarimetric SAR provide insights into sea ice variables and scattering mechanisms, aiding in environmental parameter estimation (Dabboor and Geldsetzer, 2014; Moen et al., 2015). In conventional SAR, these mechanisms are challenging to differentiate. However, fully polarimetric SAR, which includes both magnitude and phase, allows the identification of three distinct radar scattering mechanisms: single-bounce scattering (surface), double-bounce scattering, and random (volume) scattering. Single-bounce scattering occurs on surfaces with low roughness, spheres, or trihedral reflectors. Double-bounce scattering involves two surfaces at right angles to each other, preserving the incident wave's polarization but changing its sign. Random scattering, associated with depolarization, arises from surfaces with structure or heterogeneous volumes containing numerous scattering elements (Ulaby et al., 1986; Shokr and Sinha 2023). Sea ice applications involve single-bounce scattering from level young ice or FYI surfaces, random scattering from deformed surfaces with ridges, rubble fields, or multiple scattering elements like air bubbles in MYI, and double-bounce scattering at ice shelf edges or sharp sea ice floe edges. The local incidence angle of the radar beam affects the dominant scattering mechanism, depending on the sensor's viewing angle relative to the ice block arrangement (Raney, 2007; Raney and Freeman, 2011). Fully or compact polarimetric datasets support additional information about target properties such as shape orientation and dielectric properties, and signal decompositions have been widely used for sea ice detection and classification (Dabboor and Geldsetzer 2014; Ressel et al., 2015; Singha and Ressel 2017; Zakhvatkina et al., 2019; He et al. 2022).

Polarimetric parameter analysis enhances comprehension of scattering interactions at various sea ice stages, with existing approaches indicating significant potential in leveraging advanced SAR data for sea ice retrievals (Cloude and Pottier 1997;

Charbonneau et al., 2010; Gill and Yackel 2012; Dabboor and Geldsetzer 2014). However, a small number of studies examine polarimetric parameters for mapping of sea ice geophysical properties during advanced melt, due to limited polarimetric spatiotemporal data availability. Fully polarimetric SAR data have high spatial resolution (10m) but provide limited regional information (~25km), restricting the possibility of operational and wide exploitation of the existing techniques. The launch of the RADARSAT Constellation Mission (RCM) created a new SAR data era, providing compact polarimetric data over the Arctic, with significantly wider swaths (500 km in some imaging modes) and satisfactory spatial resolution (30 to 100 m). Therefore, further research is needed to analyze and compare compact polarimetric data with fully polarimetric data to establish frameworks for sea ice monitoring, especially during the advanced melt season.

1.6.1. Sea ice dielectric properties and penetration depth

In the context of microwave remote sensing, the relative permittivity and dielectric loss factor are fundamental parameters used to describe how microwave signals interact with a dielectric medium like sea ice. The dielectric permittivity describes how readily the microwave energy passes across a dielectric interface such as air to water, while the dielectric loss factor quantifies the amount of the absorbed or lost energy after passing through the interface. These parameters determine the penetration depth, which signifies the depth at which radiative power is absorbed after crossing the air-water interface (Ulaby et al., 1986). Additionally, the dielectric properties of sea ice are further influenced by the presence of a snowpack, contributing the dielectric constant of dry snow during the winter, as well as its loss factor (Geldsetzer et al., 2009). Figure 1.6 presents the penetration depth differences between SAR sensors in the winter season. Sensors with longer wavelengths, such as L-band (λ= 23cm) and P-band (λ= 50cm), offer greater penetration depth, resulting in signals that provide insights into volume scattering and subsurface conditions. This contrasts with shorter and medium wavelength systems like X-band (λ= 3cm) and C-band (λ= 5cm), which are more sensitive to surface scattering.

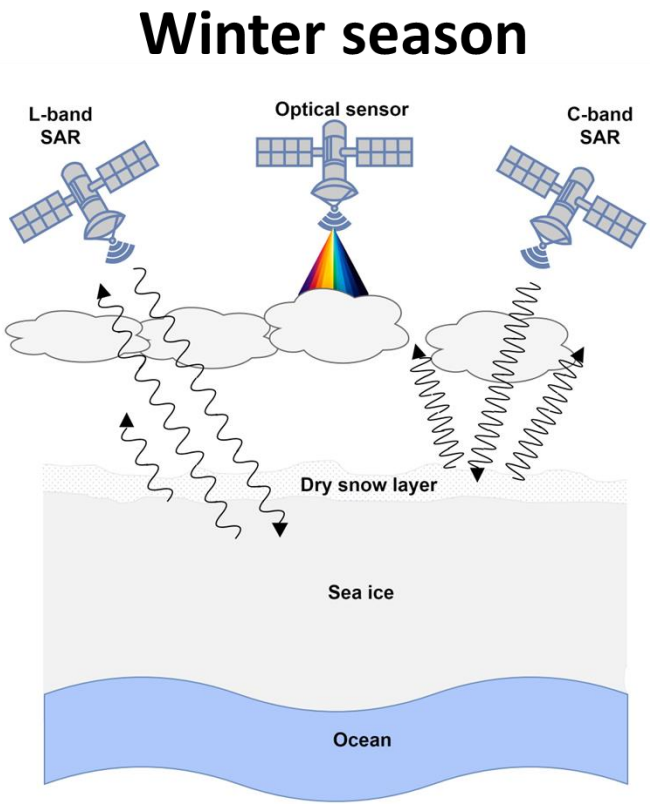

Figure 1.6: Comparison of passive optical satellite sensors with active SAR sensors of different frequencies for sea ice monitoring in the wintertime. Lower frequency SAR (L-band) is characterized by higher penetration depth compared to C-band SAR in dry snow conditions.

Wet snow influences the dielectric properties of sea ice during the onset and advanced stages of melting. As wetness and frequency increase, the microwave signal penetration depth decreases (Figure 1.7). Research conducted in the Fram Strait during the 1980s indicated that the penetration depth for L-band SAR in the melt season reached approximately 1 m, whereas for C-band, it was limited to 5 cm (Onstott, 1987). C-band SAR sensors have been the primary tool for sea ice monitoring since the 1990s. However, their effectiveness decreases during the melt season, and surface moisture obscures the distinction between first-year ice (FYI) and multi-year ice (MYI). L-band sensors, with longer wavelength, are more effective in differentiating between FYI and MYI during advanced melt stages, as evidenced by research from Dierking and Busche (2006) and Casey et al. (2016). Despite the proven capabilities of L-band SAR in other environmental

contexts, its application in sea ice research remains underutilized, presenting opportunities for improved monitoring strategies. The launch of satellites like ALOS-2 and upcoming missions, including NISAR and ROSE-L, underline the increasing relevance of L-band SAR and its potential for expanded data availability in the near future.

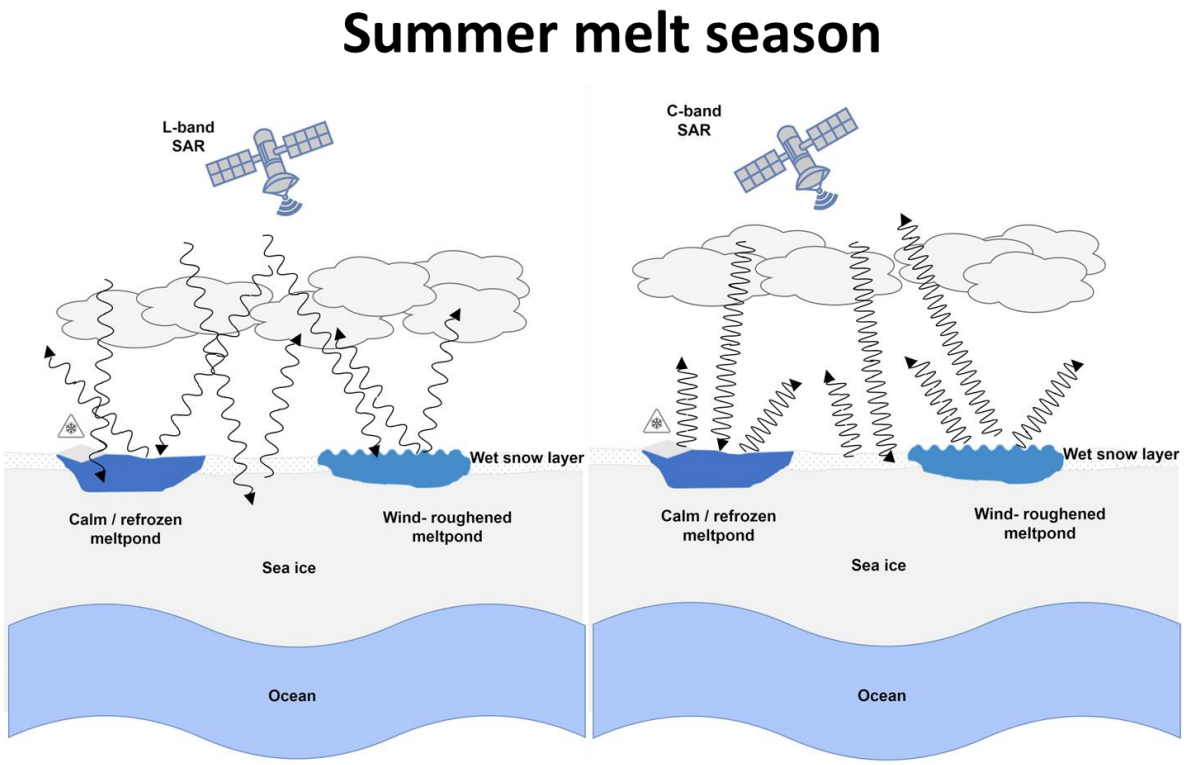

Figure 1.7: Comparison of SAR sensor frequencies for sea ice monitoring in the summertime. Lower frequency SAR is characterized by higher penetration depth compared to C-band SAR however, the presence of melt ponds impedes signal penetration at both frequencies.

1.7. Dissertation outline

This dissertation contains four chapters and one appendix. Chapter 2 investigates sea ice type separability in the summer melt season utilizing C- and L-band SAR data. The material in Chapter 2 has undergone peer review and has been published in the Canadian

Journal of Remote Sensing. Chapter 3 presents a sea ice type classification scheme in the advanced melt season using a random forest algorithm. A synergistic C- and L-band classification model is being suggested, supporting commonly available polarizations for classifying FYI, MYI and DFI. Chapter 3 is submitted to the Journal Remote Sensing of Environment. Chapter 4 provides a summary of results and concluding remarks. Suggestions for further research and future work and limitations are also presented. Appendix A includes supplementary materials and tables from chapter 2 and detailed co-author contributions. This dissertation is manuscript-based, thus some of the introduction and method sections within the chapters might be redundant.

Chapter 2. Melt Season Arctic Sea Ice Type Separability Using Fully and Compact Polarimetric C- and L-band Synthetic Aperture Radar

Abstract

Sea ice mapping using Synthetic Aperture Radar (SAR) in the melt season poses challenges, due to wet snow and melt ponds complicating sea ice type separability. To address this, we analyzed fully polarimetric (FP) and simulated compact polarimetric (CP) C- (RADARSAT-2) and L- (ALOS-2 PALSAR-2) band SAR, in the 2018 melt season in the Canadian Arctic Archipelago, for stage-wise separation of first year ice (FYI) and multiyear ice (MYI). SAR scenes at both near- (19.1-28.3º) and far- (35.8-42.1º) range incidence angles and coincident high-resolution optical scenes were used to assess the impact of surface melt ponds on separability within a landfast ice zone of diverse ice thickness. C-band provided better separability between FYI and MYI during pond onset, while L-band was superior during pond drainage due to MYI volumetric scattering. CP parameters matched FP performance across the melt season. HH and HV, commonly offered in ScanSAR mode for both frequencies, presented good separability during pond onset and drainage. Using both C-band and L-band SAR along with constraining incidence angle ranges, enhances sea ice type identification and separability. Our results can support ice type classification and seasonal stage detection for climate studies and enhance existing frameworks for ice motion vector retrievals.

2.1. Introduction

Observations of the last four decades indicate that Arctic sea ice is declining in age, thickness, and extent (Maslanik et al. 2007; Meier et al. 2014). This new ice regime represents a shift from thicker MYI to thinner, seasonally decaying, FYI (Kwok and Rothrock, 2009; Laxon et al. 2013; Sumata et al. 2023). Particularly, Arctic sea ice extent decline has been most pronounced in the summer, with earlier and longer melt seasons accelerating sea ice loss (Markus et al. 2009; Stroeve and Notz, 2015).

In the melt season, the sea ice conditions exhibit considerable heterogeneity, due to the melting of snow and the formation of melt ponds. Diverse patterns in melt pond formation and evolution manifest depending on the ice type. Generally, the smoother, undeformed FYI is characterized by higher MPF compared to the rougher and undulated MYI (Eicken et al. 2004; Scharien and Yackel, 2005; Polashenski et al. 2012). The presence of melt ponds exerts a significant influence on ice dynamics, reduces the ice's albedo, intensifying heat absorption, and accelerating ice melting (Perovich et al. 2002). Hence, studying the surface conditions in the melt season, especially for distinguishing FYI from MYI, can improve sea ice forecasting and mapping.

Field observations during the melt season are often confined to specific regions, while optical remote sensing is limited by cloud coverage (Perovich et al. 2002; Webster et al. 2022). To address these challenges, active microwave sensors, particularly SAR, offer a compelling alternative. SAR is unaffected by light and cloud cover and allows for high spatiotemporal coverage (Scharien et al. 2014; Howell et al. 2020). Additionally, the potential of using multi-frequency and multi-polarization SAR data for sea ice retrievals in challenging sea ice regimes, such as the advanced melt and freeze-up, has been demonstrated (Onstott et al. 1985; Scheuchl et al. 2002; Dierking and Busche, 2006; Casey et al. 2016; Singha et al. 2018).

Traditionally, C-band frequencies, have been used for their adeptness in distinguishing between thicker, older ice and thinner ice types. For C-band SAR the measured radar backscatter from snow-covered sea ice is a function of snow grain size, brine volume, and

roughness at the snow ice interface, hence MYI and FYI backscatter signatures are distinct in the winter. As temperatures rise during the melt season, liquid water in the snowpack and the upper ice layer reduces the microwave signal penetration and ice type differentiation. In contrast, lower SAR frequencies, such as L-band, allow for greater signal penetration depth through wet snow, thus enabling scattering responses from the upper ice layer (Dierking and Busche, 2006). Despite previous research recognizing the value of multifrequency polarimetric parameters for sea ice mapping and classification (Scheuchl et al. 2002; Dierking and Dall 2007; Gill and Yackel, 2012; Dabboor et al. 2017; Singha et al. 2020), the exploration of combined C- and L-band SAR sea ice signatures during the melt season is limited to dual-polarization acquisitions (Casey et al. 2016; Mahmud et al. 2020).

Backscatter for common single and dual-polarization SAR channels, is highly variable during melt conditions due to surface heterogeneity, leading to limited reliable ice observations (Livingstone et al. 1987; Yackel et al. 2007). The presence of liquid water alters dielectric permittivity, and fluctuations in wind-wave induced surface roughness from melt ponds on open water often result in overlapping HH and HV signatures from FYI and MYI (Barber et al. 2001). A promising alternative uses FP SAR, which employs four linear backscatter channels (HH+HV+VH+VV) and relative phase measurements to comprehensively characterize a target's polarimetric response. This mode offers a range of sea ice geophysical information, showcasing its potential for ice type separability and classification during the melt season (Fors et al. 2016; Singha et al. 2020; He et al. 2022). The wider application of FP mode data for both frequencies to understanding sea ice properties during melt has been largely limited by narrow (≤50km) achievable swath widths compared to single or dual-pol modes (Geldsetzer et al. 2015). Additionally, outside of open-access missions such as Sentinel-1 (dual-pol), data from both C- and L-band SAR missions are limited by access restraints.

Conversely, CP offers a good tradeoff between the scattering information provided by FP, and capability of acquiring data over wide swaths (Charbonneau, 2010; Geldsetzer, et al. 2015; Espeseth et al. 2017). In CP, a circularly polarized wave is transmitted, and coherent vertical and horizontal linear polarized waves are received, providing relative phase

information for polarimetric decompositions akin to FP (Raney, 2006; Dubois-Fernandez et al. 2008; Cloude 2012). While several studies have examined the CP parameter potential for sea ice mapping and classification during winter and freeze-up periods (Li and Perrie 2016; Espeseth et al. 2017; Singha and Ressel 2017), a comprehensive analysis of CP parameter relationships across all melt stages is lacking (Dabboor and Geldsetzer, 2014; Geldsetzer et al. 2015).

Geldsetzer et. al (2015) and Nasonova et al. (2018) used simulated CP data for C-band in the summer, showing that parameters sensitive to surface scattering and depolarization effectively separated FYI from MYI samples. Components of the mχ decomposition and the Stokes vectors exhibited good separation in both near range (NR) and far range (FR) incidence angles. NR acquisitions presented enhanced contrast owing to their sensitivity to Bragg scattering from wind-roughened melt ponds, accentuating differences in sea ice type-related melt pond fraction. Nonetheless, a detailed stage-wise analysis of ice type separability in the advanced melt remains unexplored. Furthermore, the assessment of simulated L-band CP data within the context sea ice variability in the melt season is limited. Future missions like Copernicus ROSE-L, NASA-ISRO SAR (NISAR), and ALOS-4 PALSAR-3 from JAXA, offer the potential for L-band data exploration, complementing existing C-band polarimetric data with high spatial resolution, in both FP and CP modes from the RCM.

For this work, we use FP and simulated CP polarimetric data from C- and L-band frequencies to study early and advanced melt stages and address a knowledge gap in understanding FYI and MYI separability in the summer. Our analysis covers the 2018 melt season in the CAA and focuses on three main research questions:

1. Which frequency, C- or L-band, offers enhanced separability between FYI and MYI in advanced melt?
2. How do CP parameters compare to FP, for FYI and MYI type separability at each melt stage?
3. What is the role of melt ponds in the observed backscatter variability?

To address these questions, we investigate the relative scattering mechanisms of FYI and MYI during late winter, melt onset and advanced melt (defined below), and explore the role of surface melt ponds as a driving factor of observed changes in the advanced melt. Additionally, we study the impact of radar parameters, such as incidence angle and frequency, on ice type separability and scattering mechanisms during the melt season. Section 2.2 describes the seasonally-evolving sea ice surface conditions, defining each seasonal stage and substage addressed in this study. We then provide details about the study site, C- and L-band SAR datasets, high-resolution satellite optical data of melt pond covered sea ice, and ancillary datasets. Data processing and the framework for analysis is provided in Section 2.3, followed by results in Section 2.4. Summary and conclusions are given in Section 2.5.

2.2. Seasonal stages, Study site and Data

2.2.1. Seasonal stages

In this study, the period pre-ceding melt is defined as *late winter* (LW) and two distinct stages comprising melt conditions are MO and *advanced* melt. MO on sea ice has been previously defined as the time when the surface temperature is above $-1^{O}C$ for more than five consecutive days. During MO, the transition from the pendular and funicular regimes leads to an increasing snow wetness and snow metamorphism (Tiuri et al. 1984). The presence of liquid water within the snow and ice volume, alters the dielectric properties of snow and ice, and results in the convergence of previously contrasting single-polarization C-band backscatter from FYI and MYI. The advanced melt season, defined as the period after MO when the sea ice volume is isothermal and surface melt ponds form, is characterized by variable combinations of melting snow, bare ice, and melt pond covered ice. As mentioned in Section 1, this leads to C-band backscatter ambiguity (Barber et al. 2001).

Advanced melt is further divided into three substages, i) PO, defined as the initial period of melt pond formation, where the pond formation and evolution is driven by melting snow, and the relatively rapid melt water influx, combined with variations in surface topography

between FYI and MYI can result in a large contrast in MPF (i.e., widespread ponding on FYI and topographically limited ponding on MYI); ii) PE, after the meteoric snow cover has ablated and sea ice is composed of melt pond water and bare ice; melt pond fraction is driven by competing melt water input and drainage sources, particularly on FYI where a network of interconnected melt ponds is formed, and enhancing drainage occurs into cracks and flaws, and iii) PD, where the FYI has become porous enough that melt water is vertically transported through the ice volume through drainage channels to the ocean (Weeks and Ackley, 1986; Eicken et al. 2002; Polashenski et al. 2012). During PD, the MPF on FYI decreases rapidly when the melt pond surfaces are above the ice freeboard line, and increases again when they reach the sea level. Importantly, PD is a pre-cursor to FYI break up as it occurs when the ice is isothermal and structurally weak (Eicken et al. 2002, 2004). FYI and MYI differ mainly in permeability, with the less permeable MYI retaining more melt ponds, in some cases into the subsequent freeze-up period (Eicken, 2002).

Overall, these substages provide an intuitive framework for evaluating key C- and L-band scattering differences between FYI and MYI, and backscatter changes in the context of seasonally evolving sea ice properties. It is acknowledged that these sub-stages are not discrete, e.g., a greater snow depth on MYI compared to FYI will result in a later transition from PO to PE for that ice type.

2.2.2. Study site

Data were acquired from M'Clintock Channel in the southwestern CAA in 2018 (Figure 2.1a), as part of an effort to characterize the seasonal evolution of sea ice physical and electromagnetic properties, including evaluating the utility of C- and L-band SAR for sea ice geophysical information retrievals (Scharien et al. 2018). This location comprises a combination of thermodynamically grown FYI, MYI and deformed ice, all of which become land-fast from winter until break up, normally in July (Canadian Ice Service, 2011).

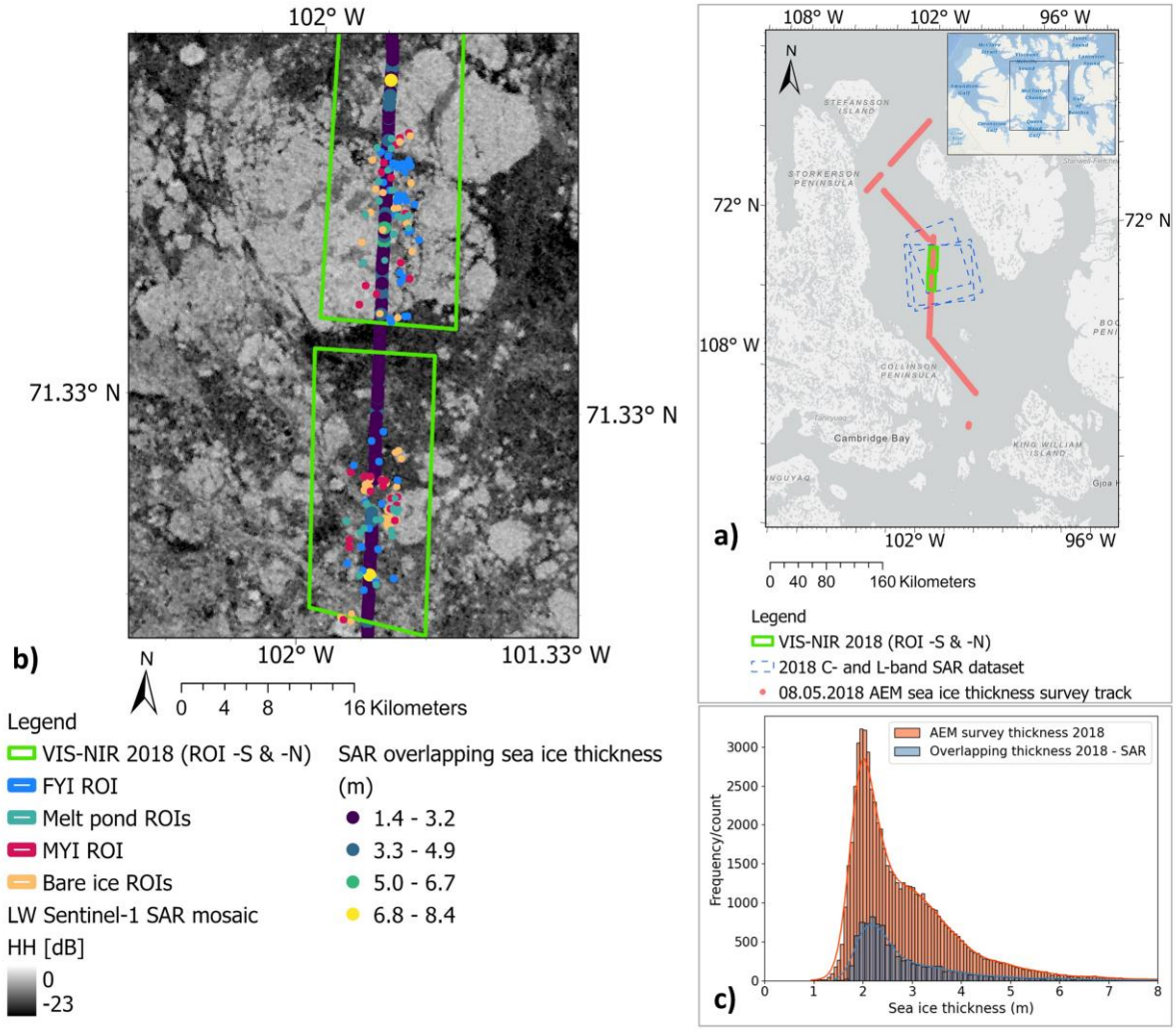

Figure 2.1: a) Study area map showing the southwestern CAA. Areal extents of C- and L-band SAR images and optical scenes are shown along with an AEM sea ice thickness track. b) A LW SAR image showing the ice thickness data and ROIs used for aggregating scattering data across all seasons. c) Histograms of ice thickness derived from the complete survey track (orange) and the segment that coincides with SAR acquisitions (blue).

Sea ice in this region is therefore characterized by a broad spectrum of roughness and thickness during the late winter and is ideal for establishing seasonal linkages with SAR backscatter since the same ice can be tracked from pre-melt through advanced melt without requiring ice motion tracking. Based on the histogram from an AEM survey on 8 May 2018 (Figure 2.1c), the snow plus ice thickness ranges from approximately 1 m to 8 m for the complete survey track, while the track portions overlapping with SAR datasets range from approximately 1.7 m to 7m. The AEM survey configuration is detailed in Section 2.3.4.

2.2.3. SAR and Optical datasets

Details of the SAR and high-resolution optical image datasets are provided in Table 2.1. We analyzed 10 C-band (5.4 GHz) RADARSAT-2 (RS2), and 3 L-band (1.27 GHz) ALOS-2/PALSAR-2 (PS2) SAR scenes (CSA, 2011; JAXA, 2008). A Sentinel-1 mosaic was used only for visualization in Figure 2.1b, to represent LW sea ice conditions in the broader study area. The PS2 scenes are coincident to RS2 scenes (Figure 2.1a) at NR (19.1-28.3°) and FR (35.8-42.1°) incidence angles within ±19-hour time difference, enabling comprehensive substage analysis for advanced melt. Each scene was collected in single look complex (SLC) format, except for PS2-1 which was ground range detected (GRD).

A total of 6 high-resolution, optical (VIS-NIR) images were acquired during advanced melt conditions from GeoEye-1 and WorldView-2 and -3 sensors. The optical imagery were at 2 m spatial resolution, enhanced to 0.5 m after panchromatic (pan)-sharpening. This enhancement enabled visual assessment of melting conditions, including surface flooding and drainage, determination of each advanced melt substage, and quantification of MPF.

Table 2.1: SAR and optical image characteristics.

ID	*Sensor*	*Date (yyyy.mm.dd)*	*Time (UTC)*	*Stage*	*IA range (°)*	*IA class*	*Air temp. (°C)*	*Wind speed (m/s)*
			Year 2018					
PS2-1	*ALOS-2 /PALSAR-2*	*2018.01.21*	*05:33*	*W*	*28 – 33*	*-*	*-34.7*	*6.3*
RS2-1	*RADARSAT-2*	*2018.05.20*	*14.10*	*LW*	*22.6 – 26.2*	*NR*	*-5.5*	*6.9*
RS2-2	*RADARSAT-2*	*2018.05.21*	*13.24*	*LW*	*38.7 – 41.3*	*FR*	*-5.1*	*4.4*
S1	*Sentinel 1-A*	*2018.05.28*	*23:59*	*LW*	*29.1 – 46*	*-*	*-4.1*	*6.1*
RS2-3	*RADARSAT-2*	*2018.06.10*	*23.25*	*MO*	*19.1 – 22.6*	*NR*	*0.8*	*4.7*
GE1-1	*GeoEye-1*	*2018.06.10*	*18:37*	*MO*	*16.1*	*ON*	*0.9*	*4.7*
RS2-4	*RADARSAT-2*	*2018.06.10*	*13.24*	*MO*	*35.8 – 38.6*	*FR*	*2.8*	*4.4*
WV2-1	*Worldview-2*	*2018.06.19*	*19:12*	*PO*	*2.3*	*ON*	*1.6*	*3.6*
RS2-5	*RADARSAT-2*	*2018.06.20*	*00.46*	*PO*	*36.9 – 42.1*	*FR*	*5.5*	*6.4*
PS2-2	*ALOS-2 /PALSAR-2*	*2018.06.20*	*09:34*	*PO*	*37 – 40*	*FR*	*5.2*	*8.9*
RS2-6	*RADARSAT-2*	*2018.06.20*	*14.01*	*PO*	*25 – 28.3*	*NR*	*6.6*	*8.9*
WV3-1	*Worldview-3*	*2018.06.26*	*19:12*	*PE*	*7.7*	*ON*	*8.7*	*2.5*
RS2-7	*RADARSAT-2*	*2018.06.27*	*23.49*	*PE*	*22.6 – 26*	*NR*	*3.5*	*1.4*
RS2-8	*RADARSAT-2*	*2018.06.27*	*00.28*	*PE*	*36.9 – 42.1*	*FR*	*5.4*	*4.4*
GE1-2	*GeoEye-1*	*2018.06.29*	*18:33*	*PE*	*16.2*	*ON*	*6.3*	*4.4*
PS2-3	*ALOS-2 /PALSAR-2*	*2018.07.14*	*11:14*	*PD*	*37 – 40*	*FR*	*7.8*	*8.9*
RS2-9	*RADARSAT-2*	*2018.07.14*	*23.43*	*PD*	*23.8–27*	*NR*	*3.4*	*3.3*
RS2-10	*RADARSAT-2*	*2018.07.14*	*00.12*	*PD*	*39 – 42*	*FR*	*2.5*	*5.3*
WV3-2	*Worldview-3*	*2018.07.15*	*18:45*	*PD*	*5.6*	*ON*	*17.6*	*2.8*
WV3-3	*Worldview-3*	*2018.07.15*	*19:12*	*PD*	*6.3*	*ON*	*15.7*	*6.7*

[1]IDs denote sensor type with each acquisition from a sensor numbered sequentially. Seasonal stages are described in the text. Incidence angle (IA) ranges correspond to SAR swaths, with average off-nadir angles substituted for each optical scene. IA classes are near-range (NR), far-range (FR), or off-nadir (ON) for optical scenes. ERA5 hourly air temperature (at 2m) and wind speed (at 10m) corresponding to acquisition times are provided.

2.2.4. Ancillary datasets

We collected ancillary datasets to assess the geophysical state of the sea ice and determine seasonal stages. A backscatter timeseries of FYI and MYI was extracted using the Advanced Scatterometer (ASCAT) Scatterometer Image Reconstruction (SIR) data product (Early and Long, 2001). ASCAT operates at C-band (5.3 GHz) and employs vertical polarization (VV). The SIR data product consists of 2-day composites, with a pixel spacing of 4.5 km and normalization to a far-range incidence angle of 40°. Similar time series have previously been employed for detecting MO and attributing seasonal stages based on FYI and MYI backscatter variations (Mortin et al. 2014; Casey et al., 2016; Howell et al. 2018). Additionally, daily corrected reflectance at 250m spatial resolution from the Moderate Resolution Imaging Spectroradiometer (MODIS) was used to support identifying advanced melt substages (Figure S.1).

The AEM survey comprised spatially coincident airborne laser scanner (ALS) and electromagnetic (EM) ice thickness data collected along the flight line shown in Figure 2.1a. Only the EM ice thickness data are used in this study. The EM ice thickness instrument derives height above the ice-water interface by inducing an EM field that exploits the differences of electrical conductivity between sea ice and water (Haas et al. 2009). These instruments do not allow for differentiating between snow and sea ice thickness, thus the difference between those two measurements is referred as the total thickness, i.e., snow plus ice thickness (Haas and Howell, 2015). After processing, thickness data are provided at approximately 6 m spacing along the survey track, with variations in spacing dependent on the speed of the aircraft. The AEM survey was conducted in the LW stage for retrieving the maximum sea ice thickness in the area while minimizing the atmospheric influence on surface conditions (Haas et al. 2009).

Hourly mean surface air temperature (2m) and wind speed data (10m) were derived from the 0.5 ^{o} x 0.5 ^{o} gridded, bias-corrected dataset from the fifth generation of the European Centre for Medium-Range Weather Forecasts (ECMWF) atmospheric reanalysis (ERA5). The ERA5 dataset provides a reconstruction of near-surface meteorological variables, and it is used as a meteorological forcing dataset for surface modelling. Western Arctic regional

ice analysis charts, published by the Canadian Ice Service (CIS), aided region of interest (ROI) selection. The charts are produced weekly from the integration of data from a variety of sources including surface observations, aerial, and satellite reconnaissance (Canadian Ice Service, 2011).

2.3. Methods

Figure 2.2 illustrates the main data processing and analysis workflow, elaborated upon in the following sub-sections.

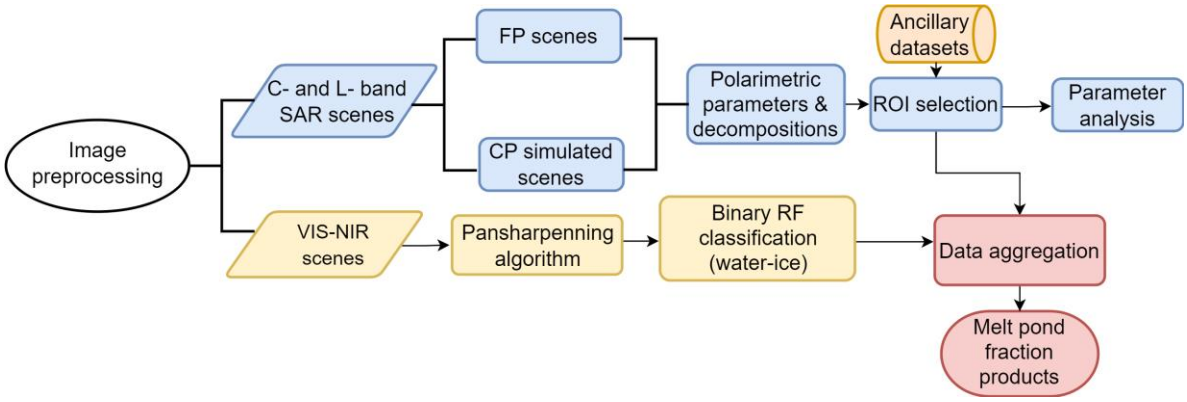

Figure 2.2: Workflow for SAR polarimetric parameter retrieval and optical scene processing to melt pond fraction. The two processing chains were executed concurrently to facilitate comparison between backscatter parameters and melt pond fraction.

2.3.1. C- and L-band SAR image processing

The SLC RS2 and PS2 scenes were calibrated to σ^0, speckle filtered using a polarimetric 7x7 Boxcar filter, and map-projected to the WGS 1984/UTM projection using Bilinear resampling. Additionally, Faraday rotation correction was applied to the SLC PS2 scenes. Following pre-processing, the RS2 and PS2 images were simulated to right circular hybrid CP mode. The SAR scenes were simulated to CP mode, due to the unavailability of CP SAR data in the region prior to the launch of RCM.

From the FP data, eight polarimetric parameters were retrieved, including polarimetric ratios. The total power (SPAN) is used to describe the backscatter variability for FYI and MYI per seasonal stage. From the simulated CP, we derived the Stokes vector components together with four child parameters describing the EM field (degree of polarization, circular polarization ratio, conformity coefficient and scattering angle α_s). Additionally, the m_χ decomposition was selected for retrieving the relative scattering mechanisms for FYI and MYI at each seasonal stage. This choice was informed by its demonstrated ability to aid identification of changes in scattering processes. This method relies on two key parameters, m (degree of polarization) and χ (Poincaré ellipticity parameter) and delivers three channels corresponding to double bounce, volumetric, and surface scattering contributions per pixel (Raney et al. 2012). Importantly, the m_χ decomposition has demonstrated its efficacy in identifying ice types across winter and summer seasons (Geldsetzer et al. 2015; Nasonova et al. 2018). This comprehensive approach yielded a total of twenty four polarimetric parameters from both RS2 and PS2 scenes, encompassing both FP and CP modes. Parameter description and definitions are listed in the Table S.1 in the supplementary materials.

2.3.2. SAR polarimetric parameter analysis

Homogeneous ROIs of FP and CP parameters from FYI and MYI were used to evaluate ice type separability, relative scattering mechanisms, relationship to MPF during advanced melt, and parameter redundancy. In addition, the effect of incidence angle range was examined based on the NR and FR designations in Table 2.1. ROIs were selected using the HH and HV channels from winter and LW RS2 and PS2 images, alongside reference ancillary data. We selected 30 FYI and 30 MYI ROIs, each measuring 20 by 20 pixels, with the deliberate intention of representing a spectrum of LW backscatter intensity levels, including varying levels of ice deformation (Figure 2.1b).

FYI and MYI sample separability was determined using the 2-sample Kolmogorov-Smirnov (KS) non-parametric test. This test measures the absolute maximum distance between the cumulative distribution functions of two samples, without assuming normally distributed data. The KS values range from 0 to 1, with 1 to indicating complete

separability. Moreover, we calculated the *p-value* for each KS test to determine statistical significance and we report only significant relationships. Before conducting the KS test for each sample, we applied z-score criteria to exclude outliers, eliminating z-score values beyond three standard deviations from the mean.

For assessing FP and CP parameter redundancy, we employed the non-parametric *Spearman's* correlation coefficient (*ρ)*. Specifically, *ρ* was calculated based on the ROIs of each ice type and substage, and within a distinct incidence angle class (NR or FR). As a correlation criterion for parameter grouping, we defined $\rho \geq |0.8|$. Beyond indicating redundancy, the correlation analysis provided insights into the grouping of parameters concerning ice type separability.

2.3.3. Melt Pond Fraction and SAR parameter comparison

High-resolution optical images from 2018 were classified to binary *ice* (or snow-covered ice) and *melt pond* pixels to: (i) retrieve areal MPF estimates for discrete regions of FYI and MYI; (ii) enhance our understanding of seasonal melt pond evolution; and (iii) assess the impact of MPF on C- and L-band backscatter. These images covered two regions in close north-south proximity and are named ROI-N, and ROI-S, respectively (Figure 2.1). Classification to MPF was done using a supervised Random Forest (RF) classifier applied to the pan-sharpened VIS-NIR bands with 0.5 m cell size obtained using the associated panchromatic band. The distinct spectral signatures of melt pond water compared to snow-covered or bare sea ice enabled overall classification accuracies >97%. Details about the image classification algorithm can be found in Scharien et al. (2014).

For analyzing MPF and SAR parameter relationships, the labelled FYI and MYI ROIs were used for aggregating SAR parameter statistics from images acquired within ± 20h of an optical scene in 2018. Additionally, a total of 30 ROIs representing pure melt pond and snow covered or bare ice over FYI and MYI types were selected from the PO stage and used to track the evolution of the pond area relative to bare ice as it subsequently evolved to become drained ice. This was done since it is expected that exposed ice that is flushed by a surface melt pond will have different physical and microwave scattering

characteristics than the surrounding ice. The MPF for FYI and MYI was then calculated for each ROI, and date-wise summary MPF statistics for individual scenes and the ice types within, were derived. Pearson's product moment correlation coefficient (r) between each polarimetric parameter and MPF was then examined to evaluate how melt ponds influence the ice type specific polarization properties of backscatter, to better understand separability potential.

2.3.4. Software usage

All the image pre- and post-processing explained in Section 2.3.1 was done using scripts integrated into the Sentinel-1 toolbox (SNAP), version 8. The polarimetric parameters analysis described in Section 2.3.2 was done using in house developed Python code utilizing Python version 3.8 (Python Software Foundation, https://www.python.org/). We performed melt pond fraction analysis stated in Section 2.3.3 using QGIS (QGIS Geographic Information System, http://www.qgis.org) version 3.28.

2.4. Results

The RS-2 and PS-2 scenes are attributed to each seasonal stage and are then examined for backscatter variability. Using SPAN and the m_χ decomposition, we describe the observed backscatter differences between FYI and MYI and identify the dominated scattering mechanisms at each stage. Coincident MPF retrievals, enable a thorough comparison with polarimetric parameters, revealing the main drivers behind FYI-MYI backscatter changes. Each section findings, support and explain the observed FYI and MYI separability and parameter redundancy.

2.4.1. Melt Season stage definition

In Figure 2.3, we present the ASCAT backscatter timeseries for each ice type. The data spans from mid-May, specifically Day of Year (DOY) 140, until DOY 200 (Figure 2.3b). MO occurs when the presence of liquid water in snow leads to a shift in MYI scattering mechanism from volumetric to surface, resulting in a large (~6dB) decrease in backscatter

(Casey et al. 2016). During this period, backscatter from FYI increases due to volumetric scattering from wet snow grains and high brine volume (Barber and Nghiem, 1999). Consequently, the backscatter timeseries of FYI and MYI converge. In our dataset, MO was detected on DOY 160. After MO, daily mean surface air temperatures are closer to 0^{o}C (Figure 2.3c), and the snowpack transitions from pendular (low saturation) to funicular regime, where liquid water is present throughout the snow and the air is trapped in distinct bubbles in the pores (Tiuri et al. 1984). The advanced melt starts when melt ponds form on the surface. At this stage, the snow cover rapidly ablates, bare ice is exposed, and MPF evolves dynamically.

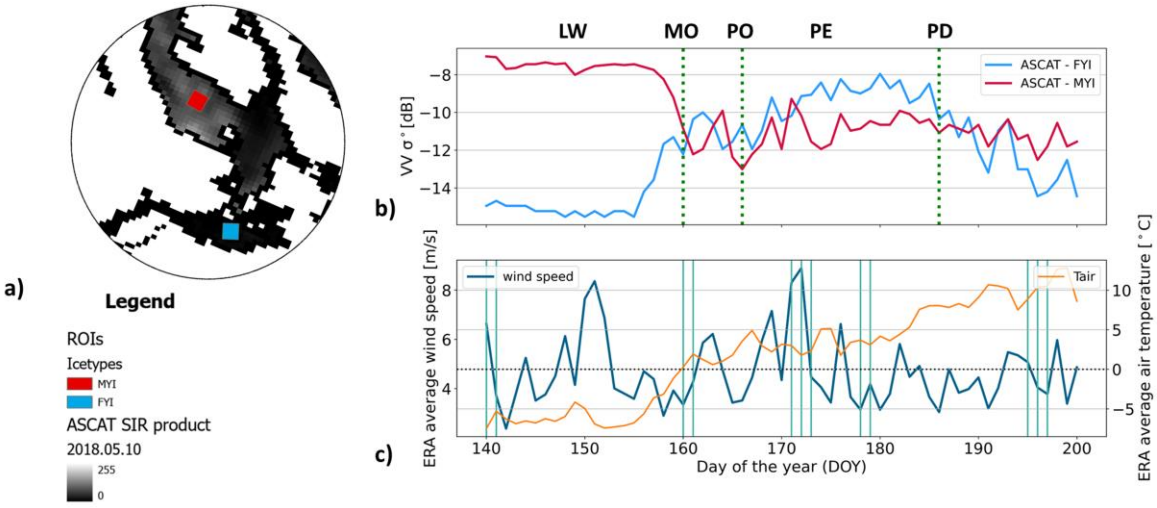

Figure 2.3: a) ASCAT data and ROIs used for FYI and MYI time series backscatter coefficient σ^0 extraction. b) Backscatter time series and seasonal regimes denoted by green dashed lines (MO, PO, PD). c) Time series ERA5 bias-corrected atmospheric reanalysis data of mean surface wind speed (at 10m) and mean surface air temperature (at 2m). Vertical, light blue lines represent the days of the RS2 and PS2 acquisitions.

To identify the advanced melt substages, we utilized optical images from high-resolution optical sensors and MODIS (see Figure S.1). The rapid and extensive flooding of relatively shallow, low-albedo ponds over smooth FYI, compared to deformed FYI and MYI, enables PO identification. Similarly, the rapid drainage of melt ponds from a FYI surface with

freeboard above the sea-level, which occurs when a permeability threshold is crossed and ice-ocean connectivity is achieved, enables PD identification. PE thus represents the intervening stage. In the study area, PO is identified at DOY 166, and PD at DOY 186. The ice in the extended area started breaking around DOY 196. MPF for the FYI samples was high during PO, then moderate in PE and decreased to low in PD, reflecting surface drainage. MYI samples had moderate MPF during PO (~50%), dropping in PE, and stabilizing at around 20% in PD. Reference surface air temperature and wind speed data are also shown in Figure 2.3c, and values coincident to SAR image acquisitions are provided in Table 2.1.

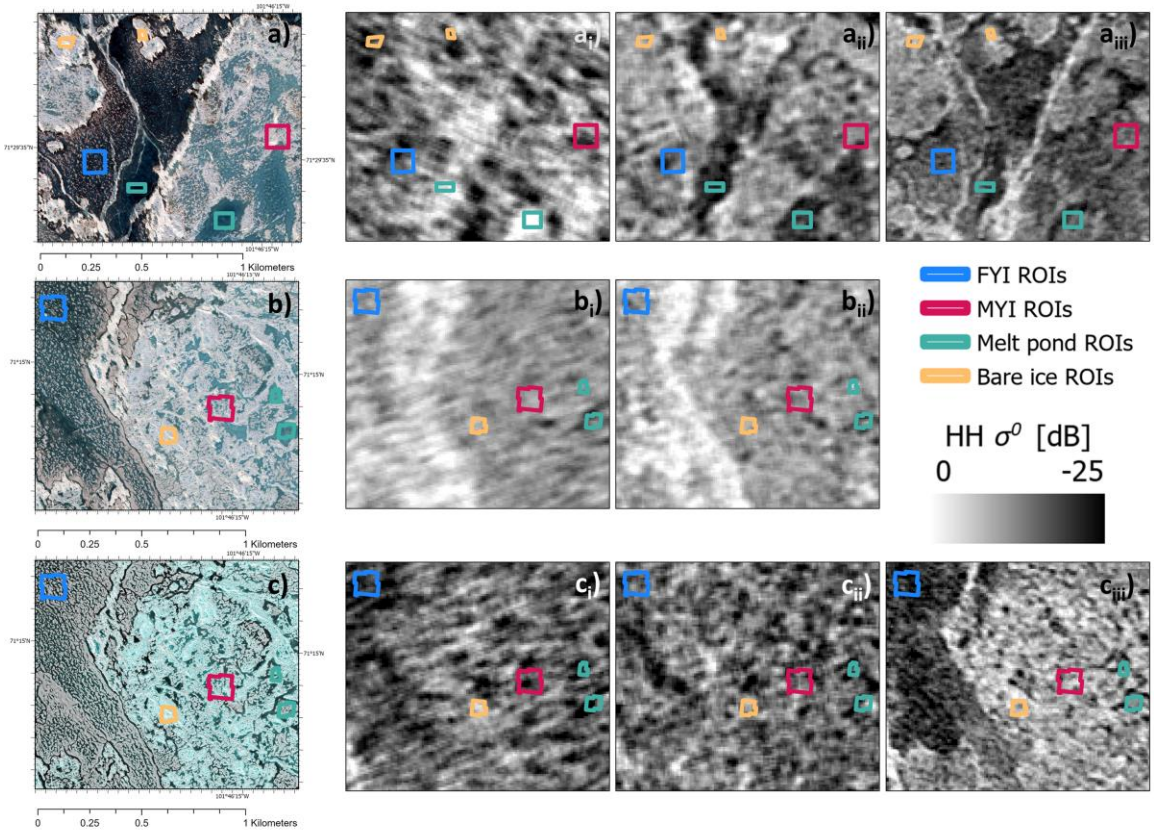

Figure 2.4: Image subsets of optical RGB composites and C- and L-band HH backscatter variability during advanced melt season substages. The top panel shows the PO stage with a) WV2-1; a_i) RS2-6; a_{ii}) RS2-5; and a_{iii}) PS2-2. The middle panel shows the PE stage with b) WV3-1; b_i) RS2-7; b_{ii}) RS2-8 (there is no L-band scene). The bottom panel shows the PD stage with c) WV3-2; c_i) RS2-9; c_{ii}) RS2-10; and c_{iii}) PS2-3.

2.4.2. FYI and MYI scattering properties across the melt season

The HH backscatter variability for SAR C- and L-band subsets in the advanced melt is shown in Figure 2.4. Additionally, Figure 2.5 presents mean SPAN for FYI and MYI, as well as initially pure pond and bare ice ROIs from PO, for all stages. Here, the same samples are examined across the season and are compared to the scattering mechanisms per type, frequency, and incidence angle. Interestingly, in each substage SPAN in NR exceeds that in FR, with the most notable difference occurring in PO. This is due to the anticipated effect of surface flooding reducing the backscatter intensity at larger incidence angles.

In LW, the C-band SAR scenes showcase the anticipated distinct contrast between FYI and MYI Progressing to MO, this contrast weakens in C-band, with FYI SPAN increasing and MYI decreasing compared to LW, aligning with the ASCAT timeseries. The relative scattering mechanisms in Figure 2.6b, show reduced volumetric scattering for MYI in both NR and FR compared to LW, indicating wet snowpack.

In the advanced melt, the C- and L- band SAR are five days after the detected PO in the MODIS timeseries, and the surface conditions are highly variable. In this stage, we notice that the SPAN of melt ponds is quite high (-4dB), similar to FYI SPAN in the NR. From Table 2.1, we observe that the C- and L-band scenes in PO, are acquired during moderate to high wind speeds affecting backscatter and SPAN. Specifically, a high wind speed (8.9 m/s) is observed for C-band in NR, and is particularly affecting the FYI backscatter, which in the NR is higher than MYI (Figure 2.4a_i). At these wind speeds a strong positive relationship is expected between C-band backscatter and MPF (Yackel and Barber, 2000). Wind roughened melt ponds result in higher Bragg scattering and SPAN for both ice types. FYI is characterized by higher MPF compared to MYI during PO, and the relatively smooth surface of FYI, compared to morphologically complex and fetch-limited MYI, promotes capillary wave development. These factors lead to a greater density of capillary waves in the SAR footprint for FYI and higher SPAN. In the FR scene from the same day, FYI SPAN is lower than MYI, and the melt pond SPAN is lower than bare ice. Despite the wind speed during this acquisition being sufficiently high to produce wind-waves (6.4 m/s), the

large reduction in SPAN is consistent with observations of C-band backscatter from wind-roughened ocean surfaces at the same wind speed and incidence angle (Snoeij et al. 1991). Thus, in the C-band and at NR, during PO, FYI SPAN is stronger than MYI due to rough surface scattering from melt ponds, whereas in FR the SPAN from FYI is weaker than MYI due to those same melt ponds. This is expected to affect the FYI-MYI separability especially in NR, allowing for greater difference between the two ice types.

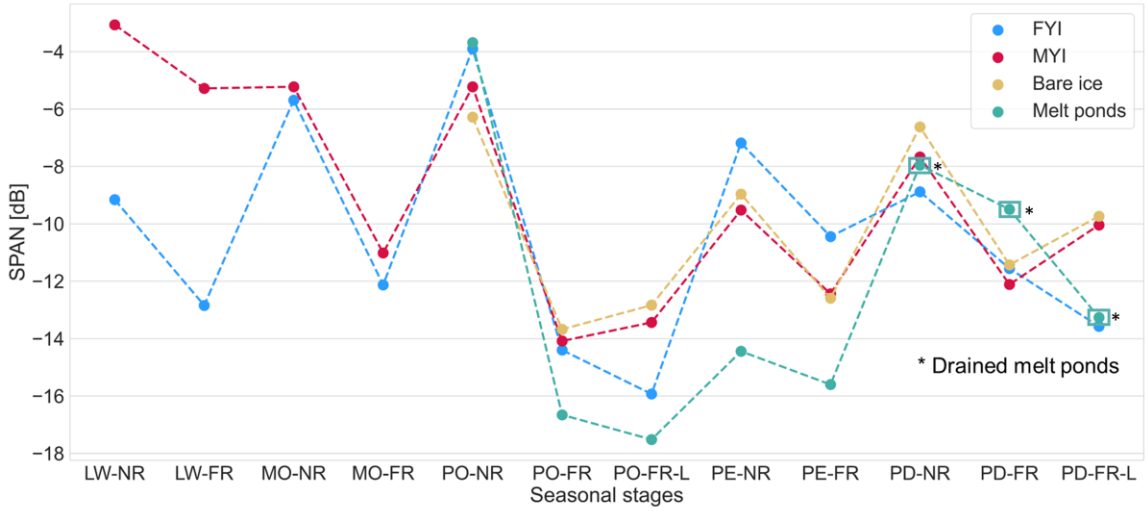

Figure 2.5: Mean total power (span) for C- and L-band ROIs in late winter (LW), melt onset (MO), pond onset (PO), pond evolution (PE), and pond drainage (PD). The analysis encompasses NR and FR for C-band during all stages, and L-band FR during PO and PD. Additional melt pond water and bare ice samples in the advanced melt (see text for description). L-band scenes are indicated by an "L" suffix.

In the L-band PO scene, greater SPAN contrast between FYI and MYI is observed than in C-band in the FR and under strong wind (8.9 m/s). Nevertheless, SPAN remains low for melt ponds and FYI, and moderate for bare ice and MYI, suggesting minimal impact from the wind. This is because L-band in FR incidence angles is less sensitive to moderate wind speeds (5 to 10 m/s) compared to C-band, thus the effect is less pronounced (Isoguchi et al. 2009). Moreover, Figure 2.4a_{iii} depicts the L-band HH backscatter. Consistent with Arkett et al. (2008) and Casey et al. (2016), we find that regions of deformed ice are clearly distinguishable, and MYI floe boundaries are better delineated suggesting good FYI-MYI separability potential at this substage.

The m_χ decomposition provides useful insights into the relative contributions of individual scattering mechanisms to total backscattered energy: surface, volumetric and double bounce. Figures 2.6c and 2.7a present the relative scattering mechanisms during PO for C- and L-band, respectively, highlighting differences between NR and FR acquisitions. The additional bare ice and melt pond samples reveal their relative roles in the observed scattering mechanisms for FYI and MYI. For C-band, NR, we observe a clear dominance of surface scattering for all ice types. In the FR, all types present a shift where the surface scattering contribution is lower (~60%) and the volumetric scattering contribution increases (~40%). FYI and MYI scattering variability indicate that both bare ice and melt ponds contribute to their signatures. However, in secondary contributions, FYI is on par with melt ponds, both showing higher volumetric scattering compared to bare ice and MYI, in NR and FR. For the L-band scene, the FYI shows similar responses to both bare ice and melt pond signatures, while MYI shows equal contributions from surface and volumetric scattering.

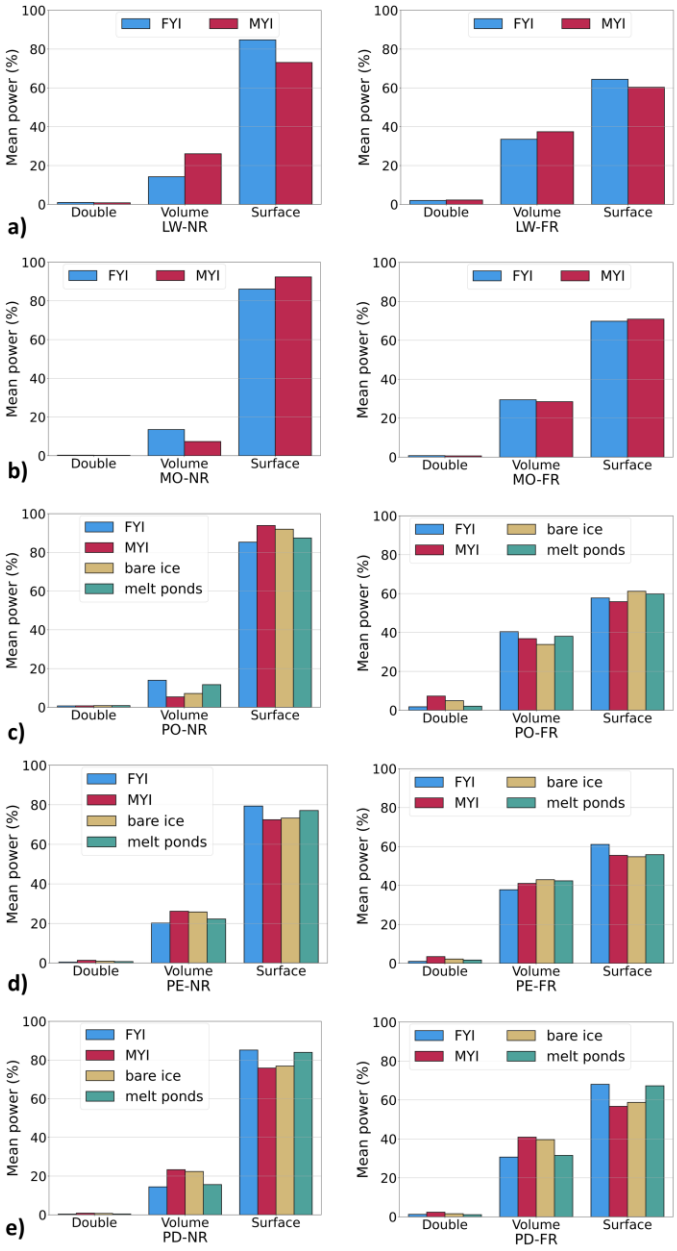

Figure 2.6: Bar plots of relative scattering mechanisms from the m_χ decomposition, from C-band acquisitions in NR (left panel) and FR (right panel). Groups a) to e) correspond to late winter (LW), melt onset (MO), pond onset (PO), pond evolution (PE), and pond drainage (PD). Bare ice and melt ponds samples are shown in addition to FYI during stages PO to PD.

During PE, nine days after PO, the C-band HH backscatter is reversed with FYI showing higher backscatter than MYI in both NR and FR (Figure 2.4b_i,b_{ii}). At this stage, FYI is about 45% drained, compared to 20% drainage over MYI. With the relatively low wind speeds of 3.1 m/s for NR and 1.9 m/s for FR acquisitions, this data suggests an ice-dominated backscatter response in place of the pond-dominated response from PO. Higher SPAN from FYI compared to MYI, in both NR and FR, is likely due to stronger relative backscatter due to surface drainage from FYI (exposure of fresh, drained ice instead of melt pond) and the presence of an absorptive wet snow surface remaining on MYI. Figure 2.6d shows dominant surface scattering for both types in NR and FR, with higher contribution for FYI.

Progressing to PD, drainage is greater for FYI (~70%), while MYI reaches a plateau at 25% (Figure 2.8a). C-band SPAN for initially melt ponds and bare ice in Figure 2.5 is similar, indicating that they both represent drained ice. FYI is considerably drained compared to earlier substages, leaving drained melt pond areas that have lower C-band SPAN than bare ice in the NR, and higher SPAN than bare ice in the FR. In the NR, the FYI SPAN is lower than MYI, while in the FR, SPAN of FYI, MYI, and bare ice are very similar. For the L-band scene in FR, there is a larger disparity in SPAN between FYI and MYI, with the latter much greater. SPAN of drained melt ponds at L-band, expected to be a greater proportion of FYI compared to MYI, is lower than bare ice.

In Figure 2.6e, the contributions from volumetric scattering for FYI and drained melt ponds present a 10% decrease compared to PE, in both NR and FR. In Figure 2.7b, the L-band FR samples present a clear dominance of volumetric scattering for all types, as well as a small contribution of double bounce. This is probably due to the greater signal penetration depth at L-band compared to C-band, combined with the relative drainage of surface melt ponds compared to the PO stage.

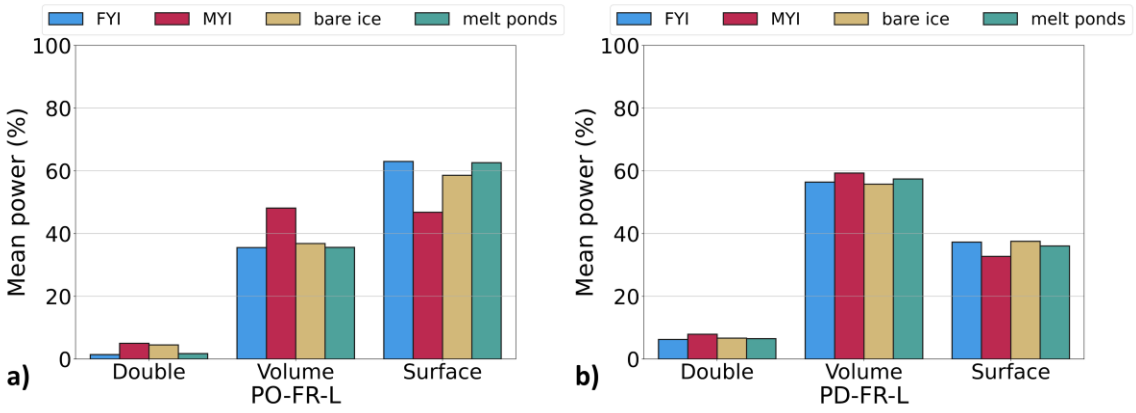

Figure 2.7: Bar plots of relative scattering mechanisms from the m_χ decomposition, from L-band acquisitions in FR during a) pond onset (PO) and b) pond drainage (PD). Bare ice and melt ponds samples are shown in addition to FYI during stages PO to PD.

Based on this stage-wise analysis, in NR, C-band surface scattering is dominant across all stages with 10% higher contribution for MYI compared to FYI in MO and PO. Volumetric scattering presented higher variability between the ice types with higher contribution for FYI (~10 to 15% more than MYI) in MO and PO. When surface drainage occurs in PE and PD, these relationships reverse for both ice types. In the FR, C-band and L-band presented a 60-40% divided contribution of surface and volumetric scattering across all stages.

2.4.3. Melt Pond Fraction retrievals

In this section, the ice type specific seasonal MPF evolution is briefly characterized. Following that, relationships between ice type specific MPF and C-band and L-band co-pol and cross-pol ratios for PO and PD stages are examined. Co- and cross-pol ratios of landfast FYI previously presented strong relationships with MPF (Scharien et al. 2012 and 2014).

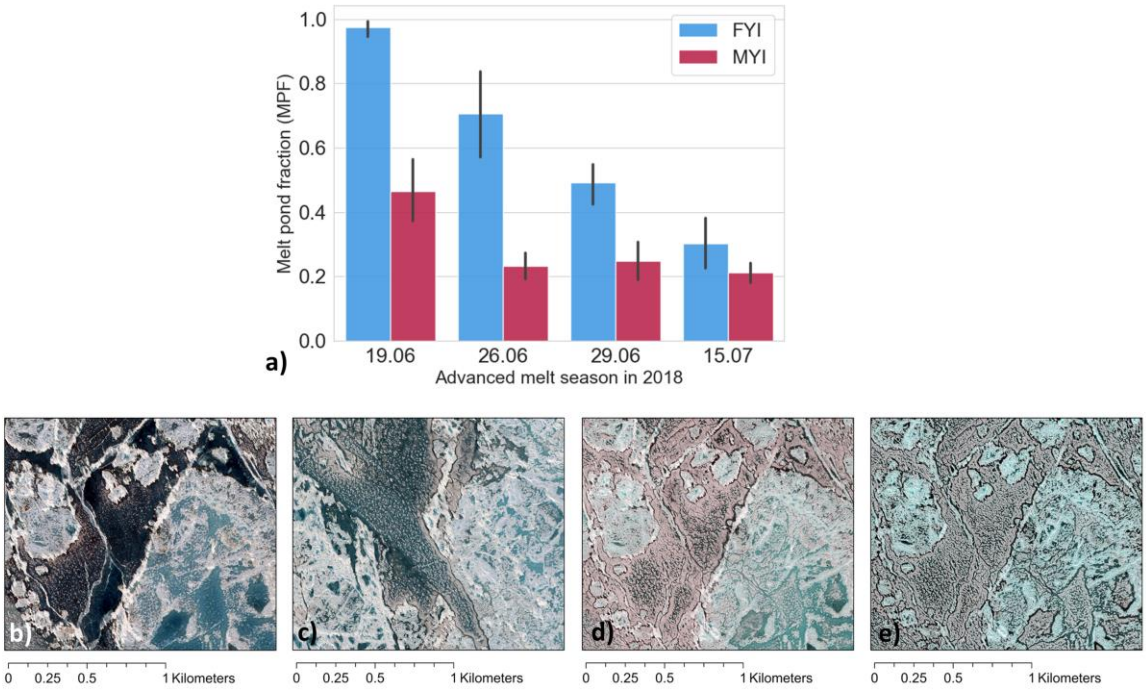

Figure 2.8: a) MPF bar plot time series of FYI and MYI, retrieved from optical imagery. The vertical lines indicate standard deviation. b) RGB colour composite image subsets demonstrating surface conditions in the corresponding dates during PO, c) and d) in PE, and e) in PD substages of the advanced melt.

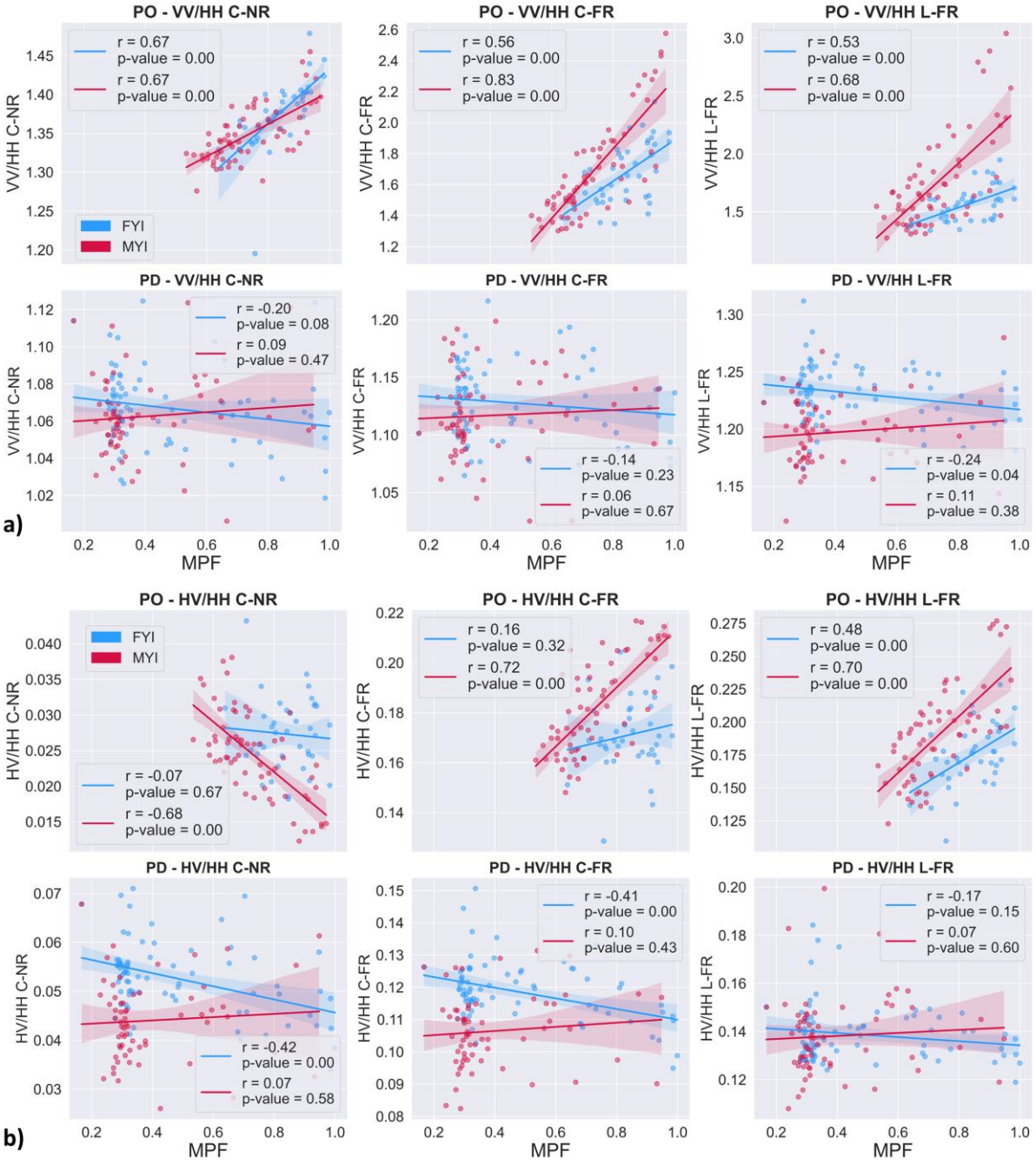

Figure 2.9: a) Scatter plots of the co-polarized ratio (VV/HH) and b) the cross-polarized (HV/HH) ratio against MPF from PO and PD substages. Pearson's product moment correlation coefficient (r) is given as a measure of linear association between the polarimetric ratio and MPF along with the significance level. The shaded area represents the size of the confidence interval for the regression estimate and here is set to 95%.

MPF was highly variable between FYI and MYI (Figure 2.8). Specifically, during PO, FYI presented higher MPF (95% ±0.05) than MYI (50% ±0.2). In PE, FYI MPF decreased to 70%, with notable variance (±0.26) on June 26th, and further reduced to 52% ±0.12 on June 29th. At the end of the season in PD, it dropped to 30% ± 0.16. Conversely, MYI MPF decreased to 23% ± 0.09 on June 26th, remained relatively similar on June 29th, and during PD on July 15th, it slightly reduced to 20% ± 0.13. It is likely that the surface conditions were highly dynamic, with MPF variability during the PE stage rapidly changing over short time intervals. In particular, this is expected for FYI, which is smooth and covered by relatively shallow melt ponds, resulting in a MPF that can rapidly change diurnally due to competing meltwater input and drainage processes.

In Figure 2.9a, the co-pol ratio shows significant positive linear relationships with MPF for both ice types and frequencies, in NR and FR in PO. In PD, these relationships are not significant expect for FYI at L-band which is slightly negative ($p < 0.05$). During PO, the strongest positive relationship with MPF (r=0.83) is observed for MYI in C-band FR. Interestingly, there are differences in the FR C- and L-band co-pol ratios between FYI and MYI across the observed MPF ranges (~1.25 to 3). We expect that melt ponds are influencing the FR co-pol ratios, as increasing liquid water in the SAR footprint, with increasing MPF, leads to more preferential backscatter of vertically compared to horizontally polarized energy. However, the separation between the FYI and MYI co-pol ratios at the FR during PO suggests that, in addition to the melt pond influence on the co-pol trend, the background ice property differences influence the polarization properties of backscattered energy at both C- and L-band as well. In the PD, the limited co-pol ratio values (~1 to 1.30) and non-significant or weak linear relationships can be explained by the dampening effect of volumetric scattering on the polarization properties of backscatter caused by the drained ice in this substage.

Relationships between the C- and L-band cross-pol ratios and MPF are shown for NR and FR scattering at C-band, and FR scattering at L-band in Figure 2.9b. During PO, we observe significant negative correlation between MYI and MPF at C-band in the NR (r=-0.68), while in the FR at both C-and L-band there are strong positive relationships for MYI (r= 0.72 and r=0.70, respectively). The negative trend for MYI in the NR can be explained

by a stronger relative increase in HH backscatter, compared to HV, due to sensitivity to increasing MPF, which in this case is associated with strong wind forcing and likely Bragg scattering during this acquisition. This effect is not seen for FYI at C-band in the NR, however. Our assumption here is that the effect of wind-wave roughening on pond surfaces is dominant over the narrow range of observed MPF on the smooth FYI surface regardless of the specific MPF. The opposite effect occurs in the FR during PO, at both C- and L-band, where the effect of melt pond wind-waves on backscatter is negligible, and HH decreases faster than HV with increasing MPF. This supports that melt ponds dominate scattering of both FYI and MYI during PO for both C- and L-band frequencies and NR and FR incidence angles. In PD, we see negative relationships for FYI at C-band (both NR and FR), while MYI presents no significant relationships. The strong cross-pol ratio associated with FYI at C-band likely indicates the emergence of volume scattering effects from the large portion of freshened ice that emerges from areas where melt ponds have drained. No significant relationships are found between MPF and the cross-pol ratio at L-band during this stage.

Overall, the results in Figure 2.9 highlight sensitivities to MPF, and potential separability, on the basis of polarization diversity at C- and L-band frequency. In terms of separability potential, it is noteworthy that L-band ratios for FYI and MYI do not overlap during PO, despite the influence of MPF.

2.4.4. C- and L-band ice type separability for FP and CP parameters

The polarimetric parameter values are calculated for each sea ice type for all scene pairs, and an equal number of samples within the 30 ROIs representing FYI and MYI are used as input to calculate the KS distance. The results are presented in Figures 2.10 and 2.11. KS separability values from LW, when high values are expected, are used as a reference for the melt season evaluation. Heatmaps for both FP and CP modes present the FYI-MYI KS values, in NR and FR for C- and L-band and have been color-coded based on three ranges: from 0 to 0.3 we define low KS, from 0.4 to 0.6 medium KS, and from 0.7 to 1 high KS separability.

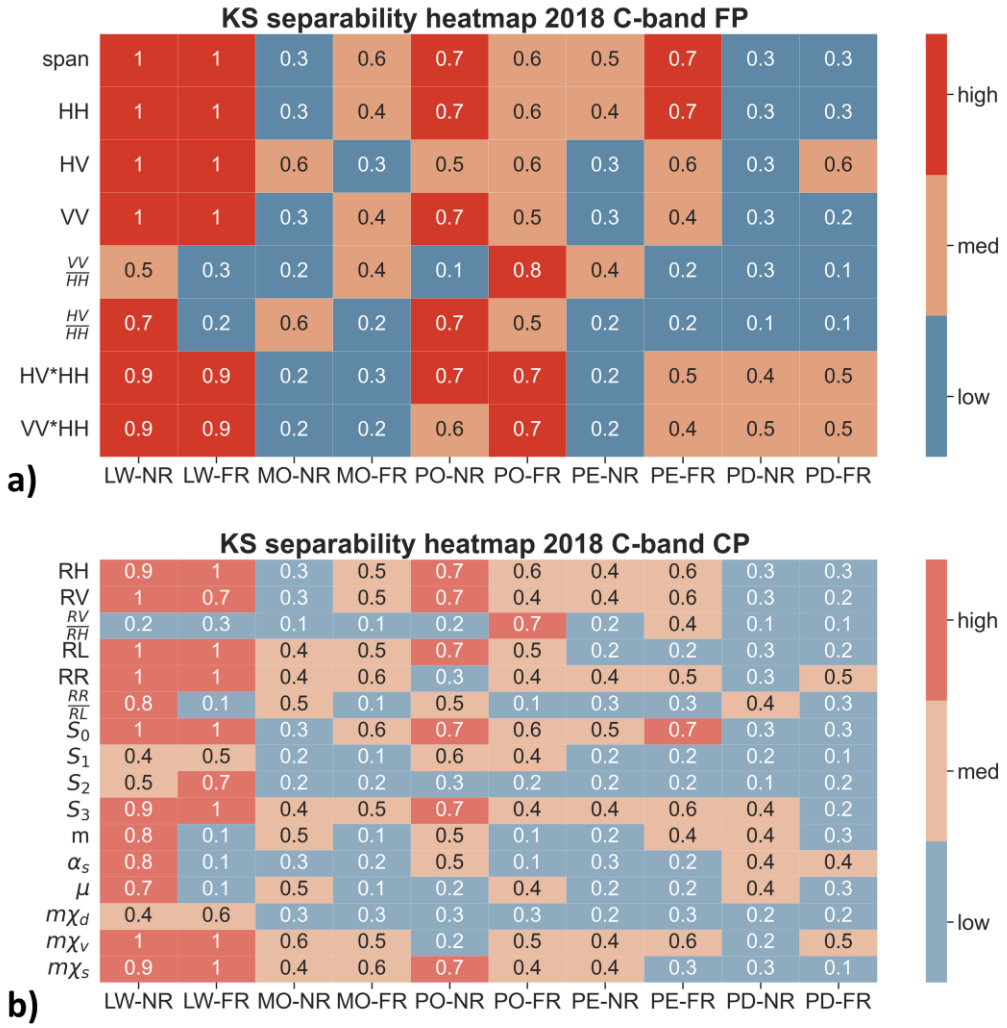

Figure 2.10: FYI and MYI type separability heatmaps using Kolmogorov-Smirnov (KS) distance for samples based on the RS2 scenes. a) C-band FP parameters. b) C-band CP parameters. Seasonal stages and NR and FR incidence angles are shown at the bottom.

In LW, we observe high separability for the majority of FP and CP parameters related to surface and volumetric scattering. However, parameters such as co- and cross-pol ratios, RV/RH, RR/RL, m, S_1 and μ show lower separability, especially in the FR, in agreement with findings from Geldsetzer et al. (2015) and Nasonova et al. (2018).

In the MO, all KS values drop as expected relative to LW, though interestingly, FP and CP parameters sensitive to volume scattering HV, and $m\chi_v$ in the NR, show good KS

separability of 0.6. This can be attributed FYI having higher volumetric scattering compared to MYI at this stage, due to brine wetted snow grains as reported by Barber and Nghiem (1999). In the FR, parameters sensitive to surface scattering such as SPAN, S_0, $m\chi_s$ and the RR parameter sensitive to volumetric scattering have good scores (KS=0.6).

Progressing to the PO substage, the KS separability is higher compared to MO, for both NR and FR. Especially in the NR, parameters sensitive to surface scattering including SPAN, HH, VV for FP and RH, RV, RL and S_0 and $m\chi_s$ in CP, denote high separability between FYI and MYI (KS = 0.7). In the FR parameters sensitive to Bragg scattering due to wind roughened melt ponds such as the co-pol ratio present the highest separability for this substage (KS = 0.8). The cross-pol ratio shows high separability in NR (KS = 0.7). These findings are supported by the SPAN and MPF analysis, confirming enhanced separability due to wind roughened melt ponds. Moreover, similar findings from Scharien et al. (2014) demonstrate the responsiveness of polarization ratios to surface melt ponds. The polarization ratios in each case, NR or FR, are sensitive to MPF and facilitate discrimination of ice types based on their MPF difference (FYI MPF > MYI MPF).

In PE, the separability between FYI and MYI in the NR is lower compared to PO. Nonetheless, in FR, high KS scores (KS = 0.7) are observed for parameters sensitive to surface scattering: SPAN and HH in FP mode, and RV, RH, S_0 and S_3 in CP mode. Highlighted in Figure 2.5, SPAN of FYI is higher than MYI, due to surface drainage, enabling a difference between the two ice types. Additionally, parameters sensitive to depolarization due to volumetric scattering (HV and $m\chi_v$) present good separability results in FR, supporting the observed increase in the volumetric scattering component at this stage (Figure 2.6d).

During PD, parameters associated to depolarization due to volumetric scattering such as HV, RR, and $m\chi_v$ in the FR, show moderately good separability. This is consistent with PE, and the observed scattering mechanism differences for FYI and MYI occurring in PD (section 2.4.2), attributed to surface drainage. However, most of the C-band FP and CP parameters present low separability at this stage.

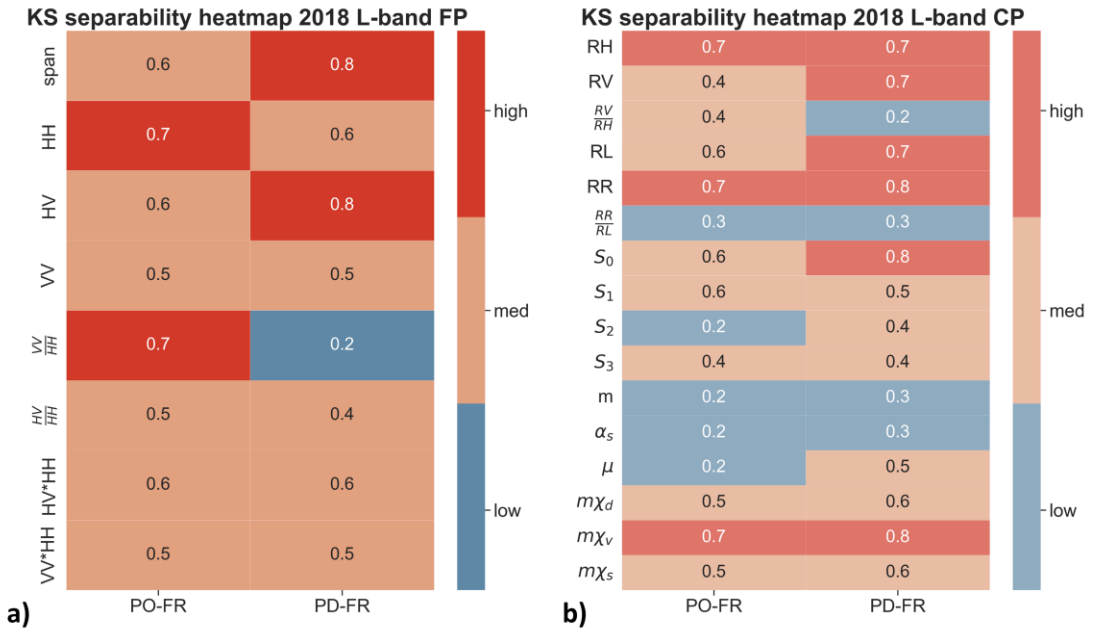

Figure 2.11: Kolmogorov-Smirnov (KS) separability heatmaps for FYI and MYI at L-band. a) L-band FP parameters. b) CP parameters. Seasonal stages and FR incidence angles are shown at the bottom.

Comparing C-band to L-band, in the PO stage, slightly lower KS scores (KS $\leq$ 0.7) are found at L-band, whereas during PD, L-band KS scores are substantially higher. During PO, separability at L-band is optimized (KS=0.7) for the FP parameter HH, and several CP parameters, including RH and $m\chi_v$. Similar to C-band FR, the co-pol ratio shows high separability supporting the MPF analysis, while in CP the parameter RR associated to volume scattering shows high separability at this stage. During PD, parameters sensitive to surface scattering (SPAN, RH and S_0) and volumetric scattering (HV, RR, and $m\chi_v$) enable very good separation (KS=0.8), reinforcing that surface drainage allows for stronger volumetric scattering contributions.

It follows from the above analysis that C-band backscatter is more sensitive than L-band backscatter to surface melt pond coverage during PO. This enables greater ice type separability based on the polarization response of backscattered energy, which is optimized by using HV/HH in NR and VV/HH in FR. On the other hand, during PD the surface is

considerably drained of melt ponds and the combined effect of enhanced volumetric scattering, and lower surface scattering, of MYI compared to FYI, from L-band backscatter leads to better separability compared to C-band.

2.4.5. FP and CP Parameter redundancy

The correlation analysis revealed consistent patterns for both ice types, with akin polarimetric parameters being correlated. Overall positive correlations are observed for surface scattering related FP and CP parameters at both C- and L-band frequencies ($\rho \geq |0.8|$) (Figures S.2 and S.3). In the FR, C- and L-band scenes presented nearly identical relationships, while more decorrelated parameters were found for FR for both FP and CP parameters across the season. The correlation relationships were weakened during PE for both FP and CP, especially for MYI. During PD, the relationships were consistent, with the same correlation ranking between NR and FR, C- and L-band for both CP and FP with scores comparable to LW.

Following Dabboor et al. (2018) and Geldsetzer et al. (2015), to minimize redundancy, the FP and CP correlated parameters can be further grouped (Table 2.2). We have identified 3 groups of parameters that presented high correlation to each other for both FYI and MYI and a group of independent. The parameters in Group 1 were found strongly positively correlated to each other. Interestingly, these parameters are sensitive to changes in surface scattering, and performed similarly in the KS separability analysis, especially during PO and PE stages, when surface scattering dominated. Group 2 parameters were positively correlated and provided higher FYI and MYI separability during MO and PD, where we observed changes in volumetric scattering. Group 3 presented variable positive and negative relationships across the season, and variable KS scores. Based on Geldsetzer et al. (2015) this group shows more promising results in the medium range of incidence angles (30 to 39^{o}). Finally, the independent group (Group 4) included the co- and cross-pol ratios, which are related to Bragg scattering and can be utilized in the cases of wind roughened melt ponds. Additionally, S_2 did not show any strong correlation ($\rho \geq |0.8|$) with other parameters across the season.

Table 2.2: Grouping of FP and CP polarimetric parameters, using Spearman's correlation coefficient ≥ |0.8| for FYI and MYI types (n = 6000). With * we denote the negative correlations

	Group 1	**Group 2**	**Group 3**	**Group4**
	SPAN	*HV*		*VV/HH*
	HH			*HV/HH*
FP	*VV*			
	*HV*HH*			
	*VV*HH*			
	RL	$m\chi_v$	*m*	S_2
	RH		S_1	*RR*
	RV		*RR/RL**	
CP	S_0		*RV/RH **	
	S_3		$m\chi_d$	
	$m\chi_s$		α_s	
			μ	

Consequently, it is possible to utilize a representative parameter from each uncorrelated group, representing different scattering mechanisms, for the purpose of classification. Nonetheless, it is important to consider the effects of incidence angle and seasonality trends in parameter relationships as our findings emphasize, to aid FP and CP data classification in the advanced melt.

2.5. Summary and Conclusions

This study provided an assessment of FP and CP polarimetric data, from C- and L-band SAR, for sea ice type separability in advanced melt conditions. We analyzed coincident RS2 and PS2 images, as well as high-resolution GeoEye-1 and Worldview optical imagery for understanding surface melt pond evolution and fractional coverage, in an area of the CAA containing a wide range of ice thickness, in 2018. Simulated CP polarimetric parameters were assessed in consideration of current, for example RCM, and future mission. In addition to statistical separability analysis, the parameter behaviours related to incidence angle, melt pond fraction and, by extension, ice fraction, were examined. Dominant scattering mechanisms for each ice type at each stage were considered using the m_χ decomposition.

For this work we addressed the following research questions: (1) Which frequency, C- or L-band, offers enhanced separability between FYI and MYI in advanced melt? (2) How do CP parameters compare to FP for FYI and MYI separability at each melt stage? (3) What is the role of melt ponds in the observed backscatter variability?

For question (1) we found the following: (i) for FP C-band, cross-polarization and cross-pol ratio in the NR, and SPAN in the FR presented consistent separability during MO, aligning with reports from Barber and Nghiem (1999) and Casey et al. (2016). An increase in volumetric scattering for FYI due to the presence of brine-wetted snow, and a decrease for MYI due to the masking effect of the wet snowpack, allows for better separability. (ii) separability during PO at C-band, when melt ponds dominate the returned signal, is best achieved using parameters sensitive to surface scattering in the NR. These include SPAN, HH, RH, RV and S_0 as well as decomposition $m\chi_s$. This agrees with Geldzetzer et al. (2015) and Nasonova et al. (2018), who found high separability for the same parameters in the NR. In the FR, VV/HH and RV/RH presented the highest separability (KS = 0.8/0.7). At L-band during PO, both surface, Bragg and volume scattering associated parameters provide separability at the FR. These include HH, VV/HH, RH, RR and $m\chi_v$. In PO, C-band performed better than L-band in terms of separability as evidence by higher KS values. (iii) separability during PE at C-band frequency is higher for FP surface scattering

related parameters SPAN and HH in FR, while in CP parameters in both incidence angles show moderate separability. (iv) separability during PD using C-band frequency is possible using FR parameters HV and $m\chi_{v,}$ though, L-band in the FR provides higher separability (KS=0.8) for surface (SPAN, RH, RV) and volumetric (HV, RR, $m\chi_{v,}$) scattering related parameters in FP and CP. The increased penetration depth from L-band into wet bare ice provides a higher contrast between FYI and MYI, due to volumetric scattering that dominates this substage. In addition, L-band data improved the identification of ice floe boundaries and deformation features (e.g., ridges) across the advanced melt season. These findings agree with previous works and strengthen our understanding when co-examining these datasets in such dynamic conditions.

For question (2), our analysis found that CP parameters were as effective as FP. The best CP parameters for both C- and L- band during the advanced melt were the first Stokes component S_0 together with the m_χ polarimetric decomposition and RR. These parameters highlighted the differences in surface and volumetric scattering between the two ice types. The $m_{\chi v}$ parameter, although not always the highest in KS separability value, ensures FYI-MYI discrimination across all advanced melt substages, depending on incidence angle utilized (here, NR or FR). Comparing to FP, at C-band HH enables separability during PO and PE substages, as HV does during MO and PD. At L-band, separability is achieved using HH during PO and HV during PD. These findings are potentially advantageous since SAR missions commonly operate in large swath ScanSAR dual-polarization HH+HV modes over sea ice, and CP data can also be collected over larger swaths. Future work should test real, not simulated, CP data and the various modes of missions such as RCM.

Another important contribution of this work comes from question (3). By examining SPAN and polarimetric ratios, together with MPF, and initially pure pond and pure ice samples, we were able to identify the influence of melt ponds on backscatter and polarimetric parameter variability. On the basis of the comparison between polarimetric ratios and MPF, we were therefore able to better understand the role of melt ponds on backscatter and ice type separability. We observed that, in the C-band frequency, NR and FR backscatter is strongly coupled to MPF during both PO and PD stages, though the effect of MPF is minimized when using the co-pol ratio in the NR and the cross-pol ratio in the FR. In the

L-band frequency, the influence of MPF is much stronger during PO than PD, when surface flooding is widespread, affecting both ice types. These results highlight the influence of melt ponds on separability and the potential utilization of these parameters as indicators for melt pond variability, an important consideration in research in atmosphere-ice-ocean exchange processes during advanced melt. In addition, we found that the cross-pol ratio in NR and FR was sensitive to differences in FYI and MYI due likely to surface roughness differences during the PD stage. On the other hand, the co-pol ratio is a consistent indicator of MPF for FYI despite environmental changes such as wind roughened melt ponds. In the PD stage, the C-band co-pol ratio does not correlate well with MPF and a general reversal in trend compared to FYI is the subject of future study.

Our findings demonstrated the utility of both C- and L-band for improved sea ice type separability retrievals in the advanced melt season. A detailed stage-wise analysis of polarimetric parameters and relative scattering mechanisms at each stage and incidence angle range, supported a deeper understanding of the surface properties and mechanisms driving FYI and MYI backscatter in the advanced melt. The comparison of FP and simulated CP parameter highlighted the potential of missions such as RCM and the parameters presented here, to be utilized from current data at different CP modes. Importantly, convectional polarimetric channels such as HH and HV presented promising FYI and MYI separability in the advanced melt, together with the co-and cross pol ratios, indicating that missions such as Sentinel-1 can be utilized for studies in the advanced melt.

For expanding this work, the FP and CP parameters proposed, should be evaluated using image classification algorithms to determine a classification scheme for the melt season. In addition, regions of drifting pack ice should be examined since there will be different melt pond and sea ice characteristics and dynamic processes compared to land fast ice conditions examined here. Similarly, more years should be examined during the advanced melt season following this analysis to enhance the robustness of this work. *In-situ* observations of relevant sea ice properties such as surface roughness, at radar and geometric scales (ridges, hummocks, etc.), as well as dielectric properties, ice properties microstructure and texture/stratigraphy, and snow properties including snow depth, snow wetness, and grain dimension, should be obtained directly coincident to SAR acquisitions.

The concurrent use of data from airborne platforms, either for the purpose of scaling from local to regional scales, or for direct SAR measurement, would be optimal. With the imaging capability of RCM, combined with pending missions such as NISAR, a new era for CP data requires expanded study of the use of CP SAR for overcoming challenges associated with highly dynamic melt season conditions, building on this, and concurrent work.

2.6. Acknowledgments

Special thanks to Malin Johansson for providing two of the ALOS-2 PALSAR-2 scenes from JAXA under the 3rd Research Announcement on Earth Observations (PI: Malin Johansson PER3A2N093). Thank you to Environment and Climate Change Canada's Climate Research Division for providing high-resolution GeoEye-1 and Worldview-2 images. We also thank Christian Haas for reviewing the paper and providing EM bird ice thickness data.

2.7. Funding

Research was funded by Marine Environmental Observations and Predictions and Response (MEOPAR) Network (1-02-02-004.5), Natural Sciences and Engineering Research Council of Canada Discovery (RGPIN-2022-05217), and Polar Knowledge Canada (POLAR) Science and Technology (NST-1718-0024) grants to Scharien. ALOS-2/PALSAR-2 scenes were provided by JAXA under the 6th ALOS Research Announcement (Project 3348; PI: Scharien).

Chapter 3. C- and L-band Synthetic Aperture Radar synergy for Arctic sea ice classification in the advanced melt season

Abstract

Sea ice type classification is crucial during advanced melt to accurately assess ice conditions, understand ice-albedo feedback mechanisms, and navigate safely through the changing Arctic. In this study, we utilized fully polarimetric C- and L-band SAR scenes from RADARSAT-2 and ALOS-2/PALSAR-2, respectively. We examined FYI, MYI, and deformed ice (DFI) types in the M'Clintock Channel of the Canadian Arctic. The study focused on two critical substages of the advanced melt, namely PO and PD, where dynamic surface conditions make ice type classification challenging. C- and L-band SAR images were classified using a random forest classification algorithm, including data from the near- (19.1º- 28.5º) and far- (35º - 42.1º) range incidence angles. The available SAR scenes per stage were compared to airborne sea ice roughness and thickness measurements acquired in the late winter for data labelling and validation. During PO, we found that C-band presented higher overall classification accuracy than L-band for all ice types, especially when combining near- and far-range incidence angle acquisitions. Conversely, L-band performance was superior to C-band during PD, with improved classification accuracies for FYI and DFI. Nonetheless, the classification accuracies in the advanced melt season were moderate, from 62 to 76% in PO and 47 to 68% in PD. In all cases, employing a dual-frequency and dual incidence angle classification approach led to more robust classification results, with 14% higher accuracies in PO and 21% in PD. Commonly available bands, HV and VV and the cross-pol ratio presented the highest information content for the classification algorithm. These findings highlight the value of existing constellation missions and upcoming dual-frequency and L-band SAR missions, as they offer great potential for improved summer sea ice retrievals.

Keywords: SAR, sea ice classification, Random forest, advanced melt, deformed ice, dual-frequency

3.1. Introduction

The declining sea ice extent and thickness and earlier and longer melt have far-reaching consequences for the Arctic environment. Thinner ice exhibits reduced internal strength, leading to increased ice deformation (Itkin et al., 2017; Landrum and Holland, 2020). Ice deformation, encompassing features such as lead edges, rubble fields, and pressure ridges, directly influences snow accumulation and heat fluxes through the ice, affecting winter sea ice growth. It also affects surface and bottom ice roughness, impacting the momentum transfer between the atmosphere and ocean, promoting lateral melt, and accelerating ice drift speed (Cole et al., 2017; Graham et al., 2019). Furthermore, prolonged melt seasons increase solar radiation absorption on the ice surface, intensifying ice melt and disrupting climate feedback mechanisms (Grenfell et al., 1998; Perovich et al., 2007). In the advanced melt, the widespread distribution of melt ponds on sea ice alters surface roughness and ice mass balance while tripling the amount of the photosynthetically active radiation available to primary producers (Nicolaus et al., 2012), exerting a substantial influence on the Arctic ecosystem.

Beyond environmental shifts, longer melt seasons and increased ice deformation have implications for Arctic marine activities and transportation. While the receding ice increases accessibility in the Arctic, it also raises concerns about potential maritime hazards (Pizzolato et al., 2014; Eicken and Mahoney, 2015). Specifically, thick MYI and regions with deformed ice (DFI) are hazardous to transiting vessels and offshore structures. This is of particular concern for navigation in the CAA through the Northwest passage that connects the Beaufort Sea in the west with Baffin Bay in the east (Smith and Stephenson, 2013). In the CAA, ice that is older and consequently thicker -often exceeding 10 m- is found within level undeformed areas and can flow into the Arctic Ocean via the connecting straits (Barber et al., 2014). Hence, ice type identification and classification during the melt season is essential for the Arctic climate and ecosystem, navigation, and hazard mitigation. Additionally, climate model predictions require improved observations on ice dynamics of the seasonal sea ice zone (Dierking and Dall, 2007; Toyota et al., 2021)

SAR is an important data source for providing valuable all-weather, high spatial resolution image data with multi-polarization and multi-frequency capabilities, suitable for monitoring dynamic and thermodynamic changes of sea ice at metre-scale resolution (Moreira et al., 2013). As well, operational ice services worldwide use large volumes of SAR data to produce sea ice stage of development and ice concentration charts on a regular basis (Canadian Ice Service, 2011). The sensitivity of SAR signals to factors like surface roughness (particularly when it's similar in size to the signal's wavelength), variations in local angles, and inconsistencies in ice such as cracks and air bubbles, can impact the accuracy of radar measurements. Seasonal changes in ice and snow's dielectric properties also influence the radar measurements. (Dierking and Dall, 2007).

In the melt season, there are limitations, particularly in distinguishing between FYI, DFI, and MYI, presenting challenges to operational services (Haas and Howell, 2015). For winter season monitoring, the higher C-band SAR frequency is favored because of its ability to differentiate between surface scattering from FYI and volumetric scattering from MYI (Barber et al. 1999). As surface temperature increases, saturated snowpack and liquid water on the upper ice layer reduce signal penetration, obscuring the detailed scattering from MYI (Onstott, 1992). Lower SAR frequencies have higher signal penetration capacity, which increases sensitivity to volumetric scattering from thicker ice types and multiple scattering from deformation features (Onstott et al, 1987). Hence L-band SAR has emerged as particularly advantageous in distinguishing sea ice types and deformation features during the early and late melt season stages (Dierking and Dall, 2007; Casey et al., 2016; Cafarella et al., 2019; Tavri et al., 2023). Additionally, SAR polarimetric parameters can enhance information about sea ice types and surface roughness, supporting ice type mapping in the melt season. Casey et al. (2016) and Tavri et al. (2023), using dual and fully polarimetric data respectively, found that combining C-band and L-band data in the advanced melt leads to better separability of FYI and MYI. The upcoming L-band SAR missions (NISAR and ROSE-L) and the existing fully and compact polarimetric missions (RADARSAT-2, ALOS-2/PALSAR-2, RADARSAT Constellation Mission) have significant potential for integrating C- and L- frequencies to monitor and classify sea ice types under the new Arctic regime.

During the advanced melt season, air temperatures consistently surpass 0^{o}C, leading to isothermal wet snowpack and melt pond formation on ice, hiding backscatter difference between ice types (Livingstone et al., 1987a; Comiso and Kwok, 1996; Barber and Yackel, 1999). Complex data-driven methods need large datasets that are harder to acquire in the advanced melt season. Many studies use polarimetric features or decompositions with focus on C-band or L-band SAR classification schemes to exploit the additional information content in the polarimetric data. In a recent study, Singha et al. (2020) investigated L-band fully polarimetric data in the advanced melt, examining different incidence angles, including deformed ice types. Their findings underscored the superior ability of L-band data in differentiating smooth FYI from deformed ice, particularly at moderate incidence angles ranging from 30° to 37°.

Sea ice classification algorithms typically encompass support vector machines and neural networks (Nasonova et al., 2018; Singha et al., 2020; He et al., 2022). He et al., 2022 used C-band fully polarimetric SAR decompositions for sea ice classification in the advanced melt, elaborating a Random Forest (RF) classifier. RF classifiers can handle large and complex high-dimensional datasets; thus, it is often used for remote sensing problems (Belgiu and Dr˘agu, 2016). Nevertheless, a methodology integrating C- and L-band SAR signatures via data-driven classification techniques has not yet been proposed for sea ice classification in the advanced melt. The integration of these frequencies in the advanced melt regime holds significant promise for enhancing the retrievals of ice types and deformation, as well as gaining insights into the variations in ice type roughness during different sub-stages of the melt season. This approach also presents an exciting prospect, especially considering the imminent launch of new missions equipped with C- and L-band SAR, which will provide access to additional polarimetric modes, including compact polarimetric data.

This work focuses on sea ice type classification during the advanced melt season using C-band and L-band SAR. Overlapping SAR scenes during the critical stages of PO and PD are evaluated using auxiliary optical and in-situ datasets. Airborne sea ice roughness data are used for validation purposes and for the identification of deformed ice. An RF classification scheme is employed to access ice type classification over landfast ice in

CAA. Our primary objective is to assess the performance of each SAR frequency in classifying FYI, MYI, and DFI during each melt substage using multiple SAR parameters. Moreover, we evaluate the effect of incidence angle on ice type backscatter and classification performance, comparing results from near (22.6^o – 28.3^o) and far (36.9^o – 42.1^o) range acquisitions and their combination. The paper is organized as follows: Section 3.2 details the study site, C- and L-band SAR datasets, and ancillary datasets. The classification scheme and methodology are described in Section 3.3, followed by the results and discussion in Section 3.4. Conclusions and further recommendations are outlined in Section 3.5.

3.2. **Study area and data**

The study area was in the M'Clintock Channel in the western CAA (Figure 3.1a). Based on daily charts from the Canadian Ice Service Digital Archive (CISDA), thick FYI and old ice dominated the M'Clintock Channel in 2018 (Figure 3.1a). Data from an airborne survey acquired during Late Winter (LW) provided detailed information about sea ice roughness and thickness (Figure 3.1b). The overlapping SAR scenes capture varying roughness and thickness conditions (thickness ranging from 1.7 to 11 m), including ice types of thermodynamically grown FYI and MYI, and DFI. The sea ice is landfast so that the same floes could be tracked throughout advanced melt, making this region ideal for establishing seasonal linkages with SAR backscatter and testing sea ice classification methods.

Two sets of overlapping C- and L-band SAR scenes are analyzed, together with two available C-band SAR scenes in the LW, when the ice conditions were consistent and comparable to those observed while acquiring the airborne sea ice roughness and thickness datasets. Specifically, we examined two distinct phenological stages in the advanced melt period: PO and PD. PO is characterized by the formation of melt ponds and an increase in their coverage, altering the ice surface properties. During this substage, surface roughness is decreased, and the ability to distinguish between FYI and MYI types is minimized. However, DFI types are identifiable in the advanced melt season using lower SAR frequencies (Casey et al., 2016). Conversely, in PD, the drainage of these melt ponds and a subsequent decrease in their coverage facilitates more effective separation of ice types.

For comprehensive descriptions and definitions of these substages, readers can refer to previous works by Eicken et al. (2004), Scharien et al. (2012), and Tavri et al. (2023).

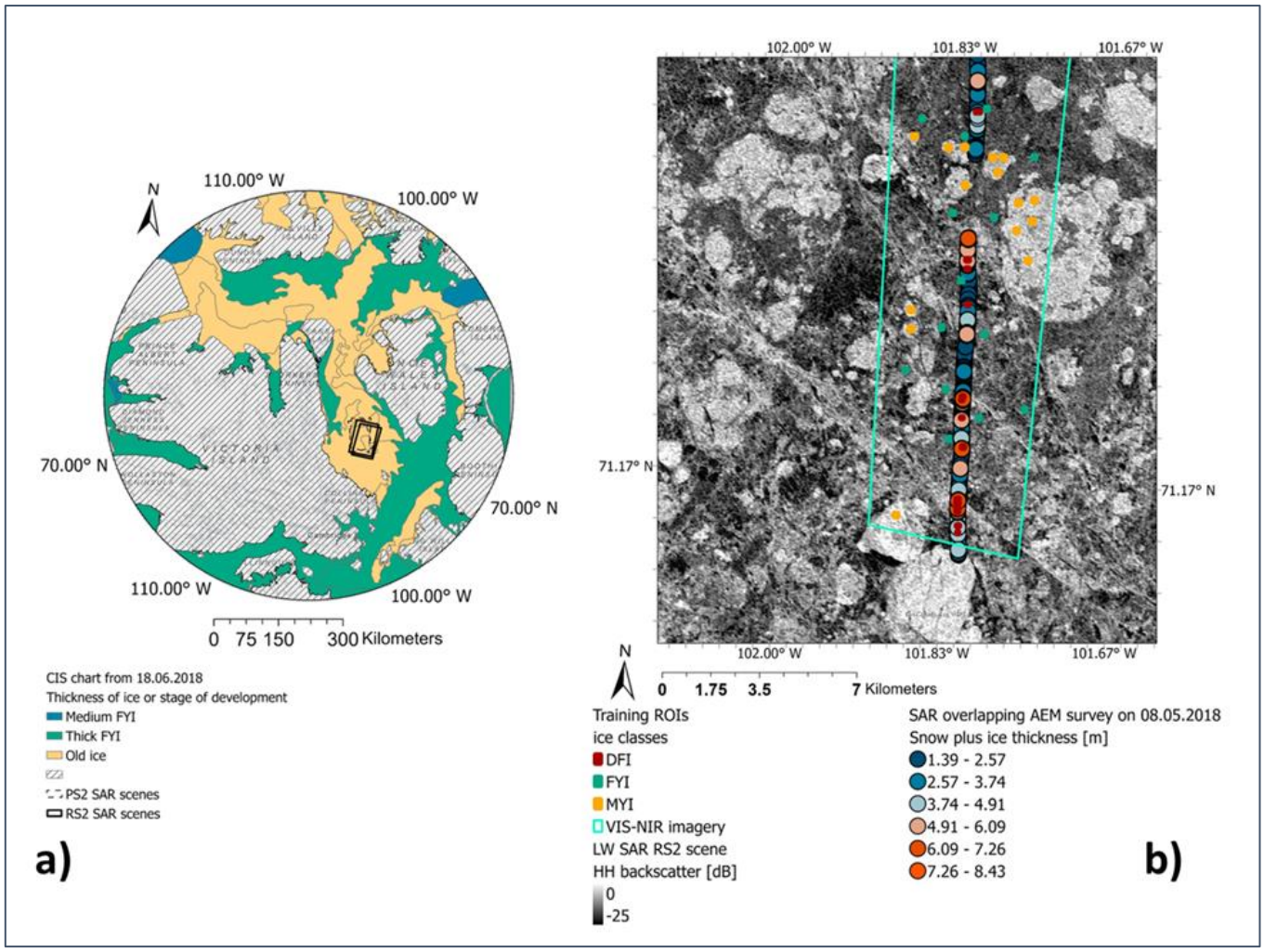

Figure 3.1: The study area in the McClintock channel, in the western Canadian Arctic Archipelago. a) Canadian Ice Service (CIS) chart presenting the sea ice types in the extended area with dashed-line and line rectangles denoting the areal extents of the ALOS-2 PALSAR-2 and RASARSAT-2 SAR scenes. b) a zoomed-in depiction of the study area, using an RS-2 SAR background to present the late winter sea ice conditions. The survey track from an airborne electromagnetic survey conducted in 2018 is overlaid.

3.2.1. Full polarimetric C- and L-band SAR

The dataset includes 6 C-band (5.4 GHz) RADARSAT-2 (RS2) and 2 L-band (1.27 GHz) ALOS-2/PALSAR-2 (PS2) SAR scenes (CSA, 2011; JAXA, 2008) (Table 3.1). All SAR scenes are fully polarimetric and in SLC format. The LW RS2 scenes provide the baseline pre-melt backscatter and polarimetric signatures used to identify ice types accurately. The PS2 scenes were acquired within a ±19-hour time difference from RS2 along with spatially coincident NR (22.6^{o} to 28.3^{o}) and FR (36.9^{o} to 42.1^{o}) RS2 image pairs.

3.2.2. **Auxiliary datasets**

A total of 3 high-resolution, optical (VIS-NIR) images from WorldView-2 and -3 sensors overlapping with the SAR scenes were used to aid the analysis. The scenes cover PO, PE and PD substages. The spatial resolution of each scene was enhanced from 2 m to 0.5 m after panchromatic (pan)-sharpening, allowing for visual assessment of melting conditions, including surface flooding and drainage, and determination of each advanced melt substage.

The airborne sea ice thickness and surface roughness data were collected on May 8, 2018, to measure maximum snow plus sea ice thickness, minimizing surface variability due to atmospheric processes like erosion and snow redistribution. An AEM thickness sounding instrument induced an EM field in the conductive sea water under the resistive sea ice, allowing the calculation of the instrument height above the ice/water interface (Haas and Howell, 2015). A laser altimeter within the EM instrument measured the height above the snow cover. The difference between these measurements represented the total thickness, referred to as ice thickness, as it is impossible to distinguish between snow and ice thickness due to their similar resistivity (Haas et al., 2009; Haas and Howell, 2015). This method oversampled the ice because each EM measurement covered a footprint about 3 to 4 times the instrument's height above the ice, equivalent to up to 120 meters, with typical instrument heights below 30 meters. With a sampling rate of 10 scans per minute, thickness observations were obtained approximately every 6 meters. In addition, a Riegel Laser Measurements Systems (Riegel LMS) Q120 near-infrared laser scanner was used to collect 2D swaths of relative surface elevation data. Each scan line was approximated using a flat

surface hyperbolic equation. Surface roughness was calculated as the standard deviation of the difference between measured and fitted surfaces for each scan line (Beckers et al., 2015). The resulting surface roughness corresponds to the root-mean-square (s_{rms}) over an approximately 105 m wide swath perpendicular to the flight direction. The scanner operated at 50 lines per second, resulting in surface roughness measurements spaced approximately 1.2 meters apart. Surface roughness is frequently characterized using the s_{rms}, which is one of the most widely employed parameters for this purpose. Details of the SAR and auxiliary datasets are provided in Table 3.1.

Table 3.1: Data description and characteristics.

Parameter	Sensor	Platform	Date (yyyy.mm.dd)	Season	Description
Snow and ice thickness	EM Bird – Electromagnetic induction and laser altimeter	Airborne	2018.05.08	LW	Spatial resolution: 6.0 m Swath width: ~120 m Accuracy: 0.15 m
Sea ice surface roughness	Riegel Laser measurement System Q120-2D laser scanner	Airborne	2018.05.08	LW	Spatial resolution: 1.2 m Swath width: ~105 m Accuracy: 0.025 m
Radar backscatter	RADARSAT-2 – C-band SAR ALOS-2/PALSAR-2 – L-band SAR	Satellite	2018.05.20 (RS2) 2018.06.20 (RS2 & PS2) 2018.07.14 (RS2 & PS2)	LW PO PD	Pixel spacing: 9.8 x 9.8m Incidence angles: Near range (NR): 22.6 – 28.3 Far range (FR): 36.9 – 42.1º Mode: Fine Quad pol NESZ: -33.5 dB for RS2, -25 dB for PS2
Sea ice optical properties and stage definition	Worldview-2 and -3 – Multispectral (VIS-NIR)	Satellite	2018.06.20 2018.06.26 2018.07.15	PO PE PD	Pixel spacing: 2.0 m Incidence angles: off-nadir 5.6 – 7.7º

3.3. **Methodology**

For sea ice type classification, we examined three scenarios based on the unique characteristics of the dataset:

- Scenario I involved the individual analysis of parameters per frequency and incidence angle,
- Scenario II examined the combination of parameters in both incidence angle ranges,
- Scenario III examined the combination of both frequencies and incidence angle ranges.

Details on the selected parameters and their definition can be found in Table 3.2.

Table 3.2*:* An overview of the investigated SAR polarimetric parameters in this study.

Polarimetric parameters	Description	Equation	Units
HH, HV, VV	Sigma naught (σ^0) backscatter intensity	$\mathbf{S} = \begin{bmatrix} S_{HH} & S_{HV} \\ S_{VH} & S_{VV} \end{bmatrix}$	Power
VV/HH	Co-polarization ratio	$\sigma^0_{VV/HH}$	Unitless
HV/HH	Cross-polarization ratio	$\sigma^0_{HV/HH}$	Unitless

3.3.1. SAR image processing and class selection

The RS2 and PS2 SAR scenes were calibrated to sigma naught (σ^o), speckle filtered using a polarimetric 7x7 Boxcar filter, and map-projected to the WGS 1984/UTM projection using Bilinear resampling to 12m pixel spacing. Subsequently, the primary polarization channels (HH, HV, VV) were selected, as well as the co- and cross-polarization ratios (VV/HH, HV/HH), informed by the work of Tavri et al., 2023, which demonstrated their effectiveness in distinguishing between FYI and MYI types in the advanced melt. Consequently, examining these parameters holds considerable utility for classification purposes. We carefully chose a set of Regions of Interest (ROIs) representing each ice type for model training and validation. For the selection and labeling of FYI and MYI ROIs, we used the LW C-band SAR scenes, ice chart polygons, and the available high-resolution optical scenes. FYI and MYI ROIs comprised 15 polygons representing FYI and MYI, each measuring 20 x 20 pixels. DFI ROIs were identified using the ice roughness (s_{rms}) point track.

The airborne measurements of s_{rms} were used to identify DFI regions using a fixed threshold to separate the point measurements into deformed and undeformed ice types based on Casey et al. (2014). Accordingly, a cut-off value of two standard deviations above the mean (τ_{rms} = 0.35 m) of the s_{rms} was applied to classify the track into deformed (rough) and level ice classes. Thus, the airborne s_{rms} points were separated into two classes, DFI and non-DFI. We resampled the track using an 8-point average to match the SAR image resolution and labelled the selected points as DFI as training input to the classification algorithm together with the FYI and MYI polygons. Furthermore, we manually labeled the ice thickness track to support image analysis and ROI selection. We linked sea ice thickness measurements to FYI and MYI classes using the optical images and backscatter signals from the LW scenes. Then, we identified deformed points on the thickness track using the detected deformed areas in the labeled roughness track.

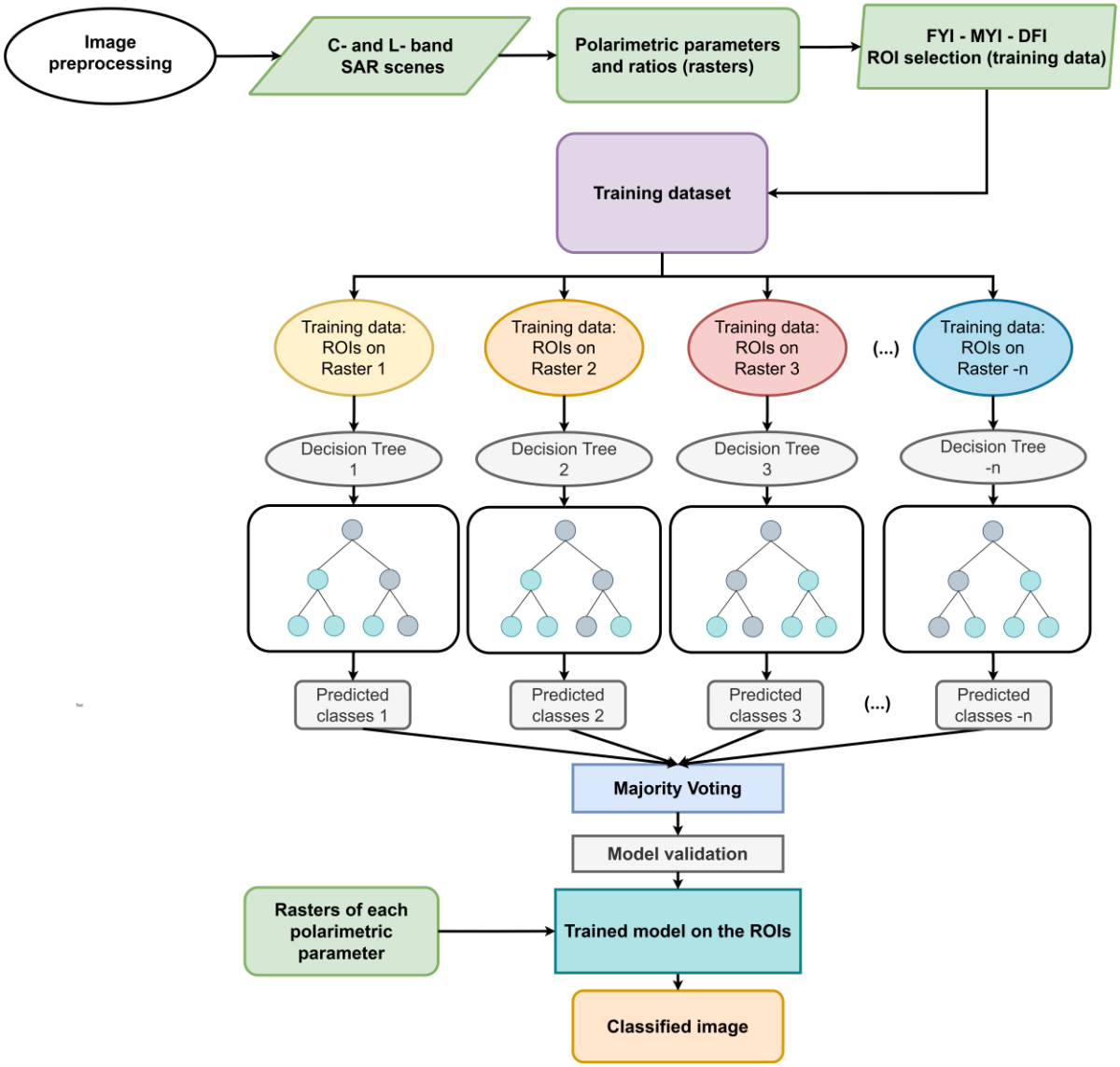

Figure 3.2: Methodological workflow for the SAR image classification using a Random Forest machine learning algorithm. ROIs representing zones of homogeneous sea ice types are used for training the classification model that classifies each SAR image.

3.3.2. Image classification and validation

An RF classification algorithm is implemented for evaluating each classification scenario (Breiman, 2001). It uses many individual decision trees as an estimator, each generated from a randomly selected subset of the training dataset and a randomly selected subset of features or inputs. Each tree is associated with a decision and gives an individual class label. The final class is then decided by a majority voting from all trees in the forest (Figure 3.2), avoiding overfitting the model to the training dataset. Lohse et al., 2020 demonstrated the utility of decision-tree and RF algorithms for sea ice classification in the winter since the algorithm allows for extracting patterns or rules in a dataset, compared to other methods. This is particularly important for implementing such an algorithm in the advanced melt season, utilizing the information and patterns of each ice type signature from the SAR parameters. The implemented RF algorithm evaluates several parameters simultaneously, informing each class prediction. Initially, we build the training models based on the FYI, MYI and DFI ROIs. We divided the total of training samples to 80% used for the training model, and we created decision trees that predict each of the three classes using the five SAR parameters (Table 3.2) as explanatory variables. The remaining 20% of the training samples were used to validate the model. We employed a consistent configuration of 300 decision trees to parameterize the models at each seasonal substage and avoid overfitting, and each training model was executed for 100 iterations. Based on the highest overall classification accuracy, the best-performing model was selected to classify the complete SAR image utilizing all explanatory variables (HH, HV, VV, HV/HH, VV/HH).

Based on the pre-defined scenarios I to III, we created training models per substage (PO and PD) and created substage-based classifications. Subsequently, we calculated the confusion matrix for assessing the classifier's performance, including User's and Producer's accuracies (Congalton, 1991). Additionally, the out of bag error was calculated, to estimate the accuracy of the RF model for each scenario for internal data validation and RF model optimization. Specifically, the mean squared error (MSE) is reported to assess the overall proportion of incorrect out of bag classifications for each ice type. The importance of each explanatory variable for the training model is also reported using Gini coefficients that indicate the number of times an explanatory variable is responsible for

individual decisions in each decision tree, divided by the number of trees (Loh and Shih, 1997). The variable importance metric refers to the frequency with which a variable contributes to a split in a decision tree and the magnitude of its impact on those splits, normalized by the total number of trees in the ensemble. Splits in this context correspond to individual decisions within the decision tree structure and informs the predictive model to be more precise and interpretable, including statistically significant variables (Menze et al., 2009).

Furthermore, the classification results for the DFI class were validated against the DFI data from the AEM track using zonal spatial statistics. The overlapping SAR and track points were extracted, and we created a profile plot including all the examined scenarios to evaluate the classification performances. We utilized an image segmentation algorithm to create a set of internally coherent, externally contrasting image objects representing homogeneous FYI and MYI zones and boundaries in the study region to aid the visual inspection of the classification outputs. The segmentation was created using the bottom–up, region-merging technique detailed in Benz et al. (2004), applied to an 8-bit scaled RS2 HH band from LW, following Scharien et al. (2017).

All the image pre- and post-processing was done using Sentinel-1 toolbox (SNAP), version 8. Python code was used for the classification algorithm utilizing Python version 3.8 (Python Software Foundation, https://www.python.org/). The segmentation algorithm is incorporated in Geomatica, 2017 (https://catalyst.earth/).

3.4. **Results and Discussion**

In this section, we examine the airborne ice thickness and roughness measurements obtained in LW to gain insights into the ice conditions within the study region. We used a predefined threshold derived from the s_{rms} data distribution to classify the airborne datasets into two categories: DFI and non-DFI. Corresponding labels for ice thickness were also established to facilitate comparison. Subsequently, we detail the variability in ROI HH backscatter and delve into the FYI, DFI, and MYI classification outputs for all scenarios and seasonal stages. Furthermore, we present a comparative analysis between the

overlapping C- and L-band backscatter data with the DFI identification derived from in situ s_{rms} measurements. This comparative examination is conducted to elucidate the distinctive DFI signatures in PO versus PD for both C-band and L-band SAR. To support this analysis, the relative scattering mechanisms of each ice type are examined across the season using the Freeman Durden decomposition (Freeman and Durden, 1998).

3.4.1. Airborne ice-type roughness and thickness in LW at M'Clintock Channel

Figure 3.3a illustrates the distributions of the airborne sea ice roughness and thickness survey by type. The mean surface roughness value of the points of the AEM track that overlapped with the SAR scenes was 0.15 m, with a standard deviation of 0.1 m. For non-DFI, the surface roughness varies between 0.05 and 0.35 m, with a mean value of 0.13 m and a mode of 0.06 m, indicating that the data is skewed. In contrast, DFI exhibits a mean surface roughness of 0.45 m and a mode of 0.46 m, indicating a uniform distribution for the deformed features. Upon evaluating ice thickness distributions, the total overlapping AEM track had a mean thickness of 3.17 m with a standard deviation of 1.37 m. DFI types are notably marked by values spanning from 1.3 to 11 m, with a mean of 5.26 and a mode of 4.96 m. In contrast, non-DFI types display an average thickness of 3 m and a mode of 2 m agreeing with observations from Melling (2022). Figure 3.3b further shows the relationships between sea ice roughness and thickness.

A positive correlation between ice roughness and thickness is evident for non-DFI types, with Spearman's correlation coefficient (ρ) 0.5. A weaker positive correlation is observed for DFI types (Figure 3.3b). These statistical findings illustrate the dynamic nature of ice conditions within M'Clintock Channel. The predominant composition of the study area consists of smoother ice with moderate thickness. In contrast, the deformed ice,

characterized by significantly higher roughness, exhibits a broader range of thickness values, indicating that deformation does not necessarily correlate with greater ice thickness.

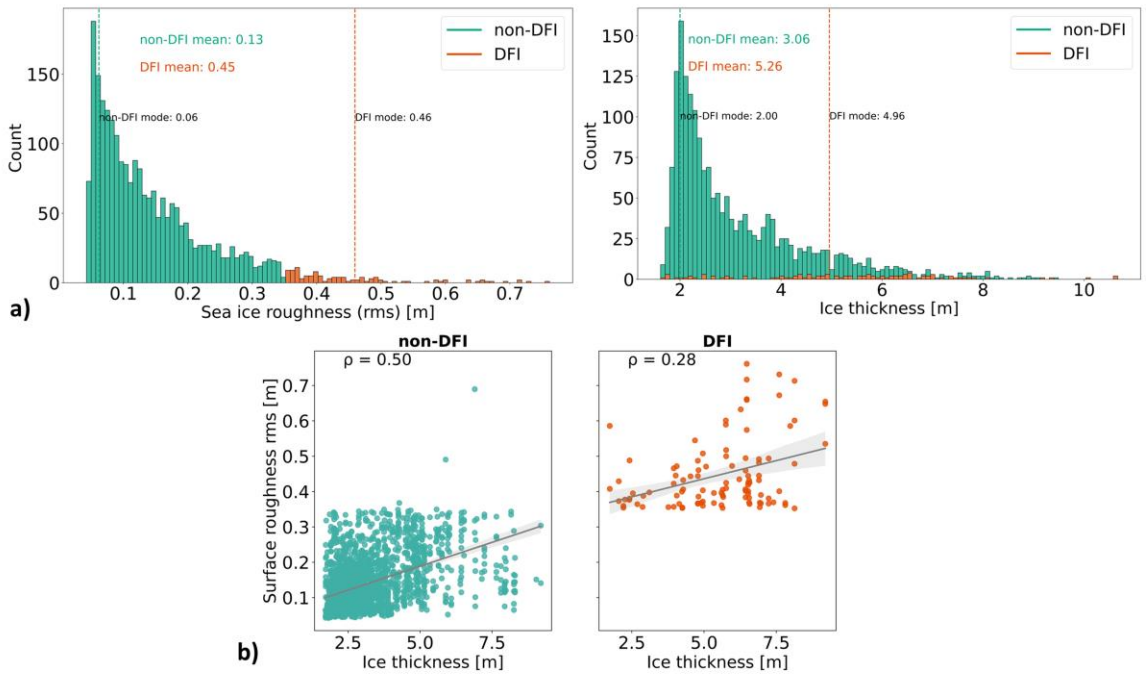

Figure 3.3: a) Late Winter (LW) sea ice surface roughness and thickness histograms for the overlapping SAR image portion of the survey line, indicating mode and mean statistics. Ice types are separated into deformed ice (DFI) and non-DFI based on a roughness threshold. b) Scatterplots between sea ice roughness and thickness for each type, showing the relationship between the two parameters using Spearman's correlation coefficient *(ρ)*.

3.4.2. C- and L- band SAR backscatter variability from LW to advance melt

The horizontal co-polarized (HH) band is selected to evaluate the backscatter variability in each stage, as it is robust for ice-water separation and deformation mapping (Dierking and Busche, 2007). Additionally, it is readily available for fully and dual-polarimetric SAR sensors. Figure 3.4 delineates the seasonal variability of HH backscatter for DFI, FYI, and MYI, revealing useful relationships for ice type backscatter variability and the influence of NR and FR incidence angles.

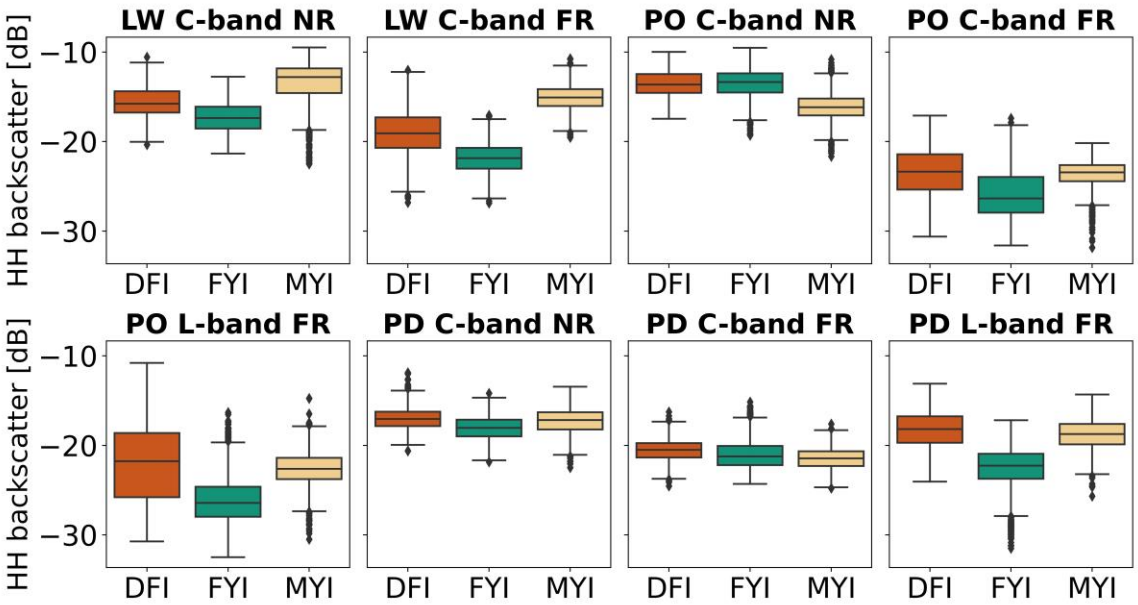

Figure 3.4: Boxplots presenting the distributions of each ice type at both C- and L-band during LW and over the advanced melt season. Each box consists of 400 pixels for FYI and MYI, while the DFI samples are based on ice roughness track points (120pixels).

During the LW phase, FYI and MYI are distinctly separate in C-band NR and FR scenes, with the predominant volumetric scattering from MYI resulting in an elevated backscatter signature. For smooth snow-covered FYI, linear and cross-polarized backscattering coefficients at near-range incidence angles exhibit higher backscatter when compared with

far-range angles (Geldsetzer et al., 2007). In contrast, DFI demonstrates an HH backscatter ranging between -11 to -20 dB (for NR) and -13 to -25 dB (for FR), positioning it between FYI and MYI backscatter signatures. For deformed ice surfaces, the incidence angle dependence of horizontal HH is lessened (Makynen et al., 2002). DFI scattering mechanisms are a complex mixture of both specular and diffuse contributions, including multiple scattering and edge diffraction (Carlstrom, 1997).

Across the advanced melt substages, DFI is characterized by consistently higher backscatter compared to FYI and MYI at both incidence angle ranges and frequencies. The differences are more pronounced for the L-band frequency due to its sensitivity to deformed sea ice in the advanced melt season (Dierking and Dall, 2007; Casey et al., 2016; Cafarella et al., 2019). Specifically in PO, FYI displays a pronounced backscatter rise in the NR, surpassing MYI that is not evident in the FR scenes from C- and L-band. Tavri et al. (2023) have posited that the heightened backscatter in the C-band NR can be influenced by high wind speeds at the time of acquisition. Upon examination of the ERA-5 atmospheric reanalysis wind speed data (at 10 m above sea level), it is evident that the wind speed during the C-band NR acquisition was 8.9 m/s, whereas it was 6.4 m/s during the FR acquisition. The variation in the backscatter response is fundamentally linked to the presence of melt ponds, with FYI exhibiting a heightened backscatter response compared to MYI, primarily due to an increased fraction of melt ponds. This effect is attributed to intensified Bragg scattering resulting from the unique characteristics of FYI. Conversely, in the FR acquisition, the backscatter response of FYI is lower than that of MYI. This disparity is influenced by the presence of calm melt ponds associated with specular reflection and the grazing incidence angle. The L-band acquisition in FR incidence angle presents similar distributions for FYI and MYI with C-band, except for DFI, which presents elevated HH backscatter.

In the PD substage, HH backscatter from C-band, in both NR and FR, converges, highlighting the complexities of ice type separability in this regime. However, the HH backscatter from L-band in FR presents better ice type separation, with DFI and MYI presenting elevated backscatter compared to FYI. This discrimination, as suggested by Singha et al. (2020) and Tavri et al. (2023), stems from enhanced sensitivity to volumetric

scattering from drained ice surfaces and deformation features, thereby proffering more ice type differences for this phase. L-band presents enhanced penetration capabilities, and with the surface drainage, there is an increased likelihood of volumetric interactions occurring with cracks and air voids within the deformed ice that increase DFI backscatter compared to MYI (Dierking and Dall, 2007).

3.4.3. *Ice type classification using C- and L- band SAR*

Figures 3.5 to 3.7 present the RF classification results for C- and L-band SAR imagery using the parameters listed in Table 3.2 as input.

Figure 3.5 depicts the LW classification results for the C-band SAR scenes. The study area comprises a mix of smooth FYI, large MYI floes, and several deformed ice features. The overall classification accuracies were 83% (Table 3.3) for both the C band NR and FR scenes, and the most important polarimetric parameter was HV for scenarios I and II. This is expected as HV is sensitive to volumetric scattering, allowing differentiation between FYI and MYI (Barber et al., 2001). The algorithm depicts FYI and MYI well, while DFI is misclassified as FYI in the FR and as MYI in the NR due to overlapping backscatter (Figure 3.4). In LW, MYI and DFI are characterized by stronger volumetric scattering, presenting strong returns and high backscatter, making their separation difficult. The combination of incidence angle ranges resulted in a small improvement in the overall classification accuracy (2%), however, the class-wise classification accuracies for FYI and MYI (90 to 95%) are high. Despite improving DFI class misclassifications, the class-wise accuracy is moderate (55%) (Table 3.3).

Table 3.3: Confusion matrices for C- and L-band SAR RF classification scenarios in LW, PO and PD

C-band NR — Late Winter (LW)

Reference pixels \ Classified pixels	DFI	FYI	MYI	Total	Producer's accuracy (%)
DFI	49	17	20	86	57
FYI	36	204	0	240	85
MYI	20	0	216	236	91
Total	105	221	236	562	
User's accuracy (%)	46	91	91		
Overall Accuracy (%)	**83**				

C-band NR — Pond Onset (PO)

Reference pixels \ Classified pixels	DFI	FYI	MYI	Total	Producer's accuracy (%)
DFI	45	34	13	92	49
FYI	57	151	32	240	63
MYI	27	35	176	238	74
Total	129	220	221	570	
User's accuracy (%)	35	67	80		
Overall Accuracy (%)	**65**				

C-band NR — Pond Drainage (PD)

Reference pixels \ Classified pixels	DFI	FYI	MYI	Total	Producer's accuracy (%)
DFI	31	27	31	89	35
FYI	34	148	60	242	61
MYI	71	73	98	242	40
Total	136	248	189	573	
User's accuracy (%)	23	60	52		
Overall Accuracy (%)	48				

C-band FR — Late Winter (LW)

Reference pixels \ Classified pixels	DFI	FYI	MYI	Total	Producer's accuracy (%)
DFI	46	30	11	87	53
FYI	32	205	1	238	86
MYI	19	1	220	240	92
Total	97	236	232	565	
User's accuracy (%)	47	87	95		
Overall Accuracy (%)	**83**				

C-band FR — Pond Onset (PO)

Reference pixels \ Classified pixels	DFI	FYI	MYI	Total	Producer's accuracy (%)
DFI	40	24	27	91	44
FYI	32	169	37	238	71
MYI	62	30	150	242	62
Total	134	223	214	571	
User's accuracy (%)	30	76	70		
Overall Accuracy (%)	**63**				

C-band FR — Pond Drainage (PD)

Reference pixels \ Classified pixels	DFI	FYI	MYI	Total	Producer's accuracy (%)
DFI	34	35	41	110	30
FYI	77	145	63	285	50
MYI	78	67	141	286	49
Total	189	247	245	680	
User's accuracy (%)	43	59	58		
Overall Accuracy (%)	**47**				

C-band NR + FR — Late Winter (LW)

Reference pixels \ Classified pixels	DFI	FYI	MYI	Total	Producer's accuracy (%)
DFI	52	24	11	87	60
FYI	27	211	0	238	89
MYI	16	0	220	236	93
Total	95	235	231	565	
User's accuracy (%)	55	90	95		
Overall Accuracy (%)	**85**				

C-band NR+FR — Pond Onset (PO)

Reference pixels \ Classified pixels	DFI	FYI	MYI	Total	Producer's accuracy (%)
DFI	61	17	12	90	68
FYI	45	175	23	243	72
MYI	28	28	186	242	77
Total	134	220	221	575	
User's accuracy (%)	45	79	84		
Overall Accuracy (%)	**73**				

C-band NR+FR — Pond Drainage (PD)

Reference pixels \ Classified pixels	DFI	FYI	MYI	Total	Producer's accuracy (%)
DFI	25	25	39	89	28
FYI	33	148	61	242	61
MYI	61	61	120	242	90
Total	119	234	220	573	
User's accuracy (%)	21	63	54		
Overall Accuracy (%)	**51**				

L- band FR — Pond Onset (PO)

Reference pixels \ Classified pixels	DFI	FYI	MYI	Total	Producer's accuracy (%)
DFI	40	39	20	99	40
FYI	50	173	37	260	66
MYI	45	45	170	260	65
Total	135	257	227	619	
User's accuracy (%)	30	67	75		
Overall Accuracy (%)	**62**				

L- band FR — Pond Drainage (PD)

Reference pixels \ Classified pixels	DFI	FYI	MYI	Total	Producer's accuracy (%)
DFI	44	6	32	82	54
FYI	28	191	19	238	80
MYI	75	27	133	235	57
Total	147	224	184	555	
User's accuracy (%)	30	85	72		
Overall Accuracy (%)	**66**				

C+L band — Pond Onset (PO)

Reference pixels \ Classified pixels	DFI	FYI	MYI	Total	Producer's accuracy (%)
DFI	50	10	7	67	75
FYI	31	137	20	188	73
MYI	30	9	147	186	79
Total	111	156	174	441	
User's accuracy (%)	45	88	84		
Overall Accuracy (%)	**76**				

C+L band — Pond Drainage (PD)

Reference pixels \ Classified pixels	DFI	FYI	MYI	Total	Producer's accuracy (%)
DFI	37	5	40	82	45
FYI	29	173	36	238	73
MYI	49	21	165	235	70
Total	115	199	241	555	
User's accuracy (%)	32	87	68		
Overall Accuracy (%)	**68**				

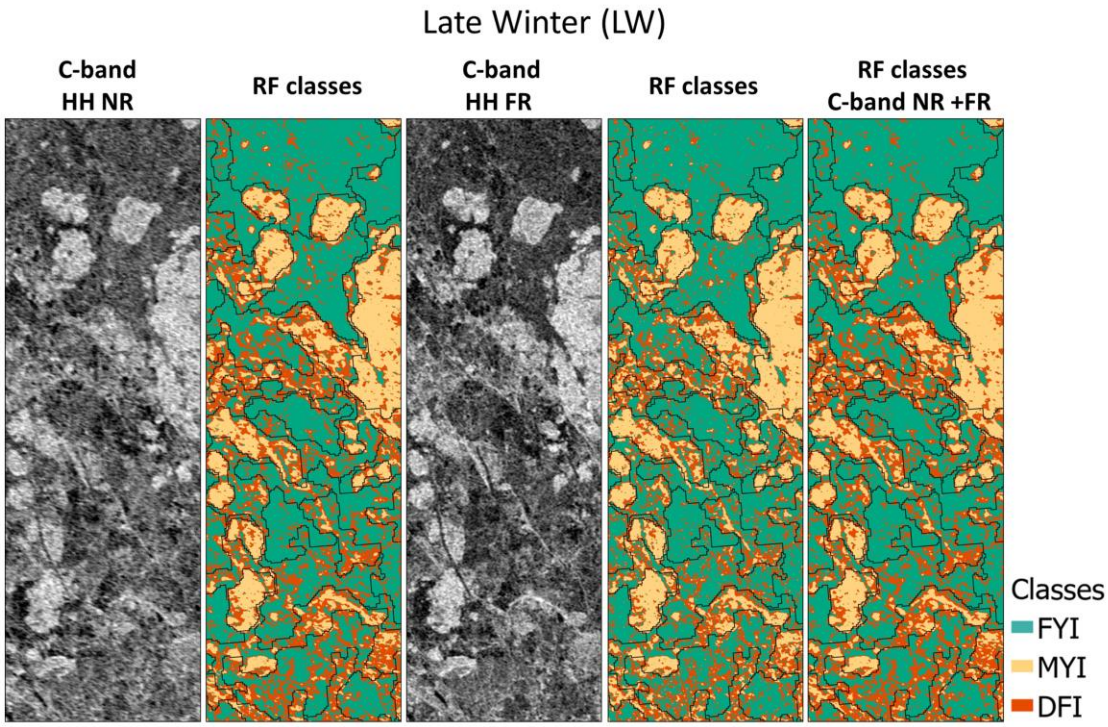

Figure 3.5: LW SAR HH subsets and classified images for C-band in NR and FR. Each classification output has image segmentation objects based on the LW SAR image overlaid for visual reference.

The first panel in Figure 3.6 displays the available overlapping high-resolution optical image, taken six days later than the C- and L-band SAR scenes in the PO substage. During this time, the melt pond fraction is spatially variable, with partially drained FYI and MYI areas visible alongside many flooded regions. A big portion of the image comprises smooth flooded FYI and thick MYI, while DFI regions are also visible.

The additional panels in Figure 3.6 illustrate the SAR HH scenes and the RF classification outputs for the three scenarios. The HH backscatter reversal relative to LW, described in section 3.4.2, supports better overall classification accuracies in this substage. Evaluation of classification results for scenario I, involving discrete examination of each frequency and incidence angle, demonstrated satisfactory precision. The overall class accuracy for C-band in the NR was 65%, compared to 63% in FR (Table 3.3). The increase in FYI backscatter, relative to MYI, led to the FYI signature overlap with DFI in the NR at C-band and the misclassification of FYI as DFI in this scenario. A slightly lower overall

accuracy was found for C-band FR, with better class-wise accuracy for FYI and MYI than DFI, which was mainly misclassified as MYI. The class-wise accuracy for MYI was highest in NR, while for FYI in the FR. Thus, the combination of NR and FR C-band parameters in scenario II, supports a ~10% improvement in the overall classification accuracies while minimizes the misclassifications for DFI (Table 3.3). Additionally, this approach minimizes class ambiguity between FYI and MYI at both incidence angle ranges.

The L-band classification has a lower overall accuracy of 62%, comparable to C-band FR. DFI was often misclassified as FYI and vice versa, creating an underestimation of deformed areas. Class-wise accuracies were better for MYI and FYI than DFI, which presented a high rate of false positives (User's accuracy= 30%), similar to C-band FR (Table 3.3). HH band was the most important metric for the classification, explaining 23% of the total dataset variability. Scenario III, combining C- and L-band SAR, yielded the highest overall classification accuracy of 76% and the highest class-wise accuracies for all classes. This fusion also augmented the discrimination of DFI, mitigating classification errors, especially for FYI (Table 3.3). The most valuable parameter for the RF model was the C-band HV/HH in the NR. This parameter effectively captures the influence of melt ponds on the scattering processes of both FYI and MYI during that stage, accentuating the distinctions between these ice types (Tavri et al., 2023). Scenarios II and III underscore the value of combining data sources for elucidating the ice type heterogeneity inherent in PO.

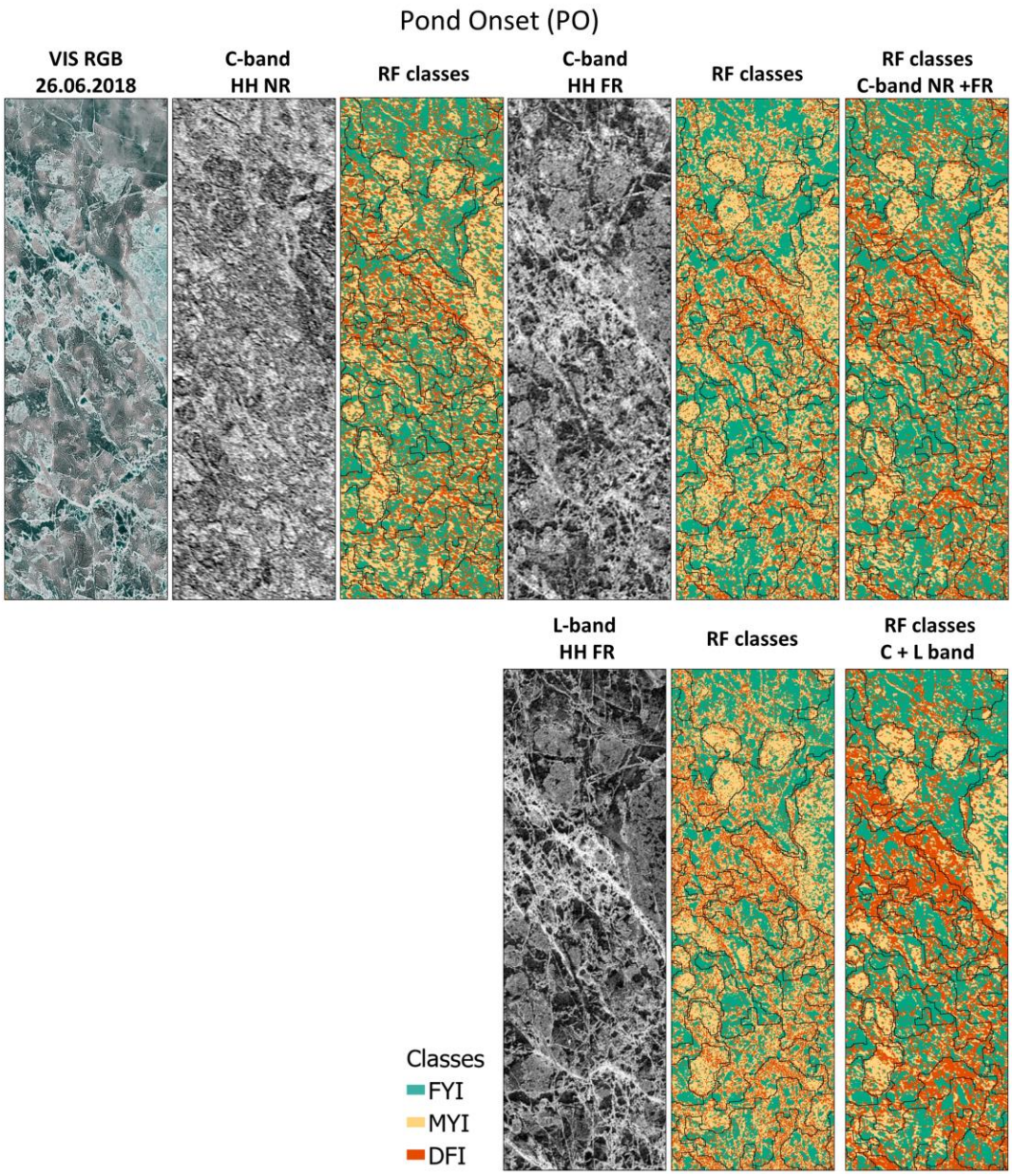

Figure 3.6: High-resolution optical scenes and classified images for C-band combining NR and FR scenes and C- and L-band for PO and PD stages for FYI, DFI and MYI. Each classification output has image segmentation objects based on the LW SAR image overlaid for visual reference.

Progressing to the PD substage, the relationships between ice types in both C- and L-band scenes are altered as the melt ponds drain. Typically, greater pond drainage is observed over FYI than MYI (Eicken et al., 2004; Scharien et al., 2012). The optical scene in the first panel of Figure 3.7, depicts the extensive surface drainage from FYI and MYI floes. SAR C-band HH imagery exhibits a grainy appearance, particularly in the FR, with moderately high backscatter for both FYI and MYI, making them indistinguishable. This is reflected in the classification results with low accuracies for both incidence angles and underestimation of MYI from the RF classifier. Conversely, DFI can be visually identified by its high HH backscatter in both C-band NR and FR, which contradicts the earlier findings of Casey et al. (2016), who could only identify deformed features in the L-band scenes. The overall classification accuracies in C- band NR and FR are similar, 48% and 47%, respectively. Both NR and FR show better class-wise accuracies for FYI. The most important parameter was HV/HH, as it is sensitive to changes in surface roughness and depolarization (Drinkwater et al., 1992). Scenario II offered a slight improvement in overall classification accuracy (51%), improving misclassifications in MYI. However, DFI remains underestimated, presenting low class-wise accuracies.

The L-band HH scene provides enhanced contrast between FYI and MYI, with a higher backscatter for MYI, possibly due to high signal penetration. DFI shows a higher mean HH backscatter in L-band FR than MYI (Figure 3.4), indicating the contribution of multiple scattering mechanisms to its backscatter signal. The higher signal penetration depth of longer wavelengths combined with the complex structure of cracks and voids within the DFI increase the probability of higher volumetric scattering contribution for this ice type (Dierking and Dall, 2007). Scenario I for the L-band FR, presents a good overall classification accuracy with 66% overall accuracy, with the highest accuracies for FYI, as there are misclassifications between MYI and DFI. The most important parameter was HV, in agreement with findings from Dierking and Dall (2007) that highlighted this parameter for deformation mapping using L-band SAR. For scenario III, combining C- and L-band improved overall accuracy to 68%, refining the misclassifications for MYI, while DFI was still misclassified as MYI (Table 3.3). For scenarios II and III, the most important parameter was C-band HH in NR.

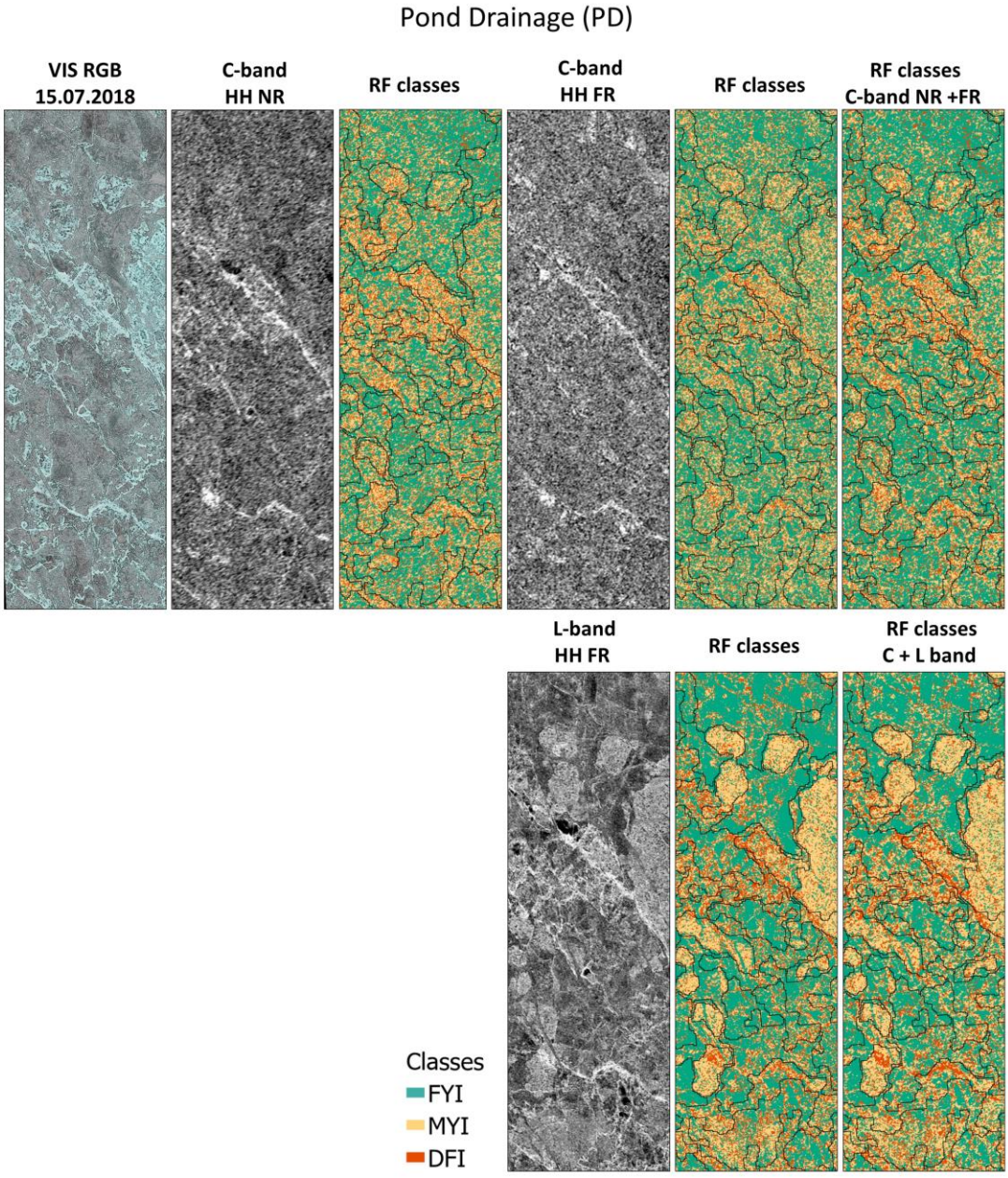

Figure 3.7: Classification results for C- and L-band SAR in PD for NR and FR incidence angles. Each classification output has image segmentation objects based on the LW SAR image overlaid for visual reference.

In addition, Table 3.4 depicts the out of bag MSE calculations from the training models per scenario and stage. The smallest MSE values are obtained for DFI and the combined incidence angle at C-band and combined frequency (C-band and L-band) scenarios, as would be anticipated due to the higher information content from the combined parameters. MSE for FYI and MYI presents higher variability, which is greater than the MSE for DFI. The lowest MSE for FYI and MYI was for the trained model in LW, with combined incidence angles.

Table 3.4: Out of bag MSE between the estimated value from the trained model and the actual value from each class ROI.

Classification scenarios	*DFI*	*FYI*	*MYI*
C-LW NR	1.078	5.298	2.654
C-LW FR	0.869	5.112	2.609
C-LW NR+FR	0.647	3.343	2.377
C-PO NR	0.436	14.288	10.964
C-PO FR	0.422	14.614	14.815
C-PO NR+FR	0.351	9.689	7.949
L-PO FR	0.399	13.721	13.562
C + L PO NR+FR	0.284	9.196	9.05
C-PD NR	0.551	13.134	22.762
C-PD FR	0.486	14.166	15.841
C-PD NR+FR	0.506	8.608	14.602
L-PD FR	0.477	7.561	15.432
C + L PD NR+FR	0.372	6.631	8.98

3.4.4. DFI validation with the airborne track

To evaluate the RF classification outputs for DFI, we compared them to the airborne-derived roughness points identified at DFI using a fixed roughness threshold. A transect plot depicts the point-to-point difference for each classification model over the same track points (Figure 3.8). This comparison reveals common misclassifications of each model, i.e., informing what drives the DFI accuracy. For the LW scene in the FR, DFI was most often misclassified as MYI, while in the later stages, DFI is predominantly misidentified as FYI. In the PO substage, the most accurate classification model is obtained for scenario III with the C- and L-band combined frequencies, while in the PD stage, the most accurate model is for scenario I, using the L-band. The least accurate model for identifying DFI is with the C-band parameters in PD. These results agree with the broader RF classification results, reinforcing the utility of combined SAR frequencies for DFI classification during PO and the utility of L-band for deformation mapping in the later stages of advanced melt during PD.

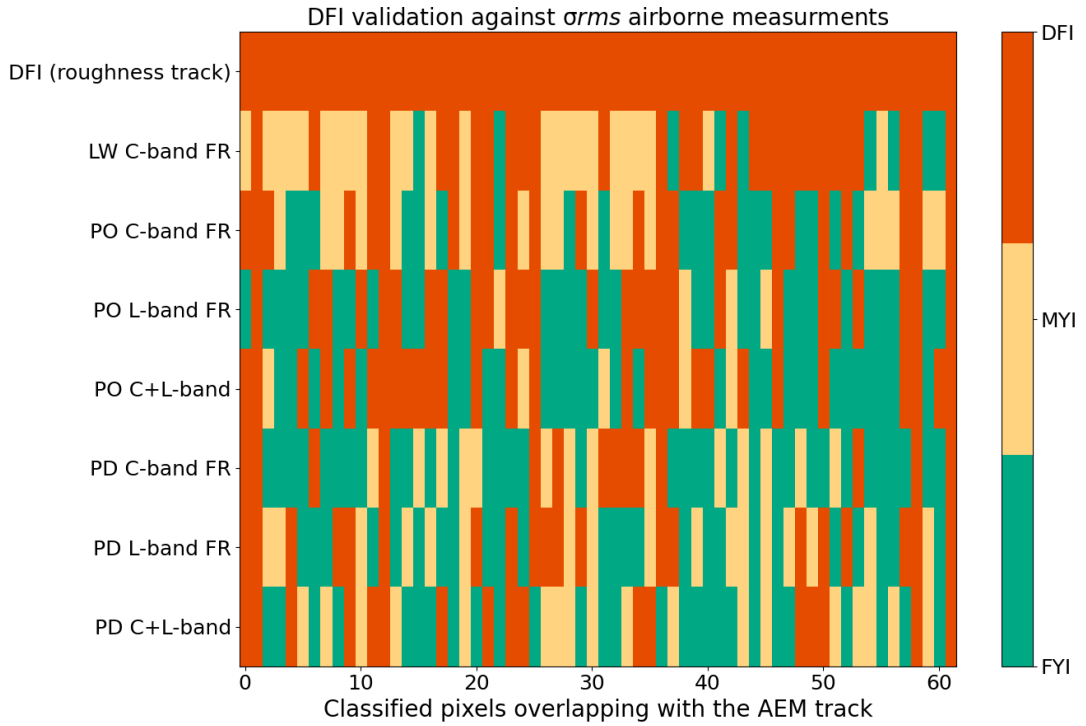

Figure 3.8: Transect plot for DFI class validation using in situ ice roughness data from the airborne survey track in LW. We compare only the results from the same incidence angle in FR for consistency between C- and L-band data.

Figure 3.9 presents the SAR pixel transect, depicting C- and L-band HH backscatter overlap with the AEM survey track during PO and PD. Star markers indicate DFI-labeled points along the track, facilitating the examination of their association with backscatter in each substage. To align with DFI point locations, an eight-measurement smoothing window has been applied to the measurements, revealing numerous deformed points and highlighting the distribution of DFI regions along the survey track. In FR, there is substantial variability in both C- and L-band HH backscatter during the advanced melt substages. Figure 3.9 showcases the SAR transect values, indicating a high HH backscatter overlap for C- and L-band in PO, while better HH backscatter separability is observed in PD. Analyzing the DFI point distributions and HH backscatter values along the survey track at C- and L-band frequencies shows that DFI mainly aligns with higher HH backscatter intensities in both substages, likely due to multiple scattering, which helps identify DFI during advanced melt.

Our findings demonstrate that the RF classifier is effective for classifying FYI and MYI in the LW, with DFI areas misclassified as MYI mainly since both types are characterized by strong volumetric scattering and higher surface roughness than smooth FYI. Progressing to the PO substage in the advanced melt season, surface scattering dominates FYI and MYI backscatter responses (Tavri et al., 2023), while DFI might be associated with more than one scattering mechanism. To further investigate this hypothesis, we employed the Freeman-Durden polarimetric decomposition to retrieve the relative scattering mechanisms of each ice type (Figure 3.10).

During LW, DFI and MYI have higher contributions of volumetric scattering in both NR and FR compared to FYI. During PO, for C-band in the NR, surface scattering dominates all ice type backscatter responses. DFI and FYI present similar contributions, explaining their misclassification by the RF model at this substage. In the FR, both C- and L-band show a combination of scattering mechanisms at play, influencing its backscatter signatures. In PO, L-band data exhibit high volumetric scattering contributions for all ice types. However, when considering the DFI scattering mechanisms in the PD substage, we notice an increase in volumetric scattering in the C-band NR. Interestingly, in the FR, the scattering distributions resemble those observed during the PO phase. The L-band FR scene

subtly departs from the PO distributions, particularly for the DFI and MYI types. DFI primarily exhibits surface scattering, while MYI is predominantly characterized by volumetric scattering.

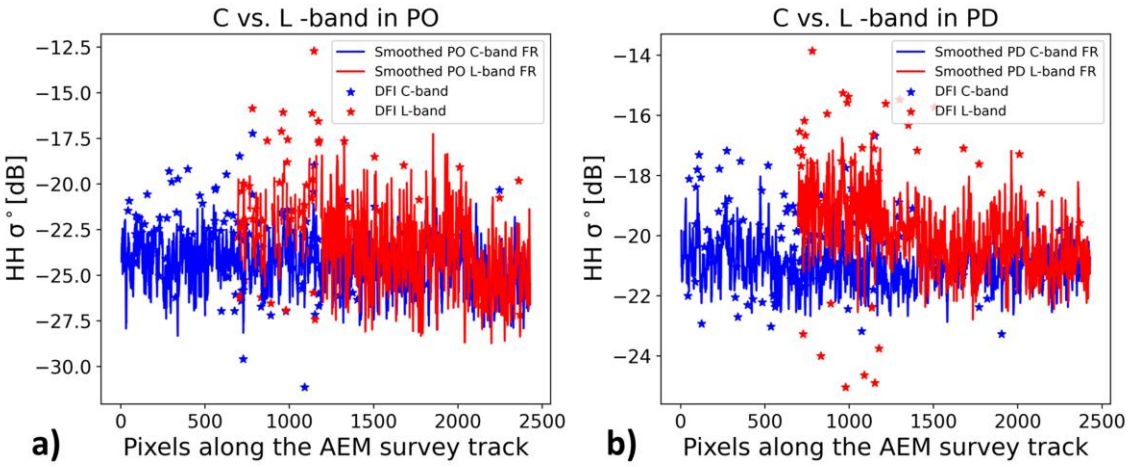

Figure 3.9: Line plots of C- and L-band HH backscatter along the AEM track, a) in PO and b) in PD. The lines are smoother with an 8-measurement averaging window size to support data comparison. Stars symbols indicate the survey points identified as DFI.

Throughout all seasonal stages, integrating C- and L-band SAR frequencies and incidence angles has proven to enhance classification outcomes, yielding higher classification accuracy, and improving the representation of each ice class within the prediction models. The combined frequency approach is advantageous during PO for improving misclassifications between the ice types and in PD, where it supports substantial improvements in class-wise accuracies compared to using a single frequency, especially in the case of C-band. The sensitivity of longer wavelengths to surface drainage offers a response that closely aligns with sea ice properties, making it especially valuable for identifying hazards in the later stages of the advanced melt season, when FYI is weakening and eventually breaking up.

Our investigation of SAR parameters has highlighted their capability to monitor large-scale roughness features during the advanced melt season, supporting operational requirements and climate model research. These larger roughness features possess the potential to exert more substantial influences on atmospheric and oceanic processes. Furthermore, the RF classification outputs for DFI uncovered recurring misclassifications useful for future studies. In LW, DFI tends to be misclassified as MYI, while in later stages, it is predominantly identified as FYI.

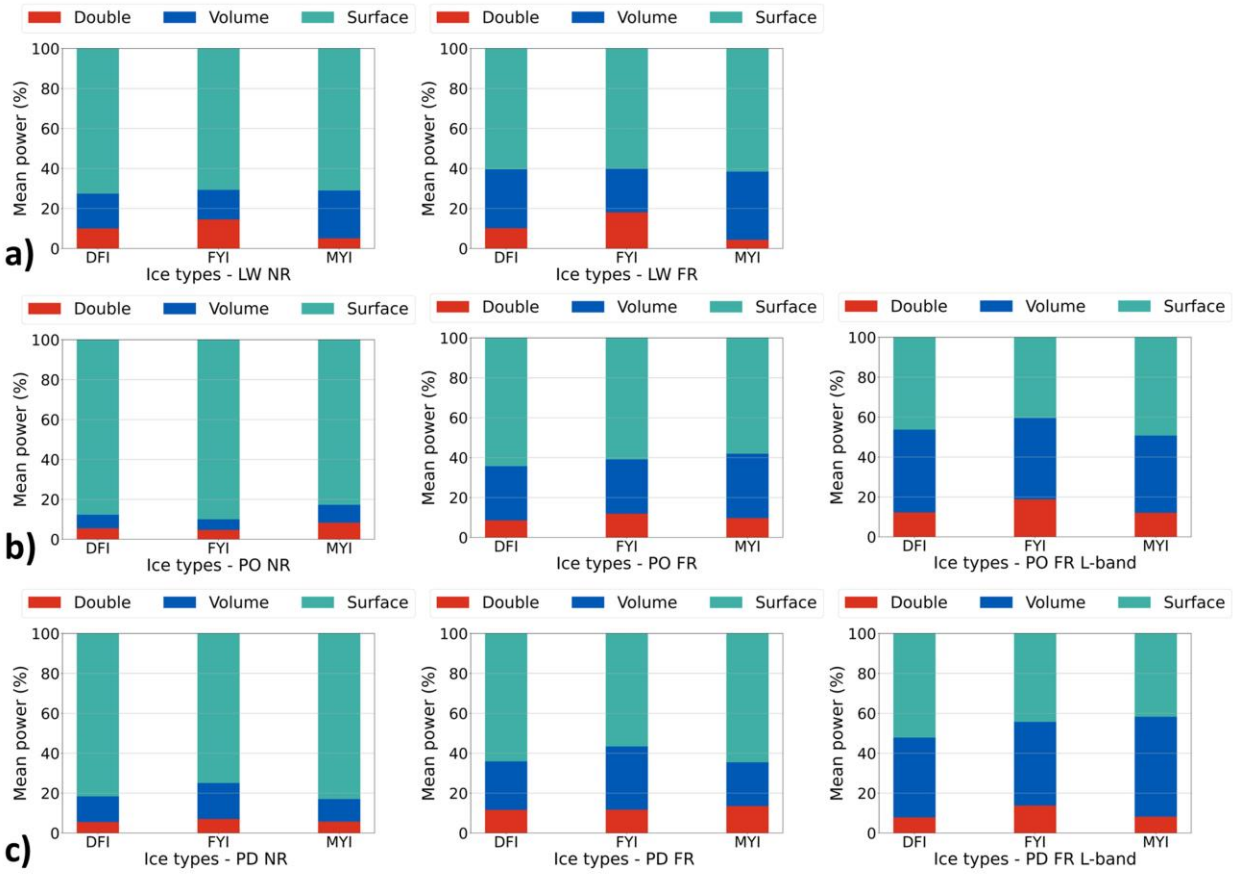

Figure 3.10: Stacked bar plots of relative scattering mechanisms for each ice type using the Freeman-Durden decomposition from C- and L-band band acquisitions in NR (left panels) and FR (right panels), with the L-band scenes indicated. Groups correspond to a) LW, b) PO, and c) PD.

3.5. **Conclusions**

We examined coincident C- and L-band fully polarimetric SAR scenes over landfast sea ice in the M'Clintock Channel of the Canadian Arctic Archipelago for sea ice classification in the advanced melt season. Three main ice types were identified based on reference winter SAR imagery, operational sea ice charts, and airborne data: FYI, MYI and DFI. We examined commonly available polarimetric parameters and used a random forest classification algorithm to explore three classification scenarios: scene-wise classification; combining near-range and far-range incidence angles at C-band frequency; and combining C- and L-band frequencies into a unified, dual-frequency classification approach. Airborne-derived surface roughness data from LW allowed us to identify DFI and validate our classification outputs for that class.

Our findings revealed the utility of combining NR and FR incidence angle acquisitions at C- and L-band frequencies in the advanced melt for improving ice type classification. We provided a detailed analysis of the DFI class across the season supported by in situ measurements from an airborne sea ice roughness and thickness survey. Based on the roughness and thickness distributions, the study area predominantly contained smooth, moderately thick ice, while DFI, despite exhibiting higher levels of roughness, displayed a diverse spectrum of thickness values. This observation underscores the notion that deformation within the ice is not inherently associated with greater ice thickness. The observed backscatter variability outlined the potential for ice type classification at each stage. In the LW, C-band SAR revealed a distinct separation between FYI and MYI in both NR and FR scenes, with predominant volumetric scattering from MYI leading to elevated backscatter. Across the advanced melt substages, DFI was characterized by higher backscatter compared to FYI and MYI at both incidence angle ranges and frequencies. In the PO, FYI exhibited higher backscatter in the NR compared to MYI, influenced by wind speed and the presence of melt ponds aiding class separation. L-band acquisition in PO presented similar backscatter distributions as C-band, except for DFI, which showed elevated HH backscatter. In the PD, C-band HH backscatter in NR and FR converged,

complicating ice type separability. However, in L-band FR, the HH backscatter supported better discrimination, with DFI and MYI displaying higher backscatter than FYI. This enhancement is attributed to the sensitivity of L-band to volumetric scattering from drained ice surfaces and deformation features, providing clearer ice type differences in this phase.

Each classification scenario yielded important findings. For the C-band SAR scenes in the LW phase (Scenario I), the overall classification accuracies are 83% for both NR and FR scenes, with HV as the most important parameter for the classification performance. FYI and MYI were well depicted, but DFI was misclassified as FYI in FR and as MYI in NR due to overlapping backscatter. In this phase, MYI and DFI exhibit strong volumetric scattering, making their separation challenging. For Scenario II, we combined NR and FR incidence angle acquisitions, improving overall and class-wise accuracies for all types. Progressing to PO, for scenario I, classification using C-band parameters achieved an overall class accuracy of 65% in NR and 63% in FR. The increased FYI backscatter relative to MYI led to FYI, and DFI overlap in NR, while in FR, DFI was mainly misclassified as MYI. L-band classification had a lower overall accuracy of 62%, with DFI frequently misclassified as FYI. Scenario II combined C-band SAR from NR and FR, resulting in a 10% improvement in overall classification accuracy and reduced DFI misclassifications. In Scenario III, the synergy of C- and L-band SAR yielded the highest overall classification accuracy of 76% in the PO substage, improving DFI discrimination and reducing classification errors, especially for FYI. C-band HV/HH in NR was the most valuable parameter for this fusion model, highlighting the effect of melt ponds on FYI and MYI scattering. In PD, for scenario I, C-band SAR data could not offer a good distinction between the ice types, with low overall classification accuracies (48% in NR and 47% in FR), mainly underestimating MYI. The L-band FR achieved good overall classification accuracy (66%) with misclassifications of MYI as DFI. Scenario II offered a slight improvement in overall classification accuracy (51%). However, scenario III yielded the best classification accuracies (68%) in PD. Combining C- and L-band frequencies refined MYI misclassifications however, DFI was misclassified as MYI in some cases.

MSE calculations revealed that the smallest MSE values were obtained for DFI for the combined models (incidence angle at C-band and frequency at C-band and L-band), while

FYI and MYI exhibited higher and more variable MSE values, with the lowest MSE for FYI and MYI occurring in the LW model with combined incidence angles.

Despite the inherent challenges in devising a robust methodology for sea ice type classification during advanced melt stages, our investigation underscores the efficacy of a combined C- and L-band frequency approach, yielding enhanced classification accuracies relative to single frequencies amidst challenging ice conditions. Using a straightforward and efficient classifier, we provided valuable baseline information on FYI, MYI, and DFI classification using C- and L-band SAR backscatter and polarization ratios in the advanced melt season. Our findings pave the way for the utilization of L-band SAR data from future missions like NASA-ISRO's NISAR, JAXA's PALSAR-3, ESA's high-priority ROSE-L, and DLR's proposed Tandem-L, which hold great promise for enhancing summer sea ice type retrievals, especially when used in combination with the already well-established C-band frequency SAR missions like Sentinel-1 and RCM. Future steps involve expanding this analysis by combining SAR image acquisitions with comprehensive in situ data of sea ice type specific geophysical properties at micro- and geometric- scales.

3.6. Acknowledgments

Special thanks to Malin Johansson for providing the two ALOS-2 PALSAR-2 scenes from JAXA under the 3rd Research Announcement on Earth Observations (PI: Malin Johansson PER3A2N093). We also thank Christian Haas for providing EM bird ice thickness data and Environment and Climate Change Canada's Climate Research Division for the high-resolution GeoEye-1 and Worldview-2 images.

3.7. Funding

The research was funded by the Marine Environmental Observations and Predictions and Response (MEOPAR) Network (1-02-02-004.5), Natural Sciences and Engineering Research Council of Canada Discovery (RGPIN-2022-05217), and Polar Knowledge Canada (POLAR) Science and Technology (NST-1718-0024) grants to Scharien. JAXA provided ALOS-2/PALSAR-2 scenes under the 6th ALOS Research Announcement (Project 3348; PI: Scharien).

Chapter 4. Conclusions

Arctic sea ice is replenishing, with its extent being rapidly declining in the past decades, dominated by thinner FYI types and characterized by longer melt seasons. Identifying, mapping, and understanding sea ice properties in the advanced melt is a challenging endeavor due to variable and complex melt conditions, as well as the limited observations during this season. This gaps in comprehending the relationships between sea ice geophysical properties and SAR signatures in the advanced melt season have important implications on expanding scientific knowledge, improving operational services products, and inform climate models parametrizations.

This dissertation has outlined the relationships between sea ice geophysical properties and C- and L-band SAR signatures in the advanced melt season considering fully and compact polarimetric data. The findings support improvements for summer sea ice retrievals, demonstrating effective products that strengthen existing knowledge for the new Arctic regime. This dissertation is based on two lead-author publications as original works, using multi-polarimetric and multifrequency SAR imagery to explain sea ice backscatter variability in the early and advanced melt season. Chapter 1 presented the sea ice nomenclature and background, as well as the research rationale and motivation. In Chapter 2, Arctic sea ice type separability in the melt season was assessed using fully and compact polarimetric C- and L-band SAR. Additionally, dominating scattering mechanisms of each ice type were outlined evaluating the influence of variable incidence angle and melt ponds on ice type backscatter. Chapter 3 examined a synergy of C- and L-band SAR for Arctic ice type classification in the advanced melt season, particularly investigating deformed ice types and their evolution in the advanced melt season. It outlined the substantial improvements of ice type classification in the advanced melt season. Especially when elaborating a dual-frequency and dual-incidence angle to classify FYI, MYI and DFI. Importantly, airborne sea ice roughness and thickness data validated the deformed ice classification offering insights in misclassifications and class-wise accuracies in the advanced melt season.

4.1. Summary of key findings

This research can be summarized by highlighting key findings and contributions in two chapters:

Chapter 2: This chapter delved into the evaluation of fully and compact polarimetric data from C- and L-band SAR imagery for distinguishing different sea ice types during advanced melt conditions. Using data from RADARSAT-2 and ALOS-2 PALSAR-2 satellites, along with high-resolution optical imagery, the study examined the evolution and coverage of surface melt ponds. It aimed to provide insights into key queries related to frequency selection, the effectiveness of polarimetric parameters, and the influence of melt ponds on backscatter characteristics. The results uncovered distinct advantages of C-band SAR for differentiating FYI and MYI during the pond onset stage, where FP and CP parameters related to surface scattering displayed consistent separability. In contrast, L-band SAR exhibited better separability during pond drainage as its longer wavelength depicted higher volumetric scattering contributions from MYI. The research also demonstrated that CP parameters were on par with FP parameters in terms of effectiveness, with key polarimetric parameters outlining the dominating scattering mechanisms at each substage. The analysis of melt ponds revealed their significant impact on backscatter, especially on co and cross-polarization ratio during pond onset. This work underscores the advantages of complimentary use of medium and lower SAR frequencies for enhancing sea ice type separability in the advanced melt season. Importantly, it demonstrated the capacity of CP data to provide good separability in each melt stage, reinforcing the use of products from RCM for enhancing melt season retrievals. This work also showcased the capacity of commonly available polarimetric bands like HH and HV, along with their ratios, to differentiate FYI and MYI types across the melt season, expanding the practical implications of this research.

Chapter 3: This chapter presented a comprehensive analysis of coincident C- and L-band fully polarimetric SAR scenes over landfast sea ice in the M'Clintock Channel of the CAA during the 2018 advanced melt season. Three primary ice types, FYI, MYI, and DFI, were identified using reference winter SAR imagery, operational sea ice charts, and airborne

data. We explored multiple classification scenarios, including combining near-range and far-range incidence angles at C-band frequency and integrating both C- and L-band frequencies into a dual-frequency classification approach. Notably, combining C- and L-band SAR data showed substantial improvements in ice type classification, particularly during late advanced melt. Additionally, we identified the most valuable parameters for each scenario and discussed the challenges and opportunities for sea ice type classification in advanced melt conditions. These results offer valuable insights for the utilization of future SAR missions, such as NASA-ISRO's NISAR and ESA's ROSE-L, to improve summer sea ice type retrievals, complementing existing C-band SAR missions like Sentinel-1 and RCM.

4.2 Significance implications and recommendations

The implications of this research are multifaceted and far-reaching. It underscores the importance of harnessing SAR frequencies and incidence angles in tandem to elevate the quality of sea ice information dissemination. This, in turn, reinforces several Arctic activities, including safe navigation and community operations, by providing more accurate and timely sea ice products. Arctic amplification and climate change over the past three decades have resulted in less predictable ice travel conditions, characterized by thinner, flooded, and rougher ice conditions, delayed freeze-up, earlier melt onset, and faster ice breakup. Chapters 2 and 3 presented invaluable information for ice service providers and coastal communities demonstrating the advantages of C- and L-band synergy for ice type identification and classification at early and advanced melt sages. Furthermore, the study highlights the need for cross-validating data from multiple sensors and missions, thereby enhancing the accuracy and reliability of sea ice monitoring during the advanced melt season.

To enhance the influence of this research and expand upon its foundations, several key recommendations emerge:

- Enhance in situ observations of sea ice geophysical properties in the advanced melt. Basic measurements of sea ice geophysical properties

during advanced melt conditions including scattering and radiative properties, are scarce but valuable for remote sensing and modeling purposes. Future field campaigns should focus on establishing the spatial and temporal characteristics of these properties, including thickness, temperature, salinity, brine volume, dielectric permittivity, wetness, surface layer grain size, and grain structure directly coincident to remote sensing datasets.

- Elaborate data fusion and cross-validation from diverse sensors and missions to enhance sea ice monitoring and data scaling during the advanced melt season. Specifically for evaluating melt pond parameters such as depth and areal fraction evolution and improve the accuracy and robustness of sea ice classification and sea ice type property retrievals in local and regional scales across the advanced melt season.

- Enhance climate modeling: Explore the ways in which improved sea ice retrievals can enrich climate modeling and contribute to assessments and implication of longer and earlier melt seasons in global climate processes. Accurate representation of geophysical parameters, including melt pond fraction, is pivotal for climate modeling and informs strategies for both mitigation and adaptation to climate change.

- Foster collaborative partnerships: Forge collaborative partnerships with operational ice services and local communities, with a particular focus on engaging indigenous communities. These collaborations are pivotal for tailoring remote sensing data to support real-time decision-making and ensuring that solutions are culturally sensitive. Incorporating local knowledge can yield more effective approaches to address sea ice-related challenges.

Given the inherently global nature of Arctic transformations, the promotion of international cooperation in data sharing, research initiatives, and disaster response planning stands as a critical imperative. Collaborative efforts, exemplified by initiatives like MOSAiC, offer unique and promising avenues for deepening our comprehension of the intricate Arctic system. Datasets collected during the expedition align with the aforementioned recommendations of establishing an observation network focused on studying sea ice properties during the summer melt season, encompassing various sea ice regimes, sampling locations and datasets.

4.3 Research limitations

The combination of dual frequency for SAR sea ice mapping and operational sea ice monitoring is still a challenge due to limited spatiotemporal coverage of L-band data, inconsistent viewing geometry and limited overlapping image availability. Recently, SAOCOM 1A and 1B joined ALOS-2, providing L-band imagery for earth observation purposes. While attempts have been made to assess their suitability for Arctic sea ice monitoring, it's important to note that these satellites were primarily designed for monitoring natural disasters, limiting their usability for sea ice research. In this doctoral research, the temporal resolution of L-band imagery posed a limitation in accurately estimating sea ice thermodynamic properties across the melt season. To develop a robust algorithm for operational sea ice monitoring, simultaneous data acquisition from L-band and other SAR sensors, coupled with in-situ measurements, is essential. The upcoming NISAR mission and ROSE-L mission are geared towards polar region exploration, offering the scientific community an opportunity to delve into high spatiotemporal resolution L-band SAR, overlapping with C-band imagery for sea ice research.

Additionally, this research is confined in one location in the CAA, over landfast sea ice. While landfast ice conditions are ideal for this analysis, as they reflect the thermodynamic changes in sea ice conditions and allow for tracking the same ice floes throughout the melt season, it is also important to consider examining regions of drifting pack ice. These areas are likely to display unique melt pond and sea ice characteristics, along with dynamic processes that differ from the land fast ice conditions we have studied.

Particular consideration should be given to the footprint of SAR sensors because it can lead to uncertainty, given the diverse characteristics of snow-covered sea ice surfaces. Although fully polarimetric data offers high spatial resolution and smaller footprints, additional research is necessary to establish a connection between the small-scale to the large-scale sea ice roughness that is observed by SAR images. This will enhance our ability to interpret microwave measurements related to dynamic changes in snow and sea ice geophysical properties.

References

Arkett, M., Flett, D., De Abreu, R., Clemente-Colon, P., Woods, J., and Melchior, B. (2008). Evaluating ALOS/PALSAR for ice monitoring — What can L-band do for the North American Ice Service, IEEE International Geoscience and Remote Sensing Symposium Proceedings 2008, 5, 188–191. http://dx.doi.org/10.1109/IGARSS.2008.4780059

Armour, K. C., Eisenman, I., Blanchard-Wrigglesworth, E., McCusker, K. E., and Bitz, C. M. (2011). The reversibility of sea ice loss in a state-of-the-art climate model. Geophysical Research Letters, *38*(16).

Barber, D. G., and Nghiem, S. V. (1999). The Role of Snow on the Thermal Dependence of Microwave Backscatter Over Sea Ice. Journal of Geophysical Research, 104. https://doi.org/10.1029/1999JC900181

Barber, D. G., Hanesiak, J. M., and Yackel, J. J. (2001). Sea ice, RADARSAT-1 and arctic climate processes: A review and update. Canadian Journal of Remote Sensing, 27(1), 51–61. doi:10.1080/07038992.2001.10854919

Barber, D. G., McCullough, G., Babb, D., Komarov, A. S., Candlish, L. M., Lukovich, J. V., ... and Rysgaard, S. (2014). Climate change and ice hazards in the Beaufort Sea. Elementa, 2, 000025.

Barry, R. G. (1989). The present climate of the Arctic Ocean and possible past and future states. In Y. Herman (Ed.), The Arctic seas. Climatology, Oceanography Geology and Biology (pp. 1-46). van Nostrand Reinhold.

Beckers, J. F., Renner, A. H., Spreen, G., Gerland, S., and Haas, C. (2015). Sea-ice surface roughness estimates from airborne laser scanner and laser altimeter observations in Fram Strait and north of Svalbard. Annals of Glaciology, 56(69), 235-244.

Belgiu, M., and Dr˘agu¸T. (2016). Random forest in remote sensing: A review of applications and future directions, ISPRS J. Photogramm. Remote Sens.,vol. 114, pp. 24–31.

Benz, U. C., P. Hofmann, G. Willhauck, I. Lingenfelder, and M. Heynen. (2004). Multi-Resolution, Object-Oriented Fuzzy Analysis of Remote Sensing Data for GIS-Ready Information. ISPRS Journal of Photogrammetry and Remote Sensing 58 (3-4): 239-258.

Boisvert, L. N., and Stroeve, J. C. (2015). The Arctic is becoming warmer and wetter as revealed by the Atmospheric Infrared Sounder. *Geophysical Research Letters*, *42*(11), 4439-4446.

Breiman, L. Random Forests. Machine Learning 45, 5–32 (2001). https://doi.org/10.1023/A:1010933404324

Cafarella, S. M., Scharien, R., Geldsetzer, T., Howell, S., Haas, C., Segal, R., and Nasonova, S. (2019). Estimation of level and deformed first-year sea ice surface roughness in the Canadian Arctic Archipelago from C-and L-band synthetic aperture radar. Canadian Journal of Remote Sensing, 45(3-4), 457-475.

Canadian Ice Service. (2011). Sea Ice Climatic Atlas: Northern Canadian Water 1981-2010. Ottawa. Retrieved from https://www.ec.gc.ca/glaces-ice/default.asp?lang=Enandn=4B35305B-1

Carlstrom, A. (1997). A microwave backscattering model for deformed first-year sea ice and comparisons with SAR data. *IEEE transactions on geoscience and remote sensing*, 35(2), 378-391.

Carsey, F. D. (Ed.). (1992). Microwave remote sensing of sea ice. American Geophysical Union.

Casey, J. A., Beckers, J., Busche, T., and Haas, C. (2014). Towards the retrieval of multi-year sea ice thickness and deformation state from polarimetric C- and X-band SAR observations, International Geoscience and Remote Sensing Symposium (IGARSS), IEEE 1190–1193, https://doi.org/10.1109/IGARSS.2014.6946644.

Casey, J. A., Howell, S. E. L., Tivy, A., and Haas, C. (2016). Separability of Sea Ice Types from Wide Swath C- and L-Band Synthetic Aperture Radar Imagery Acquired During the Melt Season. *Remote Sensing of Environment*, 174, 314-328. https://doi.org/10.1016/j.rse.2015.12.021

Charbonneau, F. T., Brisco, B., Raney, R. K., McNairn, H., Liu, C., Vachon, P. W., ... and Geldsetzer, T. (2010). Compact Polarimetry Overview and Applications Assessment. *Canadian Journal of Remote Sensing*. https://doi.org/10.5589/m10-062

Cloude, S. R., and Pottier, E. (1997). An entropy based classification scheme for land applications of polarimetric SAR. *IEEE transactions on geoscience and remote sensing*, *35*(1), 68-78.

Cloude, S. R., Goodenough, D. G., and Chen, H. (2012). Compact Decomposition Theory. *IEEE Geoscience and Remote Sensing Letters*, 9(1), 28–32. https://doi.org/10.1109/LGRS.2011.2158983

Colbeck, S. C., and Anderson, E. A. (1982). The permeability of a melting snow cover. Water Resources Research, *18*(4), 904-908.

Cole, S. T., Toole, J. M., Lele, R., Timmermans, M. L., Gallaher, S. G., Stanton, T. P., Shaw, W. J., Hwang, B., Maksym, T., Wilkinson, J. P., Ortiz, M., Graber, H., Rainville, L., Petty, A. A., Farrell, S. L., Richter-Menge, J. A., and Haas, C. (2017). Ice and ocean velocity in the Arctic marginal ice zone: Ice roughness and momentum transfer, Elementa, 5, 55, https://doi.org/10.1525/elementa.241, 2017.

Comiso, J. C., and Kwok, R. (1996). Surface and radiative characteristics of the summer Arctic sea ice cover from multisensor satellite observations. Journal of Geophysical Research: Oceans, 101(C12), 28397-28416.

Congalton, R. G. (1991). A review of assessing the accuracy of classifications of remotely sensed data. Remote sensing of environment, 37(1), 35-46.

Dabboor, M., and Geldsetzer, T. (2014). Towards Sea Ice Classification Using Simulated RADARSAT Constellation Mission Compact Polarimetric SAR Imagery. *Remote Sensing of Environment*, 140, 189–195. https://doi.org/10.1016/j.rse.2013.08.035

Dabboor, M., Montpetit, B., and Howell, S. (2018). Assessment of the high resolution SAR mode of the RADARSAT constellation mission for first year ice and multiyear ice characterization. Remote Sensing, 10(4), 594.

Dabboor, M., Montpetit, B., Howell, S., and Haas, C. (2017). Improving sea ice characterization in dry ice winter conditions using polarimetric parameters from C-and L-band SAR data. *Remote Sensing*, 9(12), 1270.

De Abreu, R., Yackel, J., Barber, D., and Arkett, M. (2001). Operational satellite sensing of Arctic first-year sea ice melt. Canadian Journal of Remote Sensing, *27*(5), 487-501.

Derksen, C., Burgess, D., Duguay, C., Howell, S., Mudryk, L., Smith, S., ... and Kirchmeier-Young, M. (2018). Changes in snow, ice, and permafrost across Canada; Chapter 5 in Canada's Changing Climate Report,(ed.) E. Bush and DS Lemmen; Government of Canada, Ottawa, Ontario.

Dierking, W. (2010). Mapping of different sea ice regimes using images from Sentinel-1 and ALOS synthetic aperture radar. IEEE Transactions on Geoscience and Remote Sensing, 48(3), 1045–1058. http://dx.doi.org/10.1109/TGRS.2009.2031806

Dierking, W. (2013). Sea ice monitoring by synthetic aperture radar. *Oceanography*, *26*(2), 100-111.

Dierking, W., and Busche, T. (2006). Sea Ice Monitoring by L-Band SAR: An Assessment Based on Literature and Comparisons of JERS-1 and ERS-1 Imagery. IEEE Transactions on Geoscience and Remote Sensing, 44(4), 957–970. http://dx.doi.org/10.1109/TGRS.2005.861745

Dierking, W., and Dall, J. (2007). Sea ice deformation state from synthetic aperture radar imagery — Part I: Comparison of C- and L-band and different polarization. IEEE Transactions on Geoscience and Remote Sensing, 45(11), 3610–3622. http://dx.doi.org/10.1109/TGRS.2007.903711

Dorn, W., Dethloff, K., Rinke, A., Frickenhaus, S., Gerdes, R., Karcher, M., and Kauker, F. (2007). Sensitivities and uncertainties in a coupled regional atmosphere-ocean-ice model with respect to the simulation of Arctic sea ice. Journal of Geophysical Research: Atmospheres, *112*(D10).

Döscher, R., Vihma, T., and Maksimovich, E. (2014). Recent advances in understanding the Arctic climate system state and change from a sea ice perspective: a review. *Atmospheric Chemistry and Physics*, *14*(24), 13571-13600.

Drinkwater, M. R., Crawford, J. P., and Cavalieri, D. J. (1991). Multi-frequency, multi-polarization SAR and radiometer sea ice classification. In IGARSS"91: Annual International Geoscience and Remote Sensing Symposium.

Drinkwater, M. R., Kwok, R., Rignot, E., Israelsson, H., Onstott, R. G., and Winebrenner, D. P. (1992). Potential applications of polarimetry to the classification of sea ice. Microwave remote sensing of sea ice, 68, 419-430.

Dubois-Fernandez, P. C., Souyris, J. C., Angelliaume, S., and Garestier, F. (2008). The compact polarimetry alternative for spaceborne SAR at low frequency. *IEEE Transactions on Geoscience and Remote Sensing*. doi:10.1109/TGRS.2008.919143

Early, D. S., and Long, D. G. (2001). Image Reconstruction and Enhanced Resolution Imaging from Irregular Samples. IEEE Transactions on Geoscience and Remote Sensing, 39(2), 291–302. doi:10.1109/36.905237

Eicken, H. (2002). Tracer Studies of Pathways and Rates of Meltwater Transport through Arctic Summer Sea Ice. Journal of Geophysical Research, 107(C10), 1–20. doi:10.1029/2000JC000583

Eicken, H., and Mahoney, A. R. (2015). Sea ice: Hazards, risks, and implications for disasters. In Coastal and marine hazards, risks, and disasters (pp. 381-401). Elsevier.

Eicken, H., Grenfell, T. C., Perovich, D. K., Richter-Menge, J. A., and Frey, K. (2004). Hydraulic controls of summer Arctic pack ice albedo. Journal of Geophysical Research: Oceans, 109(C8).

Eicken, H., Lensu, M., Leppäranta, M., Tucker III, W. B., Gow, A. J., and Salmela, O. (1995). Thickness, structure, and properties of level summer multiyear ice in the Eurasian sector of the Arctic Ocean. Journal of Geophysical Research: Oceans, 100(C11), 22697-22710.

Espeseth, M. M., Brekke, C., and Johansson, A. M. (2017). Assessment of RISAT-1 and Radarsat-2 for sea ice observations from a hybrid-polarity perspective. Remote Sensing, 9(11), 1088.

Fors, A. S., Brekke, C., Doulgeris, A. P., Eltoft, T., Renner, A. H., and Gerland, S. (2016). Late-summer sea ice segmentation with multi-polarisation SAR features in C and X band. The Cryosphere, 10(1), 401-415.

Freeman, A., and Durden, S. L. (1998). A three-component scattering model for polarimetric SAR data. IEEE transactions on geoscience and remote sensing, 36(3), 963-973.

Freitag, J., and Eicken, H. (2003). Meltwater circulation and permeability of Arctic summer sea ice derived from hydrological field experiments. *Journal of glaciology*, *49*(166), 349-358.

Geldsetzer, T., Langlois, A., and Yackel, J. (2009). Dielectric properties of brine-wetted snow on first-year sea ice. Cold Regions Science and Technology, 58(1-2), 47-56.

Geldsetzer, T., Arkett, M., Zagon, T., Charbonneau, F., Yackel, J. J., and Scharien, R. K. (2015). All-Season Compact-Polarimetry C-band SAR Observations of Sea Ice. Canadian Journal of Remote Sensing, 41(5), 485–504. https://doi.org/10.1080/07038992.2015.1120661.

Geldsetzer, T., Mead, J. B., Yackel, J. J., Scharien, R. K., and Howell, S. E. (2007). Surface-based polarimetric C-band scatterometer for field measurements of sea ice. IEEE Transactions on Geoscience and Remote Sensing, 45(11), 3405-3416.

Gill, J. P., and Yackel, J. J. (2012). Evaluation of C-band SAR polarimetric parameters for discrimination of first-year sea ice types. Canadian Journal of Remote Sensing, 38(3), 306-323.

Giles, K. A., Laxon, S. W., and Ridout, A. L. (2008). Circumpolar thinning of Arctic sea ice following the 2007 record ice extent minimum. Geophysical Research Letters, 35(22).

Gillett, N. P., Stone, D. A., Stott, P. A., Nozawa, T., Karpechko, A. Y., Hegerl, G. C., ... and Jones, P. D. (2008). Attribution of polar warming to human influence. Nature Geoscience, *1*(11), 750-754.

Golden, K. (2001). Brine percolation and the transport properties of sea ice. Annals of Glaciology, 33, 28-36. doi:10.3189/172756401781818329

Goosse, H., Kay, J. E., Armour, K. C., Bodas-Salcedo, A., Chepfer, H., Docquier, D., ... and Vancoppenolle, M. (2018). Quantifying climate feedbacks in polar regions. Nature communications, 9(1), 1919.

Graham, R. M., Itkin, P., Meyer, A., Sundfjord, A., Spreen, G.,Smedsrud, L. H., Liston, G. E., Cheng, B., Cohen, L., Divine,D., Fer, I., Fransson, A., Gerland, S., Haapala, J., Hudson,S. R., Johansson, A. M., King, J., Merkouriadi, I., Peterson,A. K., Provost, C., Randelhoff, A., Rinke, A., Rösel, A.,Sennéchael, N., Walden, V. P., Duarte, P., Assmy, P., Steen, H.,and Granskog, M. A. (2019). Winter storms accelerate the demise of sea ice in the Atlantic sector of the Arctic Ocean, Sci. Rep.-UK, 9,9222, https://doi.org/10.1038/s41598-019-45574-5.

Grenfell, T. C., and Perovich, D. K. (2004). Seasonal and spatial evolution of albedo in a snow-ice-land-ocean environment. Journal of Geophysical Research: Oceans, *109*(C1).

Grenfell, T. C., Barber, D. G., Fung, A. K., Gow, A. J., Jezek, K. C., Knapp, E. J., ... and Tanis, F. (1998). Evolution of electromagnetic signatures of sea ice from initial formation to the establishment of thick first-year ice. IEEE Transactions on geoscience and remote sensing, 36(5), 1642-1654.

Haas, C., and Howell, S. E. L. (2015). Ice thickness in the Northwest Passage. Geophysical Research Letters, https://doi.org/10.1002/2015GL065704.

Haas, C., Lobach, J., Hendricks, S., Rabenstein, L., and Pfaffling, A. (2009). Helicopter-borne measurements of sea ice thickness, using a small and lightweight, digital EM system. Journal of Applied Geophysics, 67(3), 234-241.

He, L., He, X., Hui, F., Ye, Y., Zhang, T., and Cheng, X. (2022). Investigation of polarimetric decomposition for Arctic summer sea ice classification using Gaofen-3 fully polarimetric SAR data. IEEE Journal of Selected Topics in Applied Earth Observations and Remote Sensing, 15, 3904-3915.

Hibler III, W. D. (1986). Ice dynamics. In The geophysics of sea ice (pp. 577-640). Boston, MA: Springer US.

Holland, J. M., Currier, J. M., and Neimeyer, R. A. (2006). Meaning reconstruction in the first two years of bereavement: The role of sense-making and benefit-finding. *Omega-Journal of Death and Dying*, *53*(3), 175-191.

Howell, S. E. L., Komarov, A. S., Dabboor, M., Montpetit, B., Brady, M., Scharien, R. K., Mahmud, M. S., Nandan, V., Geldsetzer, T., and Yackel, J. J. (2018). *Comparing L- and C-Band Synthetic Aperture Radar Estimates of Sea Ice Motion over Different Ice Regimes*. *Remote Sensing of Environment*, 204, 380-391. https://doi.org/10.1016/j.rse.2017.10.017.

Howell, S. E., and Brady, M. (2019). The dynamic response of sea ice to warming in the Canadian Arctic Archipelago. Geophysical Research Letters, *46*(22), 13119-13125.

Howell, S. E., Derksen, C., Pizzolato, L., and Brady, M. (2015). Multiyear ice replenishment in the C anadian A rctic A rchipelago: 1997–2013. Journal of Geophysical Research: Oceans, *120*(3), 1623-1637.

Howell, S. E., Scharien, R. K., Landy, J., and Brady, M. (2020). *Spring Melt Pond Fraction in the Canadian Arctic Archipelago Predicted from RADARSAT-2*. The Cryosphere, 14(12), 4675-4686.

Howell, S. E., Tivy, A., Agnew, T., Markus, T., and Derksen, C. (2010). Extreme low sea ice years in the Canadian Arctic Archipelago: 1998 versus 2007. Journal of Geophysical Research*:* Oceans, *115*(C10).

Howell, S. E., Wohlleben, T., Dabboor, M., Derksen, C., Komarov, A., and Pizzolato, L. (2013). Recent changes in the exchange of sea ice between the Arctic Ocean and the Canadian Arctic Archipelago. Journal of Geophysical Research: Oceans, *118*(7), 3595-3607.

Isoguchi, O., and Shimada, M. (2009). An L-band ocean geophysical model function derived from PALSAR. IEEE Transactions on Geoscience and Remote Sensing, 47(7), 1925-1936.

Itkin, P., Spreen, G., Cheng, B., Doble, M., Girard-Ardhuin, F., Haapala, J., Hughes, N., Kaleschke, L., Nicolaus, M., and Wilkinson, J. (2017). Thin ice and storms: Sea ice deformation from buoy arrays deployed during N-ICE2015, J. Geophys. Res.-Oceans, 122, 4661–4674, https://doi.org/10.1002/2016JC012403.

Johannessen, O. M., and Shalina, E. V. (2023). Will the summer sea ice in the Arctic reach a tipping point?. Atmospheric and Oceanic Science Letters, 16(3), 100352.

Kovacs, A. (1996). Sea ice. Part 1, Bulk salinity versus ice floe thickness.

Kwok, R. (2006). Exchange of sea ice between the Arctic Ocean and the Canadian Arctic Archipelago. *Geophysical research letters*, *33*(16).

Kwok, R., and Cunningham, G. F. (2012). Deformation of the Arctic Ocean ice cover after the 2007 record minimum in summer ice extent. Cold Regions Science and Technology, *76*, 17-23.

Kwok, R., and Rothrock, D. A. (2009). Decline in Arctic Sea Ice Thickness from Submarine and ICESat Records: 1958-2008. Geophysical Research Letters, 36(15), 1-5. https://doi.org/10.1029/2009GL039035.

Landrum, L. and Holland, M. M. (2020). Extremes become routine in an emerging new Arctic, Nat. Clim. Change, 10, 1108–1115, https://doi.org/10.1038/s41558-020-0892-z.

Laxon, S. W., Giles, K. A., Ridout, A. L., Wingham, D. J., Willatt, R., Cullen, R., Kwok, R., Schweiger, A., Zhang, J., Haas, C., Hendricks, S., Krishfield, R., Kurtz, N., Farrell, S., and Davidson, M. (2013). *CryoSat-2 Estimates of Arctic Sea Ice Thickness and Volume*. *Geophysical Research Letters*, 40(4), 732-737. https://doi.org/10.1002/grl.50193.

Lei, R., Gui, D., Hutchings, J. K., Heil, P., and Li, N. (2020). Annual cycles of sea ice motion and deformation derived from buoy measurements in the western Arctic Ocean over two ice seasons. Journal of Geophysical Research: Oceans, *125*(6), e2019JC015310.

Li, H., and Perrie, W. (2016). Sea ice characterization and classification using hybrid polarimetry SAR. IEEE Journal of Selected Topics in Applied Earth Observations and Remote Sensing, 9(11), 4998-5010.

Livingstone, C. E., Onstott, R. G., Arsenault, L. D., Gray, A. L., and Singh, K. P. (1987). Microwave sea-ice signatures near the onset of melt. IEEE Transactions on Geoscience and Remote Sensing, (2), 174-187.

Loh, W. Y., and Shih, Y. S. (1997). Split selection methods for classification trees. Statistica sinica, 815-840.

Lohse, J., Doulgeris, A. P., and Dierking, W. (2019). An optimal decision-tree design strategy and its application to sea ice classification from SAR imagery. Remote Sensing, 11(13), 1574.

Mahmud, M. S., Nandan, V., Howell, S. E., Geldsetzer, T., and Yackel, J. (2020). Seasonal evolution of L-band SAR backscatter over landfast Arctic sea ice. Remote Sensing of Environment, 251, 112049.

Makynen, M. P., Manninen, A. T., Simila, M. H., Karvonen, J. A., and Hallikainen, M. T. (2002). Incidence angle dependence of the statistical properties of C-band HH-polarization backscattering signatures of the Baltic Sea ice. IEEE Transactions on Geoscience and Remote Sensing, 40(12), 2593-2605.

Markus, T., Stroeve, J. C., and Miller, J. (2009). Recent Changes in Arctic Sea Ice Melt Onset, Freezeup, and Melt Season Length. Journal of Geophysical Research: Oceans, 114(12), 1–14. doi:10.1029/2009JC005436.

Maslanik, J. A., Fowler, C., Stroeve, J., Drobot, S., Zwally, J., Yi, D., and Emery, W. (2007). A Younger, Thinner Arctic Ice Cover: Increased Potential for Rapid, Extensive Sea-Ice Loss. Geophysical Research Letters. doi:10.1029/2007GL032043.

Maykut, G. A. (1985). An introduction to ice in the polar oceans (No. APL-UW-8510). Department of Atmospheric Sciences/Geophysics Program, University of Washington.

Meier, W. N., and Stroeve, J. (2022). An updated assessment of the changing Arctic sea ice cover. Oceanography, 35(3/4), 10-19.

Meier, W. N., Hovelsrud, G. K., Van Oort, B. E. H., Key, J. R., Kovacs, K. M., Michel, C., Haas, C., Granskog, M. A., Gerland, S., Perovich, D. K., Makshtas, A., and Reist, J. D. (2014). Arctic Sea Ice in Transformation: A Review of Recent Observed Changes and Impacts on Biology and Human Activity. Reviews of Geophysics. doi:10.1002/2013RG000431.

Melling, H. (2022). Thickness of multi-year sea ice on the northern Canadian polar shelf: a second look after 40 years. The Cryosphere, 16(8), 3181-3197.

Menze, B. H., Kelm, B. M., Masuch, R., Himmelreich, U., Bachert, P., Petrich, W., and Hamprecht, F. A. (2009). A comparison of random forest and its Gini importance with standard chemometric

methods for the feature selection and classification of spectral data. BMC bioinformatics, 10, 1-16.

Moreira, A., Prats-Iraola, P., Younis, M., Krieger, G., Hajnsek, I., and Papathanassiou, K. P. (2013). A tutorial on synthetic aperture radar. IEEE Geoscience and remote sensing magazine, 1(1), 6-43.

Mortin, J., Howell, S. E. L., Wang, L., Derksen, C., Svensson, G., Graversen, R. G., and Schrøder, T. M. (2014). Extending the QuikSCAT Record of Seasonal Melt-Freeze Transitions over Arctic Sea Ice Using ASCAT. Remote Sensing of Environment, 141, 214–230. doi:10.1016/j.rse.2013.11.004.

Nasonova, S., Scharien, R. K., Geldsetzer, T., Howell, S. E. L., and Power, D. (2018). Optimal Compact Polarimetric Parameters and Texture Features for Discriminating Sea Ice Types during Winter and Advanced Melt. Canadian Journal of Remote Sensing, 44(4), 390–411.

Nghiem, S. V., and Bertoia, C. (2001). Study of multi-polarization C-band backscatter signatures for Arctic sea ice mapping with future satellite SAR. Canadian Journal of Remote Sensing, 27(5), 387-402.

Nicolaus, M., Katlein, C., Maslanik, J., and Hendricks, S. (2012). Changes in Arctic sea ice result in increasing light transmittance and absorption. Geophysical Research Letters, 39(24).

Nicolaus, M., Perovich, D. K., Spreen, G., Granskog, M. A., von Albedyll, L., Angelopoulos, M., ... and Wendisch, M. (2022). Overview of the MOSAiC expedition: Snow and sea ice. Elem Sci Anth, 10(1), 000046.

Notz, D., and Marotzke, J. (2012). Observations reveal external driver for Arctic sea-ice retreat. Geophysical Research Letters, 39(8).

Onstott, R. G., and Carsey, F. D. (1992). SAR and scatterometer signatures of sea ice. Microwave remote sensing of sea ice, 68, 73-104.

Onstott, R. G., and Gogineni, S. P. (1985). Active microwave measurements of Arctic sea ice under summer conditions. Journal of Geophysical Research, 90(C3), 5035–5044. doi:10.1029/JC090iC03p05035.

Onstott, R. G., Grenfell, T. C., Matzler, C., Luther, C. A., and Svendsen, E. A. (1987). Evolution of microwave sea ice signatures during early summer and midsummer in the marginal ice zone. Journal of Geophysical Research: Oceans, 92(C7), 6825-6835.

Pearce, T., Ford, J., Willox, A. C., and Smit, B. (2015). Inuit traditional ecological knowledge (TEK), subsistence hunting and adaptation to climate change in the Canadian Arctic. Arctic, 233-245.

Perovich, D. K., Grenfell, T. C., Light, B., and Hobbs, P. V. (2002). Seasonal evolution of the albedo of multiyear Arctic sea ice. Journal of Geophysical Research: Oceans, 107(C10), SHE-20.

Perovich, D. K., Light, B., Eicken, H., Jones, K. F., Runciman, K., and Nghiem, S. V. (2007). Increasing solar heating of the Arctic Ocean and adjacent seas, 1979–2005: Attribution and role in the ice-albedo feedback. Geophysical Research Letters, 34(19).

Perovich, D. K., Richter-Menge, J. A., and Tucker, W. B. (2001). Seasonal changes in Arctic sea-ice morphology. Annals of Glaciology, 33, 171-176.

Petrich, C., and H. Eicken (2009). Chapter 2: Growth, Structure and Properties of Sea Ice. In D.N. Thomas and G.S. Dieckmann (Eds.), Sea Ice, Second Edition, pp. 23-77. Oxford, United Kingdom: Blackwell Publishing Ltd.

Pizzolato, L., Howell, S. E. L., Derksen, C., Dawson, J., and Copland, L. (2014). Changing sea ice conditions and marine transportation activity in Canadian Arctic waters between 1990 and 2012. Climatic Change, 123(2), 161–173. http://dx.doi.org/10.1007/ s10584-013-1038-3.

Polashenski, C., Perovich, D., and Courville, Z. (2012). The mechanisms of sea ice melt pond formation and evolution. Journal of Geophysical Research: Oceans, 117(C1).

Raney K.R., Cahill, J. T. S., Patterson Wesley, G., and Bussey, D. B. J. (2012). The m-chi decomposition of hybrid dual-polarimetric radar data with application to lunar craters. Journal of Geophysical Research E: Planets, 117(5), 1–8. doi:10.1029/2011JE003986.

Raney, R. K. (2006). Dual-polarized SAR and stokes parameters. IEEE Geoscience and Remote Sensing Letters, 3(3), 317–319. doi:10.1109/LGRS.2006.871746.

Raney, R. K., Freeman, A., and Jordan, R. L. (2011). Improved range ambiguity performance in quad-pol SAR. IEEE Transactions on Geoscience and Remote Sensing, 50(2), 349-356.

Ressel, R., Frost, A., and Lehner, S. (2015). A neural network-based classification for sea ice types on X-band SAR images. IEEE Journal of Selected Topics in Applied Earth Observations and Remote Sensing, 8(7), 3672-3680.

Rothrock, D. A., Yu, Y., and Maykut, G. A. (1999). Thinning of the Arctic sea-ice cover. Geophysical Research Letters, 26(23), 3469-3472.

Scharien, R. (2010). Physical and Polarimetric C-Band Microwave Scattering Properties of First-Year Arctic (Doctoral dissertation, UNIVERSITY OF CALGARY).

Scharien, R. K., and Yackel, J. J. (2005). Analysis of surface roughness and morphology of first-year sea ice melt ponds: Implications for microwave scattering. IEEE Transactions on Geoscience and Remote Sensing, 43(12), 2927–2939. doi:10.1109/TGRS.2005.857896.

Scharien, R. K., Geldsetzer, T., Nasonova, S., Cafarella, S., and Tavri, A. (2018). Assessment of seasonal sea ice type and roughness regime discrimination using a unique C-and L-band SAR database. In IGARSS

Scharien, R. K., Hochheim, K., Landy, J., and Barber, D. G. (2014). First-year sea ice melt pond fraction estimation from dual-polarisation C-band SAR–Part 2: Scaling in situ to Radarsat-2. The Cryosphere, 8(6), 2163-2176.

Scharien, R. K., Segal, R., Nasonova, S., Nandan, V., Howell, S. E., and Haas, C. (2017). Winter Sentinel-1 backscatter as a predictor of spring Arctic sea ice melt pond fraction. Geophysical Research Letters, 44(24), 12-262.

Scharien, R. K., Yackel, J. J., Barber, D. G., Asplin, M., Gupta, M., and Isleifson, D. (2012). Geophysical controls on C band polarimetric backscatter from melt pond covered Arctic first-year sea ice: Assessment using high-resolution scatterometry. Journal of Geophysical Research: Oceans, 117(C9).

Scheuchl, B., Hajnsek, I., and Cumming, I. (2002). Sea ice classification using multi-frequency polarimetric SAR data. In IEEE International Geoscience and Remote Sensing Symposium (Vol. 3, pp. 1914-1916). IEEE.

Scheuchl, B., Cumming, I., and Hajnsek, I. (2005). Classification of fully polarimetric single-and dual-frequency SAR data of sea ice using the Wishart statistics. Canadian Journal of Remote Sensing, 31(1), 61-72.

Shokr, M. E., and Barber, D. G. (1994). Temporal evolution of physical and dielectric properties of sea ice and snow during the early melt season: observations from SIMS'90 experiment. Journal of Glaciology, 40(134), 16-30.

Shokr, M., and Dabboor, M. (2023). Polarimetric SAR Applications of Sea Ice: A Review. IEEE Journal of Selected Topics in Applied Earth Observations and Remote Sensing.

Shokr, M., and Sinha, N. K. (2023). Sea ice: physics and remote sensing. John Wiley and Sons.

Singha, S., Johansson, M., Hughes, N., Hvidegaard, S.M., Skourup, H. (2018). Arctic sea ice characterization using spaceborne fully polarimetric L-, C-, and X-band SAR with validation by airborne measurements. IEEE Transactions on Geoscience and Remote Sensing, 56 (7), 3715–3734. https://doi.org/10.1109/TGRS.2018.2809504.

Singha, S., Johansson, A. M., and Doulgeris, A. P. (2020). Robustness of SAR sea ice type classification across incidence angles and seasons at L-band. IEEE Transactions on Geoscience and Remote Sensing, 59(12), 9941-9952.

Singha, S., and Ressel, R. (2017). Arctic sea ice characterization using RISAT-1 compact-pol SAR imagery and feature evaluation: A case study over Northeast Greenland. IEEE Journal of Selected Topics in Applied Earth Observations and Remote Sensing, 10(8), 3504-3514.

Snoeij, P., Unal, C. M. H., and Attema, E. P. W. 1991. "The response of the radar echo from the ocean surface to the surface wind vector at frequencies between 1 and 18 GHz compared with model predictions." In [Proceedings] IGARSS'91 Remote Sensing: Global Monitoring for Earth Management, (Vol. 3, pp. 1281-1284). IEEE.

Spreen, G., Kwok, R., and Menemenlis, D. (2011). Trends in Arctic sea ice drift and role of wind forcing: 1992–2009. Geophysical Research Letters, 38(19).

Stephenson, S. R., Smith, L. C., Brigham, L. W., and Agnew, J. A. (2013). Projected 21st-century changes to Arctic marine access. Climatic Change, 118, 885-899.

Stroeve, J., and Notz, D. 2015. "Insights on past and future sea-ice evolution from combining observations and models." In Global and Planetary Change, https://doi.org/10.1016/j.gloplacha.2015.10.011

Stroeve, J., Holland, M. M., Meier, W., Scambos, T., and Serreze, M. (2007). Arctic sea ice decline: Faster than forecast. Geophysical research letters, 34(9).

Strong, C., and Rigor, I. G. (2013). Arctic marginal ice zone trending wider in summer and narrower in winter. Geophysical Research Letters, 40(18), 4864-4868.

Sumata, H., de Steur, L., Divine, D. V., Granskog, M. A., and Gerland, S. (2023). Regime shift in Arctic Ocean sea ice thickness. Nature, 615(7952), 443-449.

Tavri, A., Scharien, R.K, and Geldsetzer, T., (2023). Melt Season Arctic Sea Ice Type Separability Using Fully and Compact Polarimetric C- and L-band Synthetic Aperture Radar. Canadian Journal of Remote Sensing, VOL. 49, NO. 1, 2271578. https://doi.org/10.1080/07038992.2023.2271578

Thompson, D. W., and Wallace, J. M. (1998). The Arctic Oscillation signature in the wintertime geopotential height and temperature fields. Geophysical research letters, 25(9), 1297-1300.

Tiuri, M. E., Sihvola, A. H., Nyfors, E. G., and Hallikaiken, M. T. 1984. "The Complex Dielectric Constant of Snow at Microwave Frequencies." IEEE Journal of Oceanic Engineering, 9(5), 377–382. https://doi.org/10.11

Toyota, T., Ishiyama, J., and Kimura, N. (2020). Measuring deformed sea ice in seasonal ice zones using L-band SAR images. IEEE Transactions on Geoscience and Remote Sensing, 59(11), 9361-9381.

Tsamados, M., Feltham, D., Petty, A., Schroeder, D., and Flocco, D. (2015). Processes controlling surface, bottom and lateral melt of Arctic sea ice in a state of the art sea ice model. Philosophical Transactions of the Royal Society A: Mathematical, Physical and Engineering Sciences, 373(2052), 20140167.

Ulaby, F. T., Moore, R. K., and Fung, A. K. (1986). Microwave remote sensing: Active and passive. Volume 3-From theory to applications.

Wadhams, P. (2000). Ice In The Ocean. London, UK: Gordon and Breach Science Publishers

Wang, J., and Ikeda, M. (2000). Arctic oscillation and Arctic sea-ice oscillation. Geophysical Research Letters, 27(9), 1287-1290.

Webster, M. A., Rigor, I. G., Nghiem, S. V., Kurtz, N. T., Farrell, S. L., Perovich, D. K., and Sturm, M. (2014). Interdecadal changes in snow depth on Arctic sea ice. Journal of Geophysical Research: Oceans, 119(8), 5395-5406.

Webster, M. A., Holland, M., Wright, N. C., Hendricks, S., Hutter, N., Itkin, P., ... and Zhang, J. 2022. "Spatiotemporal evolution of melt ponds on Arctic sea ice: MOSAiC observations and model results." Elem Sci Anth, 10(1), 000072.

Weeks, W. F., and Ackley, S. F. (1986). The growth, structure, and properties of sea ice (pp. 9-164). Springer US

Weeks, W. F., and Gow, A. J. (1978). Preferred crystal orientations in the fast ice along the margins of the Arctic Ocean. Journal of Geophysical Research: Oceans, 83(C10), 5105-5121.

WMO (2014). WMO Sea-Ice Nomenclature. WMO Report No. 259. Geneva, Switzerland: World Meteorological Organization.

Yackel, J. J., and Barber, D. G. 2000. “Melt ponds on sea ice in the Canadian Archipelago: 2. On the use of RADARSAT-1 synthetic aperture radar for geophysical inversion.” Journal of Geophysical Research: Oceans, 105(C9), 22061-22070.

Yackel, J. J., Barber, D. G., and Hanesiak, J. M. (2000). Melt ponds on sea ice in the Canadian Archipelago: 1. Variability in morphological and radiative properties. Journal of Geophysical Research: Oceans, 105(C9), 22049-22060.

Yackel, J. J., Barber, D. G., Papakyriakou, T. N., and Breneman, C. (2007). First-year sea ice spring melt transitions in the Canadian Arctic Archipelago from time-series synthetic aperture radar data, 1992–2002. Hydrological Processes: An International Journal, 21(2), 253-265.

Zakhvatkina, N., Smirnov, V., and Bychkova, I. (2019). Satellite SAR data-based sea ice classification: An overview. Geosciences, 9(4), 152.

Appendix A.

Table S.1: An overview of the SAR polarimetric parameters examined in this study.

Polarimetric parameters (FP)	Description	Equation	Units
Span	Total power	$\langle S_{HH}S_{HH}^{*}\rangle + \langle S_{VV}S_{VV}^{*}\rangle + 2\langle S_{HV}S_{HV}^{*}\rangle$	Power
HH, HV, VV	Sigma naught (σ^0) backscatter intensity	$\boldsymbol{S} = \begin{bmatrix} S_{HH} & S_{HV} \\ S_{VH} & S_{VV} \end{bmatrix}$	Power
VV/HH	Co-polarization ratio	$\sigma^0_{VV/HH}$	Unitless
HV/HH	Cross-polarization ratio	$\sigma^0_{HV/HH}$	Unitless
HV*HH, VV*HH (CP)	Polarization multiplications		Power
S_0, S_1, S_2, S_3	Stokes vectors derived from the covariance matrix C	$\boldsymbol{C} = \begin{bmatrix} \lvert S_{HH}\rvert^2 & \sqrt{2}S_{HH}S_{XX}^{*} & S_{HH}S_{VV}^{*} \\ \sqrt{2}S_{HH}^{*}S_{XX} & \lvert S_{XX}\rvert^2 & \sqrt{2}S_{XX}S_{VV}^{*} \\ S_{HH}^{*}S_{VV} & \sqrt{2}S_{XX}^{*}S_{VV} & \lvert S_{VV}\rvert^2 \end{bmatrix}$	Power
RV, RH RR, RL	Sigma naught (σ^0) backscatter intensity		Power
m	Degree of polarization	$m = \frac{\sqrt{S_1^2+S_2^2+S_3^2}}{S_0}$	Unitless
RR/RL	Circular polarization ratio	$\sigma^0_{RR/RL}$	Unitless
RV/RH	Right co-polarized ratio	$\sigma^0_{RV/RH}$	Unitless
μ	Conformity coefficient	$\mu = \frac{Re(S_{HH}S_{VV}^{*}) - \lvert S_{HV}\rvert^2}{(\lvert S_{HH}\rvert^2 + 2\lvert S_{HV}\rvert^2 + \lvert S_{VV}\rvert^2}$	Unitless

α_s	Alpha scattering angle	$\alpha_s = \frac{1}{2}\tan^{-1}\left(\frac{\sqrt{S_1^2+S_2^2}}{\pm S_3}\right)$	Radians
$m\chi_d$	$m\chi$ decomposition even bounce component	$m\chi_d = \sqrt{\frac{mS_0\,(1+\sin 2\chi)}{2}}$	Power
$m\chi_v$	$m\chi$ decomposition volumetric component	$m\chi_v = \sqrt{S_0\,(1-m)}$	Power
$m\chi_s$	$m\chi$ decomposition odd bounce component	$m\chi_s = \sqrt{\frac{mS_0(1-\sin 2\chi)}{2}}$	Power

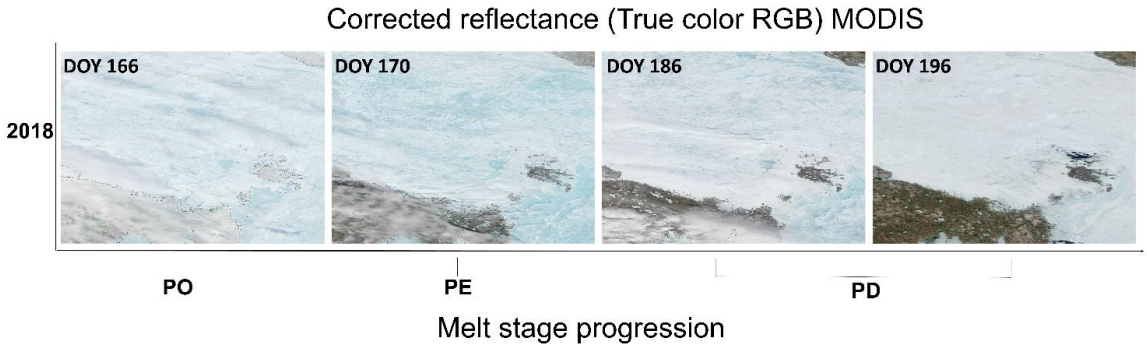

Figure S.1: Moderate Resolution Imaging Spectroradiometer (MODIS) corrected reflectance, true color timeseries of the advanced melt sub-stage evolution, for 2018 over M'Clintock Channel. The seasonal stages shown are Pond Onset (PO), Pond Evolution (PE) and Pond Drainage (PD).

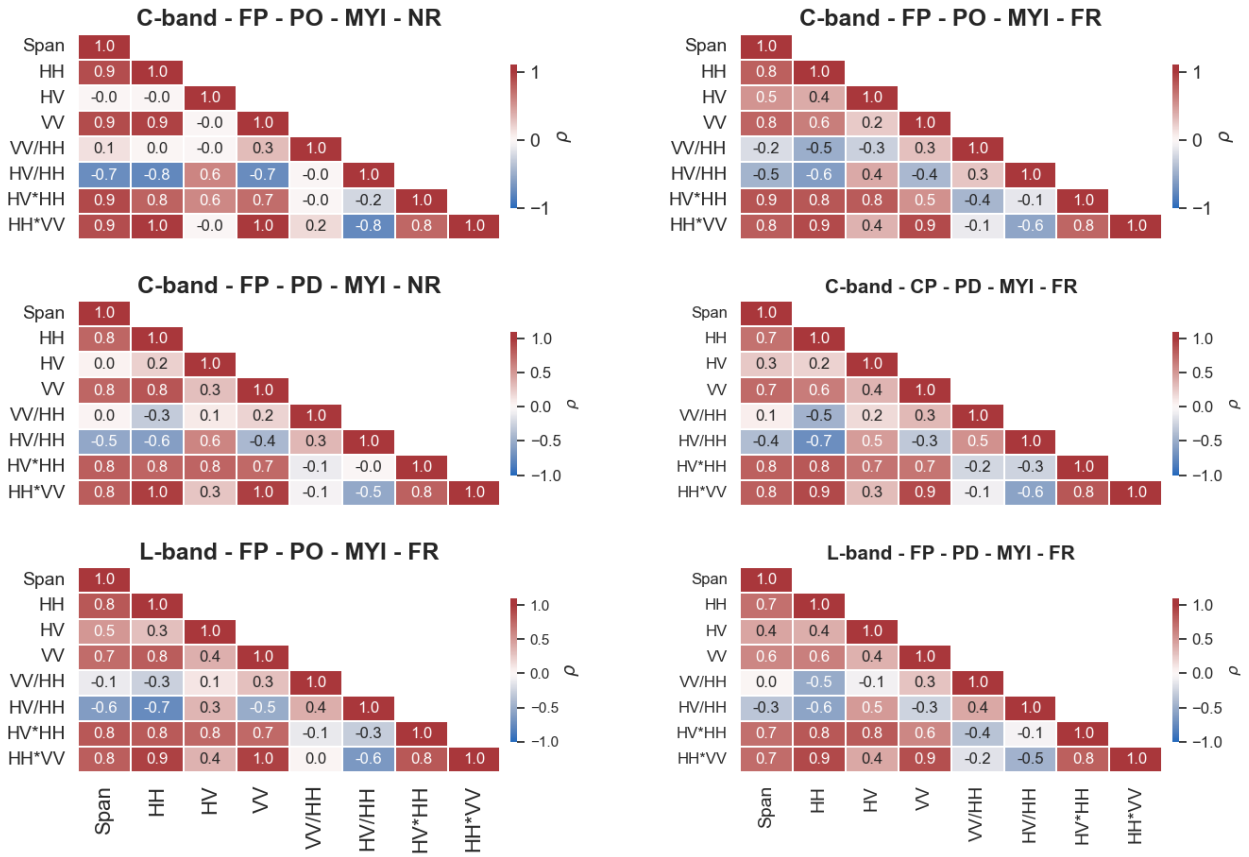

Figure S.2: Spearman's correlation matrices for the MYI FP mode. The heatmaps represent the correlation matrices from pond onset (PO) and pond drainage (PD) substages for each polarimetric parameter at C- and L-band. The effect of incidence angle is examined for the near and far range (NR, FR).

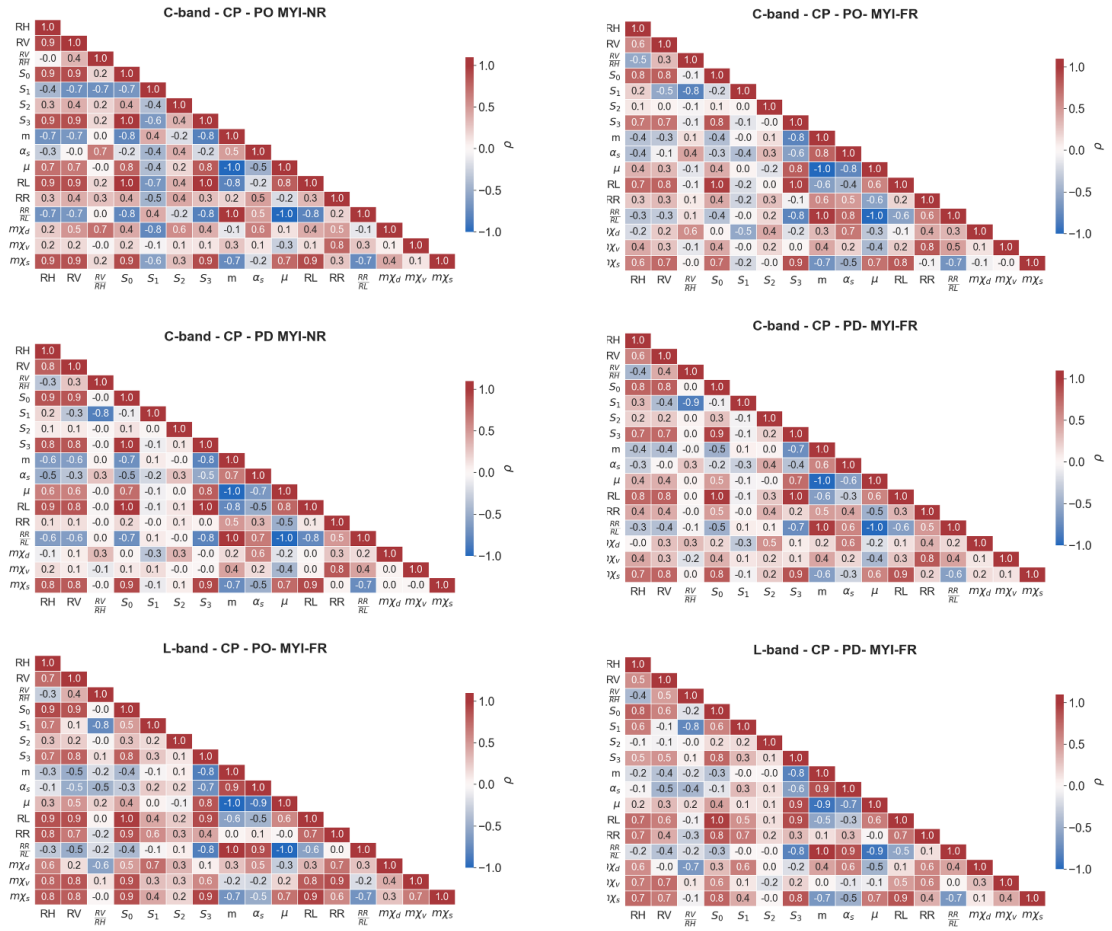

Figure S.3: Spearman's correlation matrices for the MYI CP mode. The heatmaps represent the correlation matrices from pond onset (PO) and pond drainage (PD) substages for each polarimetric parameter at C- and L-band. The effect of incidence angle is examined for the near and far range (NR, FR).

Contributions of collaborating authors

Chapter 2

R.. Scharien provided valuable discussion regarding the melt pond fraction retrievals and their connection to polarimetric parameters and contributed to revisions.

T. Geldsetzer and contributed to revisions, especially commenting on the relationships and utility of the compact polarimetric parameters and decompositions for retrieving the dominating scattering mechanisms.

Chapter 3

R.Scharien provided valuable discussion on including deformed ice in the classification, elaborating the airborne sea ice roughness measurements. Additionally, provided the segmentation object for the visual aid of the classification outputs and contributed to revisions.